AD

Research and Development Technical Report
ECOM-0341-1

A PARAMETRIC SURVEY OF THE XENON ELECTRODELESS ARC LAMP

FINAL REPORT

BY

D.D. HOLLISTER, R. E. PRICE, AND K. CHOY

MARCH 1972

DISTRIBUTION STATEMENT

Approved for public release; distribution unlimited.

ECOM

UNITED STATES ARMY ELECTRONICS COMMAND-NVL, FT. BELVOIR, VA.

Contract DAAK02-71-C-0341

CHARYBDIS INC.

2259 VIA BURTON
ANAHEIM, CALIFORNIA 92806

NOTICES

Disclaimers

The findings in this report are not to be construed as an official Department of the Army position, unless so designated by other authorized documents.

The citation of trade names and names of manufacturers in this report is not to be construed as official Government indorsement or approval of commercial products or services referenced herein.

Disposition

Destroy this report when it is no longer needed. Do not return it to the originator.

A PARAMETRIC SURVEY OF THE XENON ELECTRODELESS ARC LAMP

FINAL REPORT

March, 1972

CONTRACT NO. DAAK02-71-C-0341
DA Task No. 1S663719DK70-03-052

DISTRIBUTION STATEMENT

Approved for public release;
distribution unlimited

PREPARED BY

D.D. HOLLISTER, R.E. PRICE, AND K. CHOY

CHARYBDIS, INC.
2259 Via Burton
Anaheim, CA 92806

FOR

U.S. ARMY ELECTRONICS COMMAND, NVL, FT. BELVOIR, VA

SUMMARY

This report treats an initial survey of many of the observable properties of prototype electrodeless arc lamps. One objective of this study was to determine the practical feasibility of the lamp's use in real systems, as well as the strengths and weaknesses of such lamps in actual use. Another objective was the discovery of operational trends particular to electrodeless arc lamps in order to exploit their unique characteristics and to improve further their radiation production efficiency.

The electrodeless arc plasma is an efficient radiator because radiation is the only loss mechanism allowed to contribute appreciably to the discharge energy balance, when the discharge is formed in a sealed sphere and the effects of radial heat conduction are minimized. In this study, the performance characteristics of the electrodeless arc lamp were mapped in terms of established operating parameters. Additionally, observational trends were found which could be used to extend the lamp's range of operation.

The causes of inefficiency in lamp operation were examined and methods developed for improving lamp performance; in this connection, data which demonstrate lamp operational efficiencies approaching the theoretical maximum are presented. Also, the principal cause of electrodeless arc lamp failure was determined, and techniques were developed for preventing lamp failures.

An initial overview of the feasibility, characteristics, and trends of operation of electrodeless arc metal-vapor lamps has been included in this study. Measurements of key properties of the high-pressure mercury vapor electrodeless arc lamp are reported, and observations of several such lamps are analyzed. The basic principles of metal-vapor lamp operation are extrapolated for application to alkali-vapor electrodeless arc lamps.

TABLE OF CONTENTS

TABLE OF CONTENTS (Cont'd.)

LIST OF ILLUSTRATIONS

LIST OF ILLUSTRATIONS (Cont'd).

SECTION 1

INTRODUCTION

This report treats an initial survey of many of the observable properties of prototype electrodeless arc lamps. One objective of this study was to determine the practical feasibility of the lamp's use in real systems, as well as the strengths and weaknesses of such lamps in actual use. Another objective was the discovery of operational trends particular to electrodeless arc lamps in order to exploit their unique characteristics and to further improve their radiation production efficiency.

The electrodeless arc lamp basically is a very efficient power/energy conversion device for the production of thermal radiation. In operation, the lamp absorbs part of the reactive energy stored in a high-frequency inductor. This energy induces currents in the ionized gas contained in the lamp to yield a volume heating rate j^2/σ, where $|j|$ is the induced current density at some point in the plasma, and σ is the electrical conductivity of the discharge plasma at that point. If the discharge is maintained at a sufficiently high-pressure (usually above one or two atmospheres) a condition of quasi-or local-thermodynamic equilibrium obtains, and the plasma is said to "thermalize". The important feature of a thermal plasma is that equipartition of energy effectively exists among all species present in the plasma, and a plasma "temperature" and its distribution can be defined, at least locally. Thermal plasmas usually exist in the positive column of an arc struck between elelctrodes, hence such plasmas are often called "thermal-arcs", or simply "arcs". Certain arc characteristics can be defined[1] in terms of electrode phenomenology, but the main characteristic of any arc, its thermal plasma, has properties which do not depend directly on the electrodes. The electrodeless arc plasma is indistinguishable from the plasma of the positive column of an arc-between-electrodes for a given gas and temperature and pressure.

The electrodeless arc plasma is an efficient radiator because radiation is the only loss mechanism allowed to contribute appreciably to the discharge energy balance, when the discharge is formed in a sealed sphere and the effects of radial heat conduction are minimized. That is, in the absence of mass throughflow as provided by "vortex-stabilization"[2], or dynamic instabilities, convective contributions to discharge energy balance assume negligible proportions, as do the effects of plasma viscosity. If the discharge is constrained to exist far from the wall of its envelope, the contribution by radial conductive transport to the discharge energy balance can be reduced to a small fraction of the total power. All that is left to balance ohmic heating is radiation. Thus, by choosing operating points which keep the discharge far from the wall of the envelope, and by designing lamps that do not trigger convective instabilities in the induced discharge one has assembled the basic elements of an exceptionally efficient source of optical radiation.

This study yielded several important results. The performance characteristics of the electrodeless arc lamp were mapped in terms of established operating parameters. Additionally, some operational trends which determine methods for extending the lamp's range of operation were examined and methods developed for improving lamp performance; data which demonstrate lamp operational efficiencies approaching the theoretical maximum are presented. Also, the principal cause of electrodeless arc lamp failure was determined, and techniques were developed for preventing lamp failures. An initial overview of the feasibility, characteristics, and trends of operation of electrodeless arc metal-vapor lamps is presented, and measurements of key properties of the mercury-vapor electrodeless arc lamp were analyzed. The basic principles of vapor-lamp operation are extrapolated for application to alkali-vapor electrodeless arc lamps.

SECTION 2

FUNDAMENTAL BASIS OF THE ELECTRODELESS ARC LAMP

No theoretical treatment of the electrodeless arc in high-pressure xenon is known to exist. While such a study is beyond the scope of the present effort, it is possible to glean physical insight into the xenon electrodeless arc from the results of an earlier analysis[3] of the electrodeless arc in high-pressure air. Much reliance has been placed on this research during the design of the experiment for the present study.

2.1 CONDUCTIVE HEAT TRANSPORT AND WALL-INDEPENDENCE

The most important determining factor of the power conversion efficiency of an electrodeless arc lamp is the effect of the lamp's envelope on the energy balance of the discharge. If radial conductive heat transport to the envelope wall is enhanced by the proximity of the wall to the discharge or by other means, the power conversion efficiency of that discharge is appreciably less than if the conductive heat transport loss is negligible. The electrodeless arc lamp is a viable concept because the discharge in the lamp is relatively independent of the walls of its container. If this were not the case a containment problem would exist for which there is no known solution. Fortunately, the electrodeless arc discharge can be shown to exist independent of an outer boundary condition (i.e., the wall) without recourse to the properties of the specific gas in which the discharge is formed. This unique property of the electrodeless arc is so basic to an understanding of the physics of the electrodeless lamp that its demonstration is believed necessary for this report. The following analysis therefore has been taken from another source[4], to which the interested reader is referred for more detail.

2.2 WALL-INDEPENDENT EXISTENCE CONDITION

All arc discharges are constrained to exist in such a state that the total entropy production of a given arc

is minimal for the particular operating conditions of that arc. Steenbeck's principle[5,6,7] reflects this statement by requiring that the first variation of the entropy production rate θ must vanish:

$$\delta\theta = 0, \tag{1}$$

where the total entropy production rate of the discharge is related to the total dissipation P and a fixed (i.e., constant) boundary temperature T_R according to $\theta = PT_R^{-1}$. The variation is thus written

$$\delta(PT_R^{-1}) = T_R^{-1}\delta P = 0, \tag{2}$$

and the discharge exists subject to the boundary conditions, the energy equation, the field equations, and the relation presented in Eq. (2).

In the problem of the electrodeless arc the induction field $\underline{B}(r)$ is given by

$$\nabla^2\underline{B}(r) - i\sigma(r)\mu\omega\underline{B}(r) - \frac{\sigma'(r)}{\sigma(r)}\underline{B}'(r) = 0, \tag{3}$$

where μ is the uniform permeability and $\sigma(r)$ is the electrical conductivity of the discharge plasma at a radial position r, the primes refer to radial derivatives and the implicit time dependence of the field parameters $\exp(i\omega t)$ is understood. One notes $\nabla \times \underline{B}(r) = \mu\underline{j}(r)$, where $\underline{j}(r)$ is the current density, and takes the volume dissipation at r to be $\frac{1}{2}\underline{j}(r)\cdot\underline{E}^*(r)$ where $\underline{E}(r)$ is the electric field intensity, to form the power integral

$$P = \frac{1}{2\mu^2}\int_{vol} \sigma^{-1}\underline{B}'\cdot\underline{B}^{*\prime}d(vol), \tag{4}$$

the variation of which must vanish consistent with Eq. (3). This constraint is incorporated by forming the product of Eq. (3) and $\underline{B}^*(r)$ and subtracting from it the product of the complex conjugate of Eq. (3) and $\underline{B}(r)$ to form

$$\int_{vol}[\underline{B}^*(r)\nabla^2\underline{B}(r) - \underline{B}(r)\nabla^2\underline{B}^*(r)]dV =$$

$$\int_{vol}\left\{2i\sigma(r)\mu\omega\underline{B}(r)\underline{B}^*(r) + \frac{\sigma'(r)}{\sigma(r)}[\underline{B}'(r)\underline{B}^*(r) - \underline{B}^{*\prime}(r)\underline{B}(r)]\right\}dV. \tag{5}$$

The volume integral of the left hand side of this equation must vanish by Green's theorem[8] since the gradients of the magnetic field vanish both along the axis of the discharge

by symmetry, and outside the discharge where the field is uniform by definition. Thus, the volume integral of the right hand side of Eq. (5) must also vanish, and this integral provides the necessary constraint for the variational calculation of Eq. (2). Equations (4) and (5) are now separated into their real and imaginary components and combined with Eq. (2) to obtain the variational principle for the existence of the electrodeless arc discharge:

$$\delta\frac{\pi}{T_R\mu^2}\int_0^R\left[\left(\frac{B_r'^2+B_i'^2}{\sigma}\right)r + \lambda\left(-\sigma\mu\omega B_i^2+\frac{\sigma'}{\sigma}B_r'B_i\right)r + \gamma\left(-\sigma\mu\omega B_r^2-\frac{\sigma'}{\sigma}B_i'B_r\right)r\right]dr = 0, \tag{6}$$

in which r and i denote the real and imaginary components of the induction field, λ and γ are Lagrangian multipliers which must be determined, the radial dependence of σ, B_r and B_i and their derivatives is implicit, and radial and azimuthal components of $\underline{B}$ have been neglected as usual. The Euler equations for discharge existence become

$$\frac{d}{dr}\left[2\frac{B_i'r}{\sigma} - \gamma\frac{\sigma'B_rr}{\sigma}\right] - \lambda\left[-2\sigma\mu\omega B_ir + \frac{\sigma'}{\sigma}B_r'r\right] = 0, \tag{7}$$

$$\frac{d}{dr}\left[2\frac{B_r'r}{\sigma} + \lambda\frac{\sigma'B_ir}{\sigma}\right] - \gamma\left[-2\sigma\mu\omega B_rr - \frac{\sigma'}{\sigma}B_i'r\right] = 0, \tag{8}$$

and

$$\frac{d}{dr}\left[\lambda\frac{B_r'B_ir}{\sigma}\right]-\left[-\frac{(B_r'^2+B_i'^2)}{\sigma^2}r-\lambda\mu\omega B_i'^2r-\lambda\frac{\sigma'B_r'B_ir}{\sigma^2} - \gamma\mu\omega B_r^2r+\gamma\frac{\sigma'B_i'B_rr}{\sigma^2}\right] = 0. \tag{9}$$

Solution of Eqs. (7) and (8) for the Lagrangian multipliers yields

$$\gamma = 2\sigma\mu\omega\,\frac{B_r(B_i\tilde{\theta}+\sigma'B_i') + B_i(2\sigma^2\mu\omega B_i-\sigma'B_r')}{(B_r\tilde{\theta}+\sigma'B_r')(B_i\tilde{\theta}+\sigma'B_i') + (2\sigma^2\mu\omega B_i-\sigma'B_r')(2\sigma^2\mu\omega B_r+\sigma'B_i')}, \tag{10}$$

and

$$\lambda = 2\sigma\mu\omega \frac{B_i(B_r\tilde{\theta}+\sigma' B_r') - B_r(2\sigma^2\mu\omega B_r - \sigma' B_i')}{(B_r\tilde{\theta}+\sigma' B_r')(B_i\tilde{\theta}+\sigma' B_i') + (2\sigma^2\mu\omega B_i - \sigma' B_r')(2\sigma^2\mu\omega B_r + \sigma' B_i')}, \tag{11}$$

where

$$\tilde{\theta} = \sigma'' + \frac{\sigma'}{r} - \frac{(\sigma')^2}{\sigma}.$$

Combination of Eqs. (9-11) gives

$$\lambda(\sigma' B_i B_r' + \sigma B_r' B_i') - \gamma(\sigma' B_r B_i' + \sigma B_i' B_r') = -(B_r'^2 + B_i'^2). \tag{12}$$

The field components and the electrical conductivity can be expanded in a Maclaurin series to obtain

$$B_{r,i}(r) = B_{r,i}(o) + \frac{1}{2!}B''_{r,i}(o)r^2 + \ldots ,$$

$$B'_{r,i}(r) = B''_{r,i}(o)r + \frac{1}{3!}B^{iv}_{r,i}(o)r^3 + \ldots ,$$

and similar forms for $\sigma(r)$, $\sigma'(r)$ and $\sigma''(r)$, where the odd terms vanish because of symmetry. The values of λ and γ are now evaluated at the origin:

$$\lambda = \mu\omega \frac{\frac{\sigma''(o)}{\sigma(o)} - \sigma(o)\mu\omega \frac{B_r(o)}{B_i(o)}}{\left[\left(\frac{\sigma''(o)}{\sigma(o)}\right)^2 + \left(\sigma(o)\mu\omega\right)^2\right]}, \tag{13}$$

$$\gamma = \mu\omega \frac{\frac{\sigma''(o)}{\sigma(o)} + \sigma(o)\mu\omega \frac{B_i(o)}{B_r(o)}}{\left[\left(\frac{\sigma''(o)}{\sigma(o)}\right)^2 + \left(\sigma(o)\mu\omega\right)^2\right]}, \tag{14}$$

Finally, these values are substituted in Eq. (12) to give, at the origin:

$$\frac{\sigma''(o)}{\sigma(o)} = \pm\sqrt{2}[\sigma(o)\mu\omega], \tag{15}$$

where $B''(o) = i \frac{1}{2} \sigma(o)\mu\omega B(o)$ was obtained from the expansion of Eq. (3) at the origin. Eq. (15) is the condition which, when employed in the simultaneous solution of the energy equation and the field equations, determines the existence of the electrodeless arc.

2.3 SIGNIFICANCE OF ANALYTICAL RESULTS

Eq. (15) is the existence condition of the thermally equilibrated electrodeless arc discharge. Both this equation and its derivation are independent of off-axis conditions, specifically the outer boundary conditions at the wall of the discharge envelope. Therefore, the existence of the electrodeless arc discharge is independent of the wall of its envelope.

Wall-independent discharge existence suggests that wall-independent discharge operation may be feasible. If so, high efficiency of radiation production can be obtained at the expense of conductive energy/power transport to the wall. The electrodeless arc lamp is the embodiment of this characteristic of the electrodeless arc discharge.

SECTION 3

EXPERIMENTAL PROCEDURE

The layout and geometry of the experiment are shown in Figure 1, where dimensions and other pertinent data are given. Wherever possible these dimensions were held fixed throughout the program.

3.1 EXPERIMENTAL SET-UP AND APPARATUS

The radiofrequency (rf) system used in this study consists of a variable high voltage (0-10 KV), direct current (0-4 ampere) supply, including filtering and regulation circuitry, and a pair of high-power triodes (EIMAC type 3CX10,000 A3) employed in a push-pull configuration as a tuned-grid, tuned-plate oscillator in which distributed elements form the major parts of the resonant circuitry.

Instrumentation is provided to allow measurement of the DC plate and grid voltages and currents, and the rf plate and grid currents, where these parameters are amenable to adjustment from the front panel of the supply. Thus, any electronic operating point can completely be determined during normal operation of the radiofrequency system.

The electrodeless arc lamp herein reported was attached to a vacuum/pressure system and mounted vertically within a short coil at the central (rf ground) end of the oscillator plate lines. The use of a lamp with tubulation rather than the use of several sealed lamps is preferable in the laboratory because it permits considerable latitude in the choice of discharge pressure, as well as enabling this parameter to be varied at will during lamp operation. Additionally, use of an unsealed lamp allows cryogenic recovery of used xenon after a test has been completed.

Lamp pressure was measured by means of a mechanical absolute-pressure gauge (Wallace and Tiernan Model 61B-1A-0500, 0-500 psia) which is permanently attached to the vacuum/pressure system. The system was evacuated by an EIMAC HV-1 diffusion pump during pre-fill purging operations. The lamp used in

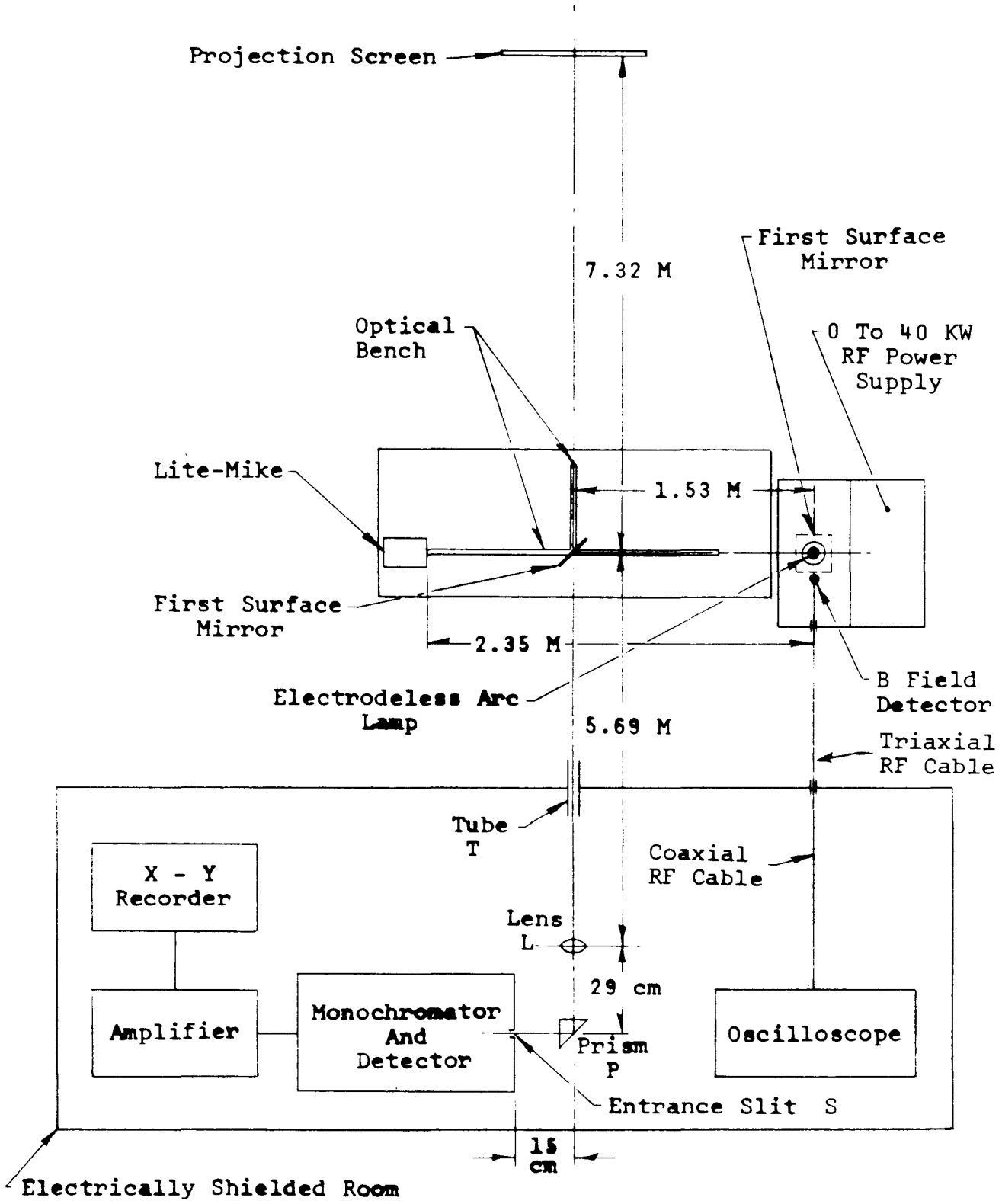

Figure 1. Experimental Layout

this investigation is a simple quartz sphere with diameter 38 mm and 1 mm wall-thickness. The discharge was observed along the optical axis through a first-surface aluminized mirror located directly above the discharge such that a view along the discharge axis is obtained.

A Perkin-Elmer Model 99 double-pass monochromator was employed for spectral measurements. This instrument was rigidly located in a fixed position inside an electrically shielded room.

The Perkin-Elmer instrument is equipped with a thermocouple detector and is conveniently provided with a 13 cps internal chopper. The thermocouple detector output is fed into a phase-locked amplifier where only the 13 cps component of the signal survives, and the amplified detector output is displayed on the vertical scale of a Hewlett-Packard X-Y Recorder, Model 7004A.

Average radiated power was measured with an EG&G Lite-Mike, Model 560 B, and illumination data were measured with a Weston Model 756 illumination meter. A thorough calibration of the optical diagnostic system was completed prior to the start of this experimental effort. This calibration is reported in detail in Appendix A.

3.2 EXPERIMENTAL TECHNIQUES

The observational procedures developed during the spectral calibration were applied directly to data acquisition during the actual experiment. Thus, electrodeless arc spectral data were obtained from the same distance as were the data of the calibration standard lamp, and only common optical elements were employed along the common path.

A typical spectral observation required several hours for its completion. A single sweep of the monochromator Littrow system at constant recorder gain settings was employed to generate an initial spectral distribution covering the range of electrodeless arc irradiance below 1.8μ. Selected portions of this distribution were examined next at higher gain settings to enable better structural resolution. Slit width and horizontal drive voltage were held fixed throughout the recording.

The observed intensity-position relationship was reduced to a true spectral irradiance distribution once key spectral characteristics were identified. The principal element sought in this phase of the identification process was a

positive identification of the xenon structure in the blue, especially of the two lines at λ4624 and λ4671, followed by the principal structural components at λ4734, λ4807, λ4830, λ4843, λ4917 and λ4923. These lines combine to produce an easily recognized signature that is characteristic of the electrodeless arc in xenon, from which the initial position-versus-wavelength determinations were made for a particular spectrogram. Secondary identification of spectral positions was accomplished by continuing the identification process from the blue into the infrared. Key lines sought were from the group λ6182, λ6318, λ6504, λ6882, λ7120, λ7643, and λ8232.

A nonlinear wavelength-scale, divided into 100 Å bands, was prepared from the results of the wavelength calibration. When a sufficient number of lines were identified on a raw spectrogram, the scale was superimposed, aligned with identified spectral positions, and a comparison made. Misidentities were accounted for, and the scale position was adjusted until spectral position agreement was obtained between the scale limits .35μ and 1.8μ. The spectrogram was marked at 100 Å intervals, and the area within each interval was evaluated redundantly by a) planimetry, b) square counting, c) direct measurement. These areas were tabulated at each wavelength interval, multiplied by their respective transfer functions*, and normalized to unity. The resulting transformed areas are proportional to the irradiance of the electrodeless arc source in their respective wavelength intervals. Irradiance was determined from a supplementary Lite-Mike reading.

Lite-Mike readings were evaluated in terms of the instrument calibration constant K_o, the relative response curve of the Lite-Mike, and the normalized spectral irradiance distribution obtained for a particular electrodeless arc discharge. The data processing techniques used were exactly those employed in the calibration, hence the Lite-Mike reading was a calibrated measure of the spectral irradiance of the xenon source.

A final check on both the accuracy and integrity of the irradiance measurement was provided by the comparison of Lite-Mike irradiance measurements in spectral bands (defined by calibrated filters) with values of irradiance in those bands derived from a numerical integration of the area under the irradiance distribution curve.

---

*The instrumental transfer function is defined and its measurement is described in Appendix A.

3.2.1 PROCEDURAL EXAMPLE: RUN C-1

The experimental procedure is demonstrated below for a 1 KW, 15 Mc discharge. This case is identified elsewhere in this report as Run C-1.

The discharge was initially struck at a pressure of a few millimeters of mercury, then the discharge pressure and DC plate power were adjusted to within a few percent of one kilowatt, at a static pressure of 20 psia. The following data were recorded at this reference operating point:

Date:	December 17	
Time'on':	3:25 PM	
Run Number:	C-1	
Reference Pressure:	20 psia	
Frequency:	15.5 Mc	
Plate Voltage:	1630 Volts	DC Values
Plate Current:	0.63 amperes	DC Values
Grid Voltage:	-90 volts	DC Values
Grid Current:	0.05 amperes	DC Values
Lite-Mike Readings		
(a) No filter:	6.75μA	
(b) RG780*:	4.75μA	
(c) RGN9*:	4.0 μA	

The discharge pressure was gradually raised, usually in increments of 10 psi. Discharge power controls were adjusted to maintain constant plate power. The discharge observables recorded at each pressure interval were:

Plate voltage
Plate current
Frequency
Lite-Mike Readings
(a) No filter
(b) RG780
(c) RGN9

Radiation production, as indicated by the observed Lite-Mike current, increased with increasing pressure, went through a maximum, then either stabilized or decreased as the pressure was raised past a certain critical value. No universal relationship between the radiation-production efficiency and any given pressure has been observed. The

---

*For filter passbands and transmission characteristics please see Appendix A, Figure A-7.

relationship observed during Run C-1 is presented in Figure 2. These data suggest that the most efficient operating point for this 15 Mc discharge at 1 KW is at 185 psia. The discharge parameters were then readjusted for 1 KW operation at 185 psia. The discharge observables recorded at this operating point were:

Plate voltage:	2060 volts	DC Values
Plate current:	0.49 amperes	
Grid voltage :	-125 volts	
Grid current :	0.09 amperes	
Frequency :	15.1 Mc	
Lite-Mike readings		
(a) No filter:	13.25μA	
(b) RG780 :	10.0 μA	
(c) RGN9 :	8.5 μA	

The spectral content of discharge radiation was examined next. A 94% reflecting, first-surface aluminized mirror was placed at the fixed "tee" of the optical bench, and rotated to such a position that the top view of the discharge could be viewed unobstructed from inside the shielded room through the aperture formed by the tube T shown in Figure 1. An image of the top view of the discharge was formed by the lens L at the entrance slit S of the monochromator after passing through the 90° prism P.

After setting and recording amplifier gain and damping response, slit width, and the drive motor speed, the first recording of the Run C-1 spectrum was made. All spectrograms were recorded on 11" x 17" vellum. Three additional spectrograms were obtained, two of which were restricted to the IR, the other being a relatively high-sensitivity spectrogram of the visible spectrum which became noise-limited in the vicinity of λ3900.

Upon completion of the spectral observation the mirror positioned at the optical bench "tee" was rotated through 90°, and a lens-aperture unit was installed upon the optical bench to form an image of the discharge top-view on the projection screen (see Figure 1). The distribution of illuminance at this image was observed and recorded. These raw data and a photograph of the discharge image are presented in Figure 3.

Run C-1 was terminated upon completion of the measurement of the illuminance distribution, at which time the equipment was shut down. The total operating time for Run C-1 was 3.4 hours.

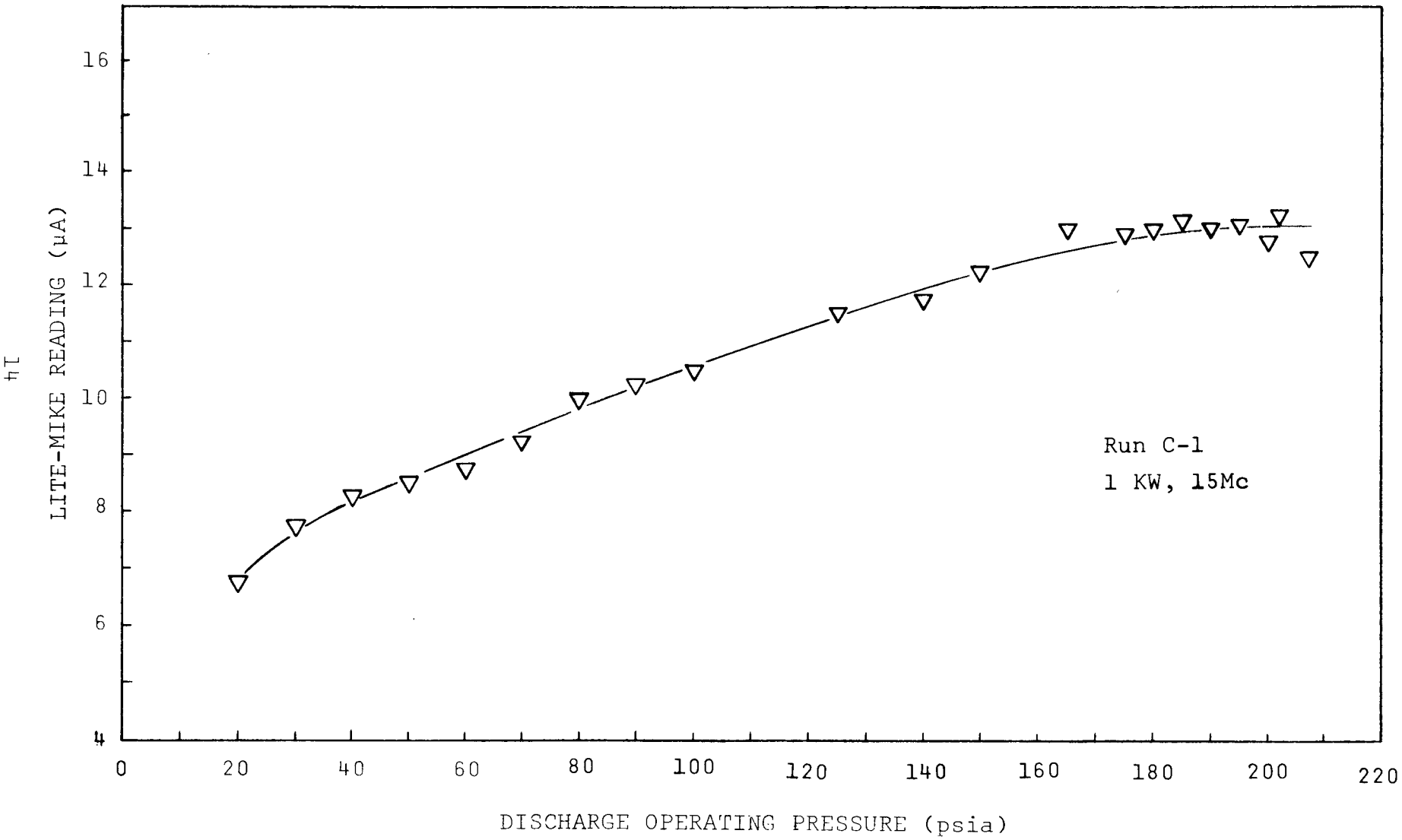

Figure 2. Radiation output as a function of discharge pressure.

	D	E	F	G	H	I	J	K	L
1	Values in foot-candles, measured at the projection screen.								
2									
3					0.4	0.5	0.5	0.6	0.5
4				0.5	0.3	0.3	0.5	0.5	0.3
5		0.4	0.3	0.7	3.3	5.3	5.9	5.7	4.5
6		0.3	1.7	5.8	6.6	6.1	5.9	5.9	6.2
7	0.3	1.2	6.0	6.4	5.4	4.7	4.6	4.7	5.1
8	0.3	4.0	6.7	5.1	4.3	3.6	3.2	3.3	4.0
9	0.4	6.1	6.1	4.5	3.5	2.5	2.0	1.9	2.7
10	0.7	6.4	5.7	4.3	3.1	1.9	1.3	1.2	1.9
11	0.6	6.1	5.6	4.3	3.1	1.9	1.2	1.1	1.6
12	0.3	5.2	6.0	4.7	3.8	2.6	1.8	1.5	2.1

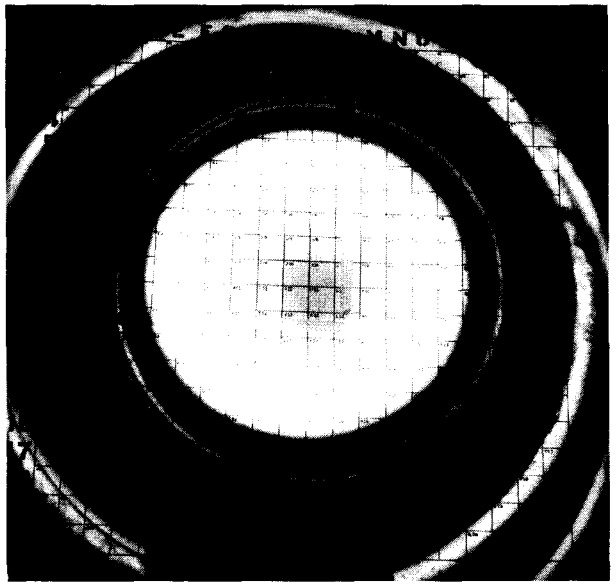

Figure 3. Illumination distribution and photograph of top view image of the discharge for Run C-1, (1 KW, 15 Mc).

3.2.2 DATA REDUCTION: RUN C-1

Observational data from Run C-1 were reduced as described previously, then tabulated for analysis. These data are described below.

3.2.2.1 SPECTRAL IRRADIANCE

The normalized irradiance distribution from this run is presented in Figure 4. Various pertinent raw data from the tabulation are presented in Table I. The amplitude of the irradiance distribution was derived from the Lite-Mike observation. This observation was made from a fixed position 235 cm from the discharge via a 94% reflecting first surface mirror. The effects of stray light were excluded from the measurement by nulling the instrument while the optical path (defined by two stops in series with the Lite-Mike detector head) was blocked from direct electrodeless arc radiation. At the time of the spectral observation the Lite-Mike indicated the following:

FILTER	CURRENT	INSTRUMENT/FILTER CONSTANT
None	13.25μA	$K_0 = 2.234 \times 10^{-2}$ μA/μW/cm^2
RG780	10.0 μA	$K_{780} = 2.857 \times 10^{-2}$ μA/μW/cm^2
RGN9	8.5 μA	$K_{N9} = 2.482 \times 10^{-2}$ μA/μW/cm^2

The technique developed from the Lite-Mike calibration* was used to evaluate the xenon irradiance distribution. The maximum amplitude of the irradiance curve ψ_{max} is found from:

$$I = \Sigma A(\lambda)R(\lambda) \cdot \psi_{max} K_o \qquad (16)$$

where I is the indicated Lite-Mike current, and $\Sigma A(\lambda)R(\lambda) = 3.217$ in^2 is given in Table I. Thus, from Eq (16) is found $\psi_{max} = 184.366$ μW/cm^{2}in^2, which is converted to absolute units when multiplied by the graphical scale factors (i.e., 1 inch vertical = $\psi_{max}/5$; 1 inch horizontal = 200 nm):

$$\psi_{max} = \frac{184.366}{40} \frac{\mu W}{cm^2 nm}$$

Taking the product of ψ_{max} and the total area under the irradiance curve $\Sigma A(\lambda)$, one obtains the net irradiance

---

*See Appendix A.

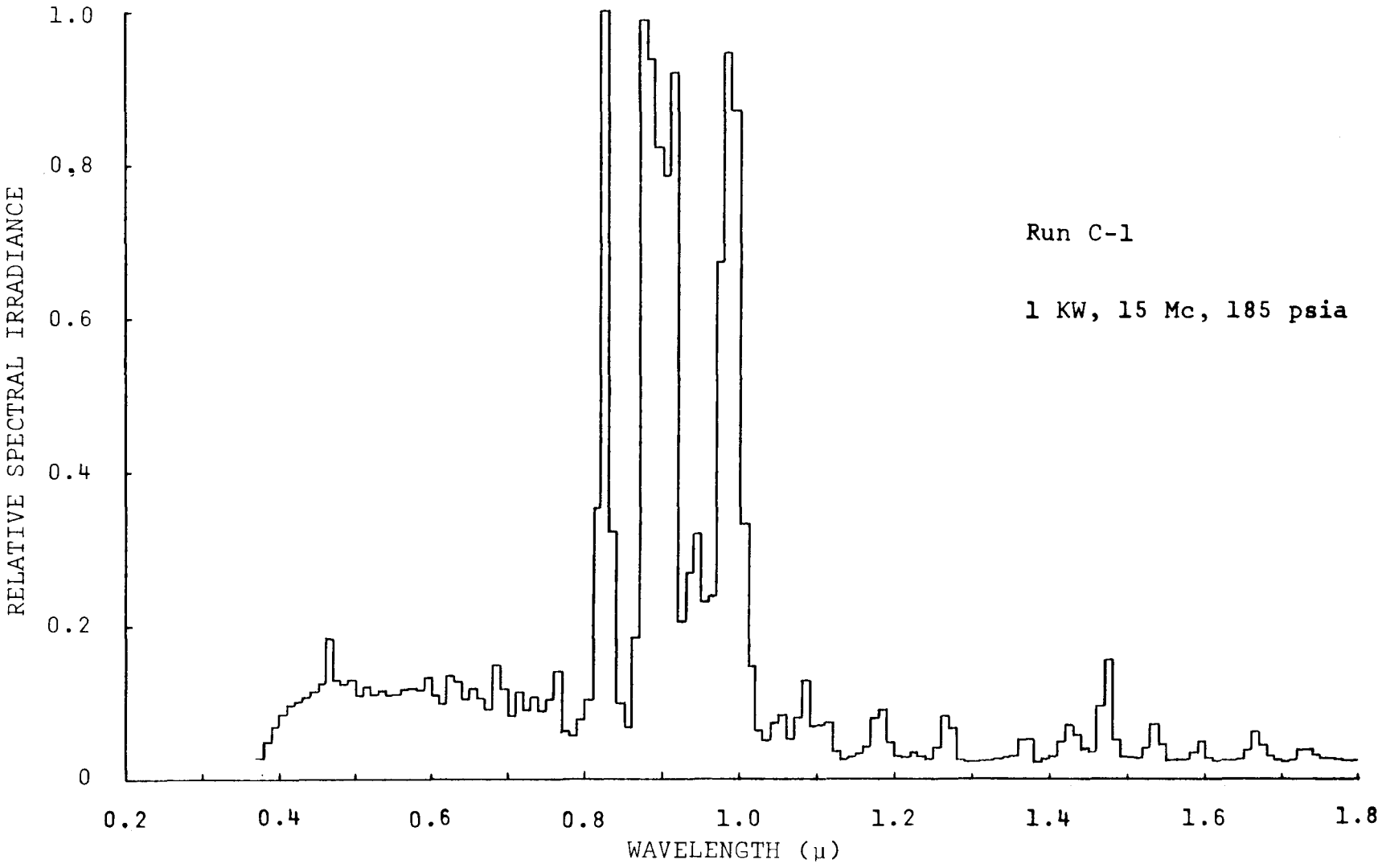

Figure 4. Normalized irradiance distribution of an electrodeless arc discharge in xenon.

TABLE I

NORMALIZED IRRADIANCE DATA FROM RUN C-1

Wavelength Interval $\Delta\lambda(\mu)$	Area Under Irradiance Curve $\Sigma A(\lambda)$ (in^2)
$< 0.4\mu$	0.037
$0.4\ \mu - 1.11\mu$	4.028
$0.78\mu - 1.10\mu$	2.925
$0.73\mu - 1.09\mu$	3.034
$0.37\mu - 1.8\ \mu$	4.753

$$\Sigma A(\lambda)R(\lambda) = 3.217 \text{ in}^2$$

$$\Sigma A(\lambda)R(\lambda) = 0.314 \text{ in}^2$$

$$\Sigma A(\lambda)R(\lambda)F_{780}(\lambda) = 2.153 \text{ in}^2$$

$$\Sigma A(\lambda)R(\lambda)F_{N9}(\lambda) = 1.955 \text{ in}^2$$

$A(\lambda)$ = an area per unit wavelength interval under the irradiance curve centered at λ;

$R(\lambda)$ = the relative response characteristic of the Lite-Mike at λ;

$F_{780}(\lambda)$, $F_{N9}(\lambda)$ = transmission of indicated filter at λ;

$V(\lambda)$ = coefficient of photopic luminosity function at wavelength λ.

$\Delta\Phi/\Delta A\big|_{TOT}$ in the band $0.37\mu \leq \lambda \leq 1.8\mu$:

$$\left.\frac{\Delta\Phi}{\Delta A}\right|_{TOT} = \psi_{max}\Sigma A(\lambda)\Delta\lambda = 8.763 \times 10^2 \mu W/cm^2.$$

The interval of response of the Lite-Mike with the RGN9 filter is $0.73\mu \leq \lambda \leq 1.09\mu$. The area under the irradiance curve in this band is 3.034 in^2 (Table I). The product of this area and ψ_{max} is the irradiance of the source in this band: $3.034\psi_{max} = 5.594 \times 10^2 \mu W/cm^2$.

The current indicated by the Lite-Mike when this instrument is used in conjunction with a filter is

$$I = \left.\frac{\Delta\Phi}{\Delta A}\right|_F \cdot K_F \frac{\sum_\lambda A(\lambda)R(\lambda)F(\lambda)}{\sum_\lambda A(\lambda)}$$

Using the filter RGN9, the Lite-Mike current was 8.5μA. The indicated irradiance in the response band is

$$\frac{\sum_{N9} A(\lambda)}{\sum_{N9} A(\lambda)R(\lambda)F(\lambda)} \cdot \frac{I}{K_{N9}} = 5.315 \times 10^2 \mu W/cm^2$$

which compares within 5.25% of the directly integrated value.

3.2.2.2 LUMINOUS INTENSITY

The product of the irradiance distribution and the photopic luminosity function is given by $\Sigma A(\lambda)V(\lambda) = 0.314$ in^2. Multiplication of this area by ψ_{max} yields an irradiance of 57.89μW/cm^2 (i.e., "light watts" x $10^{-6}/cm^2$), which is equivalent to 36.575 lumens/ft^2. The viewing distance was 7.71 ft (235 cm), hence the solid angle subtending one square foot at the viewing distance is 0.0168 steradians. Thus, $\Sigma A(\lambda)V(\lambda)$ equals 36.575 lumens per 0.0168 steradians, or 2177 candelas.

The illuminance distribution of Run C-1 presented in Figure 3 can be integrated to provide an independent evaluation of the luminous intensity of the top view of this discharge.

The luminance B of the source is given by

$$B \approx \frac{4S^2}{\pi T d^2} E ,$$

where S is the distance in feet from the detector to an aperture of diameter d mm, at which is located a lens of transmission T. If E is measured in footcandles, B has the dimensions cd/mm^2.

In the actual laboratory situation a pair of 94% reflecting mirrors were part of the optical path and their effect must be included in T. The lens employed had a measured transmission (visible) of 0.975. The effective transmission was (.94)(.94)(.975) = 0.86. For d = 46.3 mm and S = 27.33 ft, the relation between source luminance and measured illuminance is

$$B \approx 0.515 \; E \; cd/mm^2 .$$

The magnification of the system was 22:1 so that illumination measurements taken at two-inch intervals on a rectangular grid at the projection screen correspond to a resolution element 2.31 mm x 2.31 mm at the source. The luminous intensity I of the discharge top view can be obtained by summing over the source resolution elements, and is given by

$$I = (2.31)^2 \times 0.515 \; \Sigma E(x,y) \; cd,$$

where the summation is over the entire spatial illuminance distribution. Circular symmetry allowed the observed quarter distribution to be multiplied by four, where the appropriate boundaries were found by comparison of the photograph of the image with the recorded distribution. In Run C-1, the summation $\Sigma E(x,y)$ yields 197.4, hence the luminous intensity is 2168 cd which agrees with the value 2177 cd obtained by direct integration of the irradiance distribution.

3.2.2.3 NET RADIATION PRODUCTION

The electrodeless arc polar radiation distributions observed thus far indicate that the electrodeless arc discharge has essentially a uniform spatial irradiance distribution except at its top (and presumably at its bottom) where the effects of the off-axis peak in plasma temperature are evidenced by an off-center peak in the source brightness distribution, and an on-axis minimum of radiation production. Observations

of electrodeless arc radiation from stations at polar angles θ between 0° (the zenith angle) and 20° yield measurements of irradiance which are low (compared to the uniform value observed where $\theta>20°$) by about 13% at 0°.

A polar radiation distribution function $\xi_o \Sigma K(\theta)\sin\theta$ (where ξ_o is a dummy parameter--brightness, irradiance, etc.--) evaluated at $\theta>20°$, and $K(\theta) = 1$ for $\theta>20°$) is derived from observational data and presented in Appendix B. This function is incorporated in the calculation of radiant flux as follows:

$$\Phi = \int \frac{d\Phi}{dA}\, dA \approx 4\pi r^2 \Delta\theta \left.\frac{\Delta\Phi}{\Delta A}\right|_o \Sigma K(\theta)\sin\theta,$$

where r is the observation distance, $\Delta\theta$ is a constant angular increment equal in the present experiment to 0.08726 radians (i.e., 5°), and $\Delta\Phi/\Delta A_o$ is the uniform source irradiance observed at $\theta>20°$. The "uniform" irradiance is simply the 0° value divided by 0.868 (i.e., the 13% correction), including reflection loss.

In Run C-1, r = 235 cm., and irradiance measured at θ = 0° was $8.765 \times 10^2 \mu W/cm^2$, which corresponds to the "uniform" irradiance $\Delta\Phi/\Delta A_o$ of $1.00098 \times 10^3 \mu W/cm^2$ at polar angles greater than 20°. Thus, the net radiant flux is given by

$$\Phi_R \approx 4\pi r^2 \Delta\theta \left.\frac{\Delta\Phi}{\Delta A}\right|_o \Sigma K(\theta)\sin\theta \approx 730 \text{ watts}.$$

Likewise, the net luminous flux Φ_L was found by a similar process, because the spatial radiation distribution of luminance is the same as that of irradiance (Appendix B):

$$\Phi_L \approx 4\pi r^2 \Delta\theta L_o \Sigma K(\theta)\sin\theta \approx 32{,}749 \text{ lumens},$$

where L_o is the uniform luminous flux which is observed at polar angles greater than 20°.

The overall efficiency in the conversion of electrical power to radiation for Run C-1 was 72.91%. The luminous efficacy was 32.46 lumens/watt.

SECTION 4

EXPERIMENTAL RESULTS AND DISCUSSION

The final results of the spectral survey of the electrodeless xenon lamp are presented in Table II, where each of the eleven main data runs is identified by name, applied power level, discharge pressure, and induction field frequency. Applied power was measured at the plate of the radiofrequency generator and is equal to the product in watts of the DC plate voltage and current. Total radiated power was measured between the limits 0.37μ and 1.8μ. The computed efficiency of conversion of DC plate power to rf power was 84%. Observed net power conversion efficiencies had values between 42.5% and 76.8%.

In each case relative Lite-Mike indications (both with and without filters) and relative illuminance and brightness measurements have been intercompared for consistency with data derived by means of integrations under the appropriate spectral irradiance curve. The absolute magnitude of irradiance was independently determined in each case from the Lite-Mike reading obtained at the time at which the individual spectrogram was recorded.

Instrumental and observational errors and uncertainties associated with data reduction and processing yield an overall uncertainty of ±10% in the tabulated discharge properties. The spectral irradiance distributions from which these data have been derived appear in Appendix C.

4.1 OPERATIONAL CHARACTERISTICS OF THE ELECTRODELESS ARC LAMP

The principal criterion employed in the evaluation of lamp performance is the net conversion efficiency of electrical power into optical radiation.

The effects of pressure, frequency, power, coupling and rf technique are intimately related to the power conversion efficiency observed in any given discharge. These effects

TABLE II

SUMMARY OF PARAMETRIC STUDY

Run I.D.	DC Power Level W (watts)	Pressure (psia) / Frequency (Mc)	Total Radiated Power R (watts)	Net Efficiency (= R/W)	RF Efficiency (= R/RF Power)	Power in Near IR (watts) (.73μ ≤ λ ≤ 1.09μ)	% of Total Power in Near IR	Power in Visible Part of Spectrum (watts)	% of Total Power in Visible Part of Spectrum	Luminous Flux (lumens)	Luminous Efficacy (lumens/watt)
SL-1	1020	165/25	493	48.3%	57.5%	313.6	30.8%	108.1	10.6%	19,911	19.52
BL-1	1011	190/25	661	65.4%	77.8%	409.2	40.5%	145.6	14.4%	26,862	26.57
C-1	1009	185/15	729	72.2%	86.0%	445.8	44.2%	171.4	17.0%	32,749	32.46
C-2	2520	170/15	1470	58.3%	69.4%	874.2	34.7%	355.2	14.1%	73,244	29.07
B-1	1008	175/54	575	57.0%	67.9%	348.5	34.6%	147.2	14.6%	29,455	29.22
B-2	2520	210/54	1539	61.1%	72.7%	937.4	37.2%	366.8	14.6%	92,476	36.70
A-1	996	140/25	716	71.9%	85.6%	434.4	43.6%	179.1	18.0%	37,048	37.18
A-2	2522	165/25	1938	76.8%	91.5%	1156.2	45.8%	465.8	18.5%	97,748	38.76
SC-2	2000	155/25	1364	68.2%	81.2%	794.4	39.7%	366.9	16.8%	72,608	36.30
SC-1	1020	148/25	688	67.5%	80.3%	435.9	42.7%	149.7	14.7%	30,467	29.87
W-1	1027	140/25	436	42.5%	50.5%	312.8	30.5%	103.1	10.0%	20,502	19.96

are not rigorously separable in the mathematical sense, but observation of lamp operation over extended periods of time and under varying conditions of operation provides physical intuition rigorously justifiable on statistical grounds. The observed effects of operating pressure on electrodeless arc lamp efficiency and performance are demonstrated throughout this Section, where pressure has been treated as the independent variable.

4.1.1 EFFECTS OF RADIAL CONDUCTIVE HEAT FLUX

As stated in Section 2 the most important determining factor of the power conversion efficiency of an electrodeless arc lamp is the effect of the lamp's envelope on the energy balance of the discharge. High-pressures are favorable to the constriction of the discharge from the envelope wall, hence power conversion efficiency increases with pressure because (among many other reasons) radial heat transport by conduction to the wall decreases with pressure due to the smaller discharge size. This is clearly shown in Figure 5 where normalized observations of discharge radius and radiation production are presented as functions of pressure for a discharge at constant power.

The effect of heat conduction to the wall is demonstrated most clearly in Runs SL-1 and BL-1, where discharges were generated and evaluated under conditions identical within a few percent except for the size of the lamp employed. The diameter of the lamp in SL-1 was 3.2 cm. while the diameter of the lamp of BL-1 was 4.1 cm.; the lamps employed throughout the remainder of this program had diameters of 3.8 cm., where the nominal wall thickness was 1 mm.

The effects of a "poor" induction coil surface lead to extreme degradation of lamp radiation efficiency, as will be demonstrated. The coil employed in Runs SL-1 and BL-1 was highly oxidized and both runs exhibit low efficiencies as a direct consequence. The efficiency of the large lamp (BL-1) was in excess of 30% greater than that of the small lamp (SL-1), however, which is due almost entirely to the reduction of heat conduction to the wall in the large lamp

Radial conduction losses will decrease as the wall temperature is raised. Most examples observed during this survey involved discharges in which wall-conduction losses ranged from "minor" to "negligible", so no effort was made to study efficiency enhancement through increases in wall-temperature. An exercise of considerably more interest

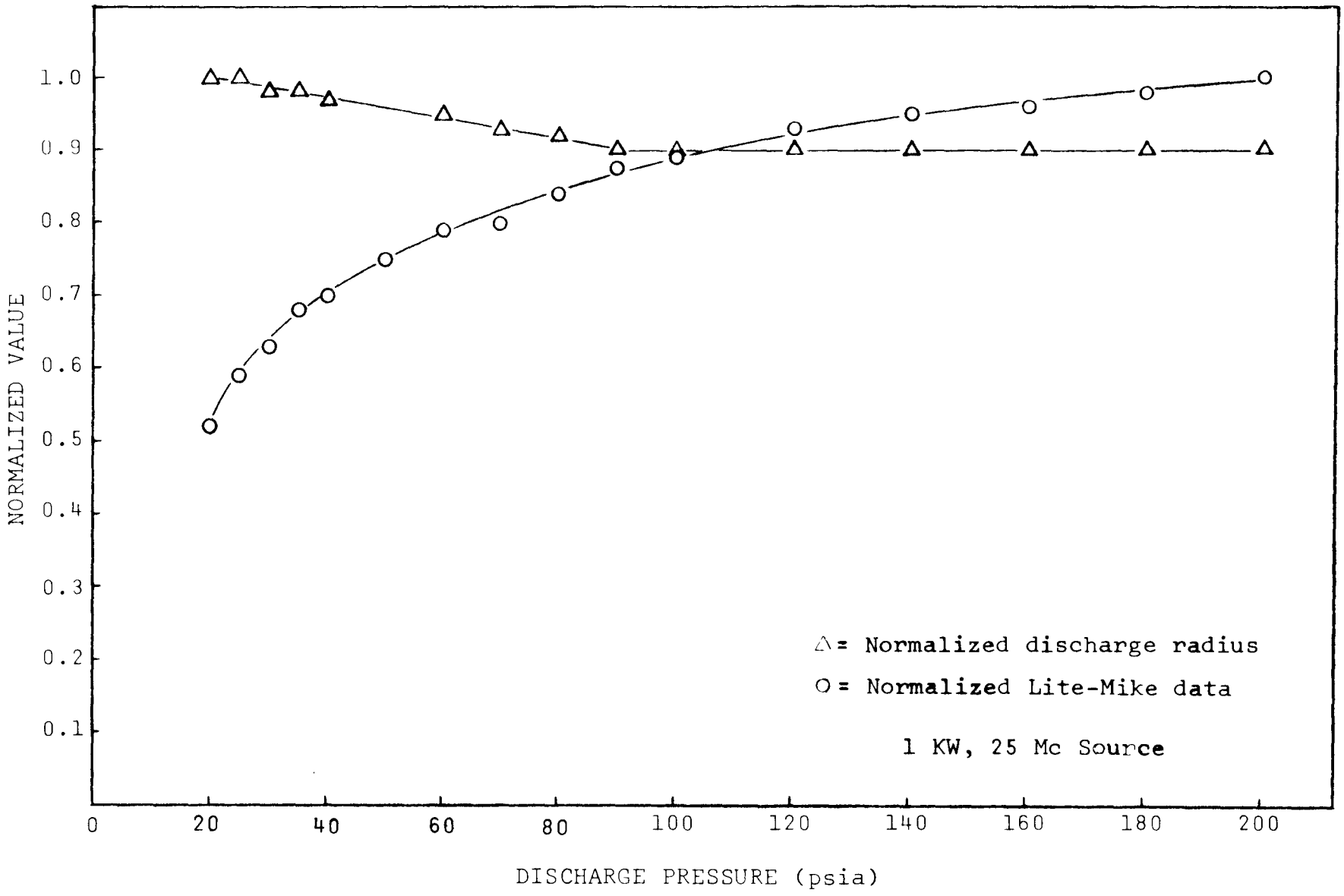

Figure 5. Normalized radiation output and discharge radius as a function of discharge pressure.

was provided by the employment of a standard-sized lamp in a water-cooled quartz jacket, in the experiment of SL-1 and BL-1, such that the wall temperature could be lowered through several hundred centigrade degrees, to allow the study of efficiency degradation through a decrease in wall-temperature.

Maintenance of such an artifically low boundary temperature would be expected to seriously degrade the performance of any thermal system. That this indeed is the case for the electrodeless arc lamp is evident from the results of Run W-1. Irradiance data for this example (Appendix C) show that absorption of lamp radiation by the cooling water increases from a few percent over most of the visible spectrum, to totality at 1.4μ, hence some care in the interpretation of wall effects is required. Comparison of the water cooled lamp radiation efficiencies observed in the near-IR and visible (where absorption is not too important) with those of Run SL-1 shows that the effect of forced-cooling of the discharge envelope was essentially the same as the effect of the small lamp envelope. Because of enhanced conductive heat transport, lamp performance is seriously degraded by the presence of a cool wall.

The importance of minimizing conductive losses from an electrodeless arc discharge is made obvious by the preceding examples. The criteria for lamp operation which tend to reduce conductive power losses in an electrodeless arc lamp are:

(1) Large ratio of lamp diameter to discharge diameter,
(2) High-pressure operation, and
(3) "Hot" envelope.

4.1.2 EFFECTS OF CIRCUIT TECHNIQUES AND COUPLING

An important prerequisite to the achievement of high-performance, high-efficiency operation of an electrodeless arc lamp has been found to be excellence in the circuit techniques employed in the apparatus used to generate the radiofrequency power and transmit it to the discharge. The radiofrequency generator used in the present program was originally designed to operate at a point which yields 84% plate efficiency (per tube). Push-pull operation was employed to raise the effective plate efficiency by about four percent. The maximum radiation efficiency observed during this study was about 77%, hence, a considerable fraction (i.e., ~90%) of the available radiofrequency power was recovered in the spectral region between 0.37μ and 1.8μ.

The remainder of the power is accounted for by radial heat transport within the lamp, ohmic heating of the induction coil, rf radiation, and optical radiation outside the observed spectral region.

The extent to which the circuit itself determines the characteristics of the discharge is by no means obvious.

The radiation efficiency observed in every example exhibited a strong dependence on the condition of the surfaces of the induction coil and its transmission line. Efficient circuit operation is favored by clean, polished, oxide-free, highly conductive (i.e., silverplated) surfaces. Failure to silverplate the induction circuit has been observed to reduce the maximum observed efficiency of power conversion by a minimum of 10%, most often considerably more. Electrodeless arc lamp performance is degraded by oxides, roughness, and foreign material (i.e., solvent, fingerprints, etc.) on or at the induction coil surface.

An excellent case in point is given by the construction, configuration, and material of the induction coil itself. In general, during this program induction coils were wound from ¼ inch copper refrigeration tubing. For 25 Mc operation, four turns wound about a two inch diameter form were found to be adequate. Employing this coil, Lite-Mike measurements of discharge radiation at constant power input as a function of discharge pressure were made through appropriate stops from a fixed position on an optical bench. These data appear as open circles in Figure 6. An identical coil was wound and installed after having first been thoroughly cleaned and heavily silverplated, and similar measurements were made using the same apparatus in the same configuration as before. These data appear as triangles in Figure 6. In both cases the power was fixed at one kilowatt. The latter observations correspond respectively to Lite-Mike currents on the order of 70% greater than former observations. Since the Lite-Mike current is a measure of radiated power, one concludes that the use of a silverplated coil results in a dramatic increase in radiated power, when all other parameters are held fixed.

The silverplated coil was again employed in a repeat of the preceding measurement sequence some twenty days later. These data appear as dark circles in Figure 6 and are seen to be somewhat lower than the preceding observations. The later data are described in the present report under Run A-1.

Run A-2 immediately followed Run A-1, employing the same lamp and induction coil as before. The power level was raised to

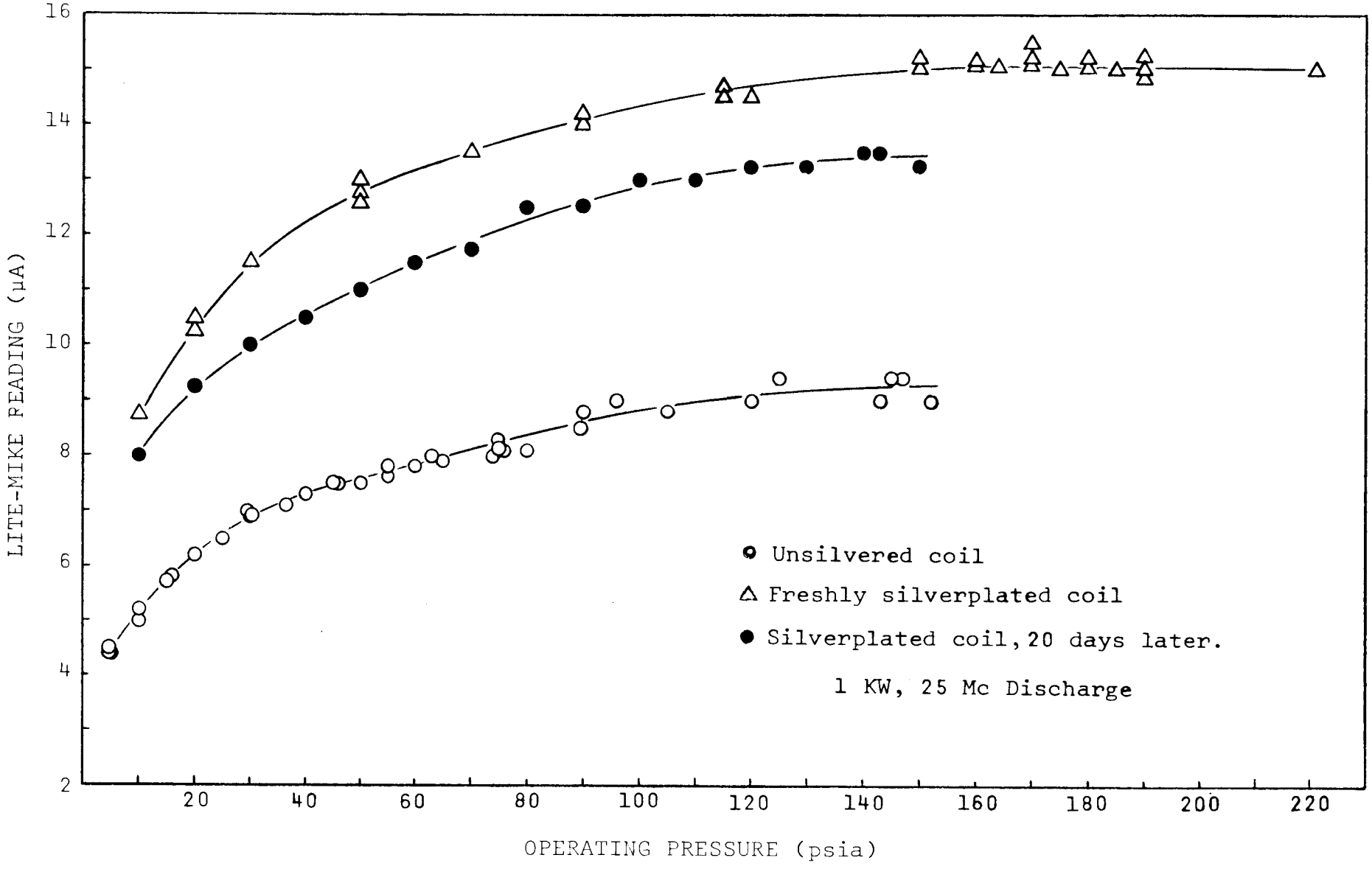

Figure 6. Effect of induction coil silverplating on lamp radiation output.

2.5 KW and maintained at this level for 3.5 hours while data were taken. Upon completion of Run A-2 several data points at the 1 KW level were spot-checked. It was found that, as a function of discharge pressure, the observed power as indicated by the Lite-Mike was approximately twenty percent lower than the equivalent data points previously observed in Run A-1.

This spectacular loss of operational efficiency eventually was traced to severe oxidation of the silverplated induction coil, which apparently resulted from its proximity to the electrodeless arc lamp during 2.5 KW operation. Parts of the coil had actually turned black during the 2.5 KW run. The slight decrease in efficiency observed after the initial twenty day period evidently was due to ordinary surface oxidation of the silverplated coil. An occasional scrubbing of silverplated coils in a silver-cyanide bath was found adequate to eliminate much of this effect.

An additional example of the effects of radiofrequency circuit techniques on lamp performance is given below, where the effect of coupling on discharge performance is described.

An induction coil was especially fabricated for use in the polar radiation study described in Appendix B. For purposes of the intended measurement, the coil was wound on a smaller than normal form, and the final coil diameter was 8% smaller than the coil diameter usually employed. The intent was to blacken this coil with ultra-flat black enamel, so a heavy silverplate was not applied.

Prior to darkening the coil, two observational runs were made with it in order to determine whether or not appreciable effects of tighter coupling with the discharge would be observed. The characteristics observed for one of these runs (SC-1) appear in Table III, and in Figure 7 they are compared with similar observations of a comparable discharge in which a larger, well-silvered coil was used (Run #10) These latter data are tabulated in Table IV.

Several important features of electrodeless lamp performance are clearly demonstrated by these data. The discharge employing the silvered coil was significantly more efficient in converting rf power into radiation than was the unsilvered coil. The power differential was due to the lower efficiency of the smaller coil. Part of this power was dissipated in the coil itself, thus raising the coil's temperature which increased its rf resistance and lowered the circuit Q, which ultimately increased the rf generator plate loss.

TABLE III

CHARACTERISTICS OF "SMALL COIL" DISCHARGE

AS FUNCTION OF ABSOLUTE PRESSURE

(Run SC-1 Unsilvered Coil)

Pressure (psia)	Power (Watts)	Total Radiation (Watts)	Total Lumens	Lumens/ Watt	Net Efficiency
20	1012	413	21034	20.79	40.8%
30	1008	454	22759	22.58	45.0%
40	1008	509	27069	26.85	50.5%
50	994	551	28793	28.97	55.4%
60	1015	592	27931	27.52	58.3%
75	1015	619	30172	29.73	61.0%
100	1029	661	31897	31.00	64.2%
125	1036	674	31552	30.46	65.0%
150	1028	688	31379	30.52	66.9%
153	1021	688	31379	30.73	67.4%
175	1018	674	34310	33.70	66.2%
155	2000	1294	64483	32.24	64.7%

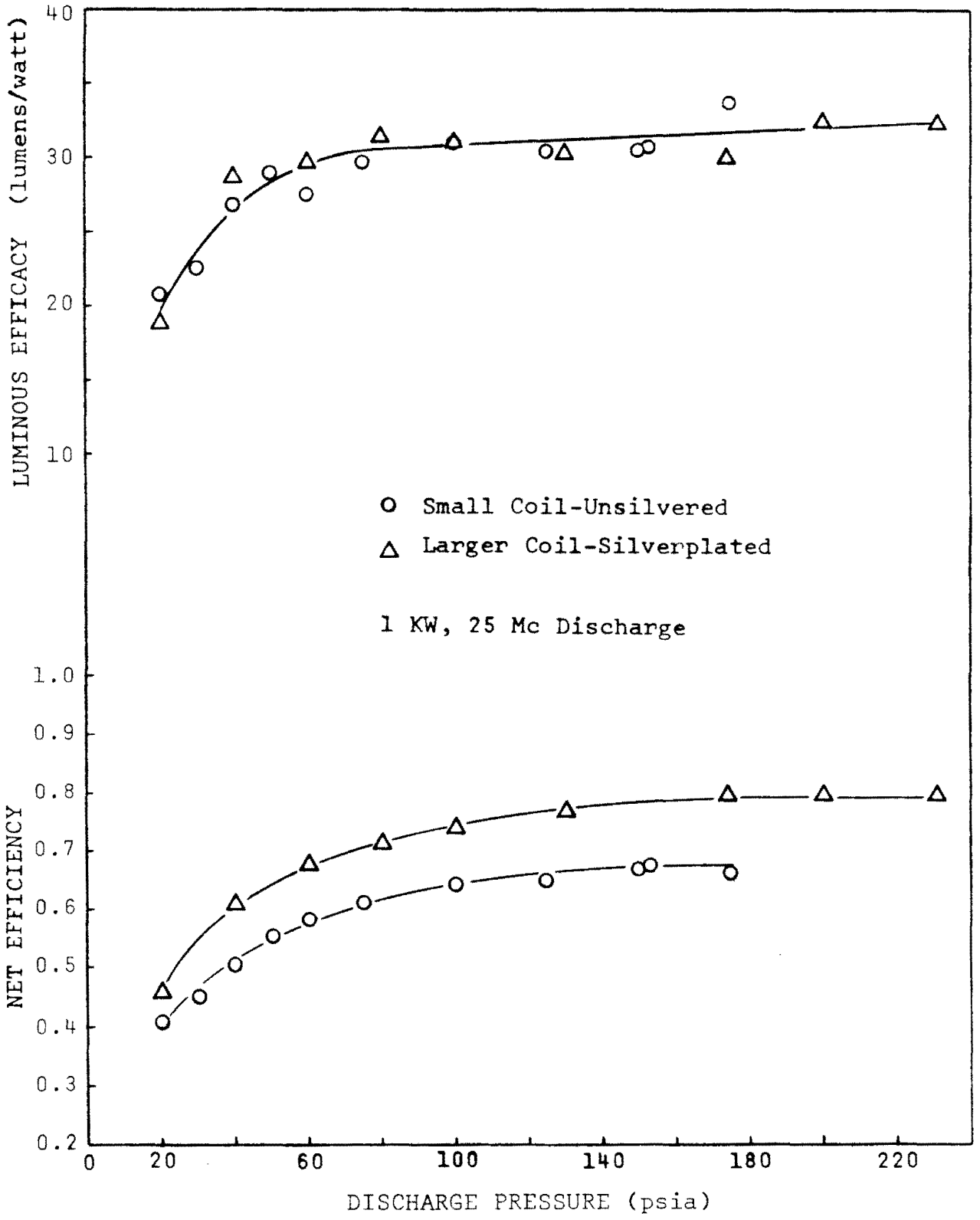

Figure 7. Comparison of effects of tighter coupling and coil silverplating on luminous efficacy and net efficiency.

TABLE IV

CHARACTERISTICS OF 25MC ELECTRODELESS ARC

(Run #10 - Silverplated Coil)

Pressure (psia)	Power (Watts)	Total Radiation (Watts)	Total Lumens	Lumens/ Watt	Net Efficiency
20	1037	482	19483	18.79	46.5%
40	1040	633	29828	28.68	60.9%
60	1040	702	31034	29.84	67.5%
80	1040	743	32759	31.50	71.4%
100	1040	771	32241	31.00	74.1%
130	1040	798	31552	30.34	76.7%
174	1040	826	31207	30.01	79.4%
200	1042	826	33793	32.43	79.3%
231	1040	826	33793	32.43	79.4%

The tighter coupling between the smaller coil and the discharge is reflected in the luminous efficacy of the small coil discharge, which is essentially equal to that of the more efficient discharge. This is possible because tighter coupling produces a smaller discharge, everything else being held constant. Even though the tightly-coupled discharge dissipated less power than the more efficient discharge, that power was dissipated in a smaller volume and yielded a greater plasma energy density, and produced a higher radiation temperature than would be expected on the basis of relative dissipation alone.

Additional performance data were obtained from the blackened small coil. In an experiment performed subsequent to the polar radiation distribution measurements, the illumination produced by the discharge in the blackened small coil was sampled from a polar angle of 22°. The data presented in Table V were obtained for a fixed discharge pressure of 153 psia.

These data are seen to be about 30% low at 1 KW, and 14% low at 2 KW, relative to the observations previously tabulated in Table III. In this case the cause was found to be the black enamel used to darken the coil. Several hours' exposure to the operating electrodeless arc lamp completely carbonized the paint on the coil, producing a surface which was, in an electrical sense, the opposite of that desired for efficient operation of an electrodeless arc lamp.

One aspect of radiofrequency technique that was recognized but not fully appreciated during the design phase of the 15 Mc segment of this study was the effect of the distributed capacitance of the induction coil on lamp performance.

Reduction of the resonant frequency of the rf generator to 15 Mc was accomplished by extending the length of the plate transmission line by approximately a factor of two relative to its length at 25 Mc. Space limitations required that the extended line be folded, so the final resonator was formed by winding a double-layer solenoid. The geometry of this winding is such that appreciable distributed capacitance exists between adjacent turns, and additional capacity exists between layers-of-turns, especially at the terminal ends which are positions of high relative potential. The resonator was thoroughly cleaned and heavily silverplated prior to its use in Run C-1 at a power level of one kilowatt.

The data of Run C-1 were obtained at a very efficient

TABLE V

VISIBLE RADIATION PRODUCED WITH BLACKENED SMALL COIL

Applied Power (Watts)	Illumination (lumens/ft^2)	Luminous Flux (lumens)	Luminous Efficacy (lumens/watt)
890	130	20,744	23.34
1216	195	31,161	25.63
1344	225	35,955	26.75
1523	260	41,548	27.28
1638	285	45,543	27.80
1814	315	50,337	27.75
2000	355	56,729	28.36
2310	430	68,714	29.75
2700	510	81,498	30.18
3136	630	100,674	32.10

operating point. An overall power conversion efficiency of 72.2% was observed, indicating that only fourteen percent of the radiofrequency power was lost to wall conduction, rf radiation, and other sources of inefficiency. The luminous efficacy of the lamp in Run C-1 was 32.46 lumens/watt. Prior experience and observations of the performance trends of other discharges suggested that, on the basis of Run C-1 data, the operational efficiency of Run C-2 (2.5 KW) should be between 75% and 78%, and a luminous efficacy between 40 and 41 lumens per watt should be realized. Contrary to expectation, the values observed respectively were 58.3% and 29.07 lumens per watt.

Two attempts to repeat Run C-2 failed when a high frequency arc developed across the high potential points of the induction coil. Reproduction of Run C-1 data could be accomplished without difficulty. When the cause of the poor performance of the system at the higher power level was identified, attempts to observed "better" data at 2.5 KW and 15 Mc were abandoned.

The capacitive energy stored in a single-layer solenoid is relatively small--at most, a few percent. Addition of a second winding atop the first increases the self-capacitance of the inductor considerably. The fraction of the total energy stored by the coil that is contained in the coil's electric field (i.e., the capacitive part of the coil's energy storage) depends not just on capacitance, but on the square of the coil's potential distribution function as well. The construction of the double layer 15 Mc coil was such that the positions of highest potential were the same as the positions of highest capacitance. At the low power level the main consequence of the high-capacitance winding was only minor enhancement of the capacitive energy stored by the coil, which evidently had little or no effect on the performance of the lamp in Run C-1. At the higher power level enough energy was stored in the coil's capacitance to cause flashover and a catastrophic rf breakdown across the coil (i.e., three identical coils were constructed, two were completely destroyed by high-voltage arcing). Quite evidently, rf flashover is preceded by corona and a large dielectric loss, and this behavior is almost completely determined by the local potential distribution. Thus, the poor performance observed in the 15 Mc, 2.5 KW experiment (Run C-2) was a direct consequence of the use of a high-capacitance resonator with an unsuitable potential distribution. Attempts to improve performance at this operating point were stopped because such improvement required a complete redesign and changeover of the rf system to one employing lumped circuit elements.

4.1.3 EFFECTS OF OPERATING POWER AND FREQUENCY

The effects of operating power and frequency on electrodeless arc lamp performance are considered. Runs A-1, A-2, B-1, B-2, and C-1 indicate trends which yield improved lamp performance and higher operational efficiency with either decreasing frequency, or increasing power, or both. The trend would be much more obvious if Run C-2 had not been influenced by such high electronic-system losses, and if complete uniformity in induction-coil fabrication and silverplating had been achieved throughout the duration of the experimental program. Nevertheless, all competing effects are believed to have been evaluated. Higher frequency discharges tend to have larger diameters than lower frequency discharges when pressure, power and lamp size are held constant, but the actual change in diameter is relatively small (for two-fold frequency changes the diameter change is only about ten percent, or less). This size-change is believed to be the main element contributing to improved lamp efficiency at lower frequencies. A secondary effect leading to improved performance may be the change in the discharge temperature profile predicted[3] by solutions to the energy balance equation, although this has not been established in the present study.

Higher power operation yields hotter discharges, and the efficiency of thermal radiation processes improves with temperature. Thus, the efficiency of the electrodeless arc lamp would be expected to improve with any power increase, as has been observed in this study.

4.1.4 LAMP RESONANCES AND INSTABILITIES

Experimental xenon lamps employed throughout this study were unsealed to enable their operation at various pressures. Filling took place through a three inch capillary tube with a one mm bore which served as the lamp stem. Pressure-sealing of the stem was accomplished mechanically by means of a neoprene gasket. A 1/8 inch gate valve was mounted approximately one inch below the seal to isolate the lamp from its fill system.

Operation of a lamp at static pressures in excess of 100 psia at powers greater than 1 KW is often characterized by a slight flickering in the central region of the discharge. The flicker increases in intensity with increases in discharge pressure, often decreases in intensity with increases in applied power, and can be stopped by closing the isolation valve. Flicker has been observed to increase in

intensity and decrease in frequency with increases in the lengths of the stems of unsealed lamps; however, no such flicker has been observed in a sealed-off lamp.

This flicker is believed to be a manifestation of an acoustic resonance in which a mild pressure wave oscillates between the stem capillary tube and the spherical lamp, and is assumed to be similar to the organ pipe in its physical description.

If the lamp pressure is raised to a sufficiently high, power-dependent value, and if the isolation valve is left open, the plasma occupying the central region flickers between a "full-on" state and a "full-off" state in a spatially asymetric, apparently random fashion. This occurs under conditions which suggest that the pressure pulse is sweeping plasma out of the central volume at a rate considerably greater than plasma can re-enter the volume by diffusion (i.e., the induced electric field, hence the current density and ohmic heating vanish identically at $r = 0$). As in its milder form, this resonance stops upon closure of the isolation valve, and has not been observed in sealed-off lamps.

When the applied power is increased to the two-to-three kilowatt level, the discharge appears to begin a rotational motion with what appears to be a uniform angular velocity which increases with increasing power. This apparent motion vanishes at static pressures below about ten atmospheres. The rotating discharge remains constricted from the wall, gives every evidence of being spatially "stable", and does not appear to be accompanied by a decrease in light output. As the static pressure is raised to twelve-to-thirteen atmospheres, the rotating discharge becomes violently unstable and appears to tumble while rotating. Light output diminishes and large excursions in the indicated pressure are observed. Still photographs of the projected image of a discharge exhibiting this instability are presented in Figure 8 where the deformation of the normally azimuthally-symmetric discharge shape is apparent.

This instability cannot be halted by closing the isolation valve, nor has it been established that it is or is not coupled to the organ-pipe resonance. While it is believed that the origin of this instability is purely hydrodynamic, hydromagnetic effects may be present which couple the Lorentz body force $\underline{j} \times \underline{B}$ (which is always directed radially inward) to plasma mass-motion through any pressure and field gradients which may exist in the discharge. Effects similar to those observed would be possible through such

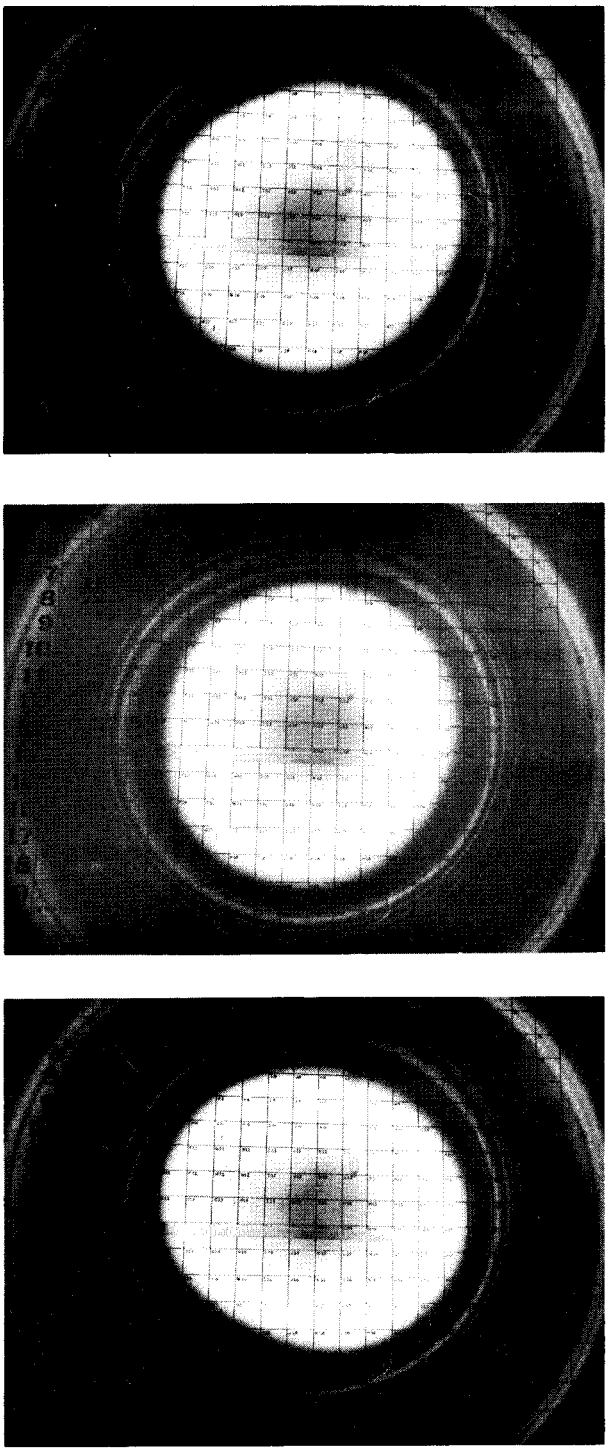

Figure 8: Photographic study of rotational instability in a 3 KW, 190 psia xenon discharge, viewed along the polar axis.

coupling, and triggering of the violent instability could easily result from something as mild as the organ-pipe resonance, even with the isolation valve closed.

4.1.5 LAMP FAILURES

This section has been prepared with the thought that post-mortem examinations of lamp-failures may yield enough information about the cause to prevent future failures.

The following tabulation traces the history of a single lamp at a constant pressure of 11 atmospheres as the power was raised through 5.5 kilowatts:

Applied Power (Watts)	Total Power Radiated (Watts)	Net Efficiency (%)	Luminous Flux (Lumens)	Luminous Efficacy (Lumens/Watt)
1045	578	55.3	28,276	27.1
1879	1225	65.2	57,759	30.7
2620	1763	67.2	81,552	31.1
3546	2395	67.5	113,966	32.1
4290	3028	70.6	146,552	34.2
4884	3524	72.1	162,931	33.4
5580	3883	69.6	182,414	32.7
>5580 - failure.				

The failure was sudden, and no piece of the quartz lamp larger than about 2 mm^2 was recovered.

In this example the failure was due to inadequate cooling of the lamp. The failure was preceded by a decrease in radiation efficiency observed when the applied power was raised past 4884 watts.

Subsequent observations have shown that a lamp initally softens and expands before it fails. The loud report and pulverized quartz that occasionally accompany a failure result from the plate circuit filter capacitor discharging its considerable stored energy across the induction coil along a path formed by the expanding xenon plasma from a lamp that has already ruptured. (The energy stored in the filter capacitor just prior to the 5.58 KW failure was 2.268 kilojoules: 3600 V, 350μfd). Decreasing the capacitor size would eliminate the explosion hazard, but would not prevent failures.

A lamp failure was intentionally triggered to further explore the failure mechanisms. In this exercise an

electrodeless discharge was maintained at a constant power level (2.5 KW) while the pressure in the lamp was reduced until failure occured. The following data were recorded:

Applied Power (Watts)	Pressure (psia)	Total Power Radiated (Watts)	Net Efficiency (%)	Luminous Flux (Lumens)	Luminous Efficacy (Lumens/ watt)
2503	220	2065	82.5	91,207	36.44
2503	200	2051	81.9	91,552	36.58
2503	180	2010	80.3	89,828	35.89
2489	160	2010	80.7	89,828	36.09
2523	160	2037	80.7	91,897	36.42
2523	140	1983	78.6	87,414	34.65
2523	100	1845	73.1	85,172	33.76
2494	75	1721	69.0	82,241	32.98
2481	60	1624	65.5	78,966	31.83
2519	40	1432	56.8	69,655	27.65
~2500	25 - failure				

When the failure occurred, the lamp remained intact except at the actual failure point, which extruded several millimeters from the lamp prior to rupturing. A photograph of this lamp appears in Figure 9. The internal pressure at the time of failure was sufficient to deform the lamp, but the quantity of ionized xenon that escaped was inadequate to short the plate filter capacitor to ground.

The lamp shown in Figure 9 is typical of every failed lamp recovered to date. The failure mechanism is believed to be an unbalanced thermal stress somewhere on the lamp's surface caused by some combination of the following:

(a) contact of discharge and wall
(b) excessive internal conductive heat transport
(c) inadequate cooling of lamp surface.

Internal conductive heat transport can usually be reduced by raising the lamp pressure. This causes the discharge to constrict farther from the wall, thereby lowering the radial heat flux at the wall. Appropriate changes in the induction field magnitude and frequency will also enhance discharge constriction and reduce the conductive load on the lamp.

4.2 METAL-VAPOR DISCHARGE STUDIES

The principal goal of the present study is to obtain observational data describing the performance of the xenon

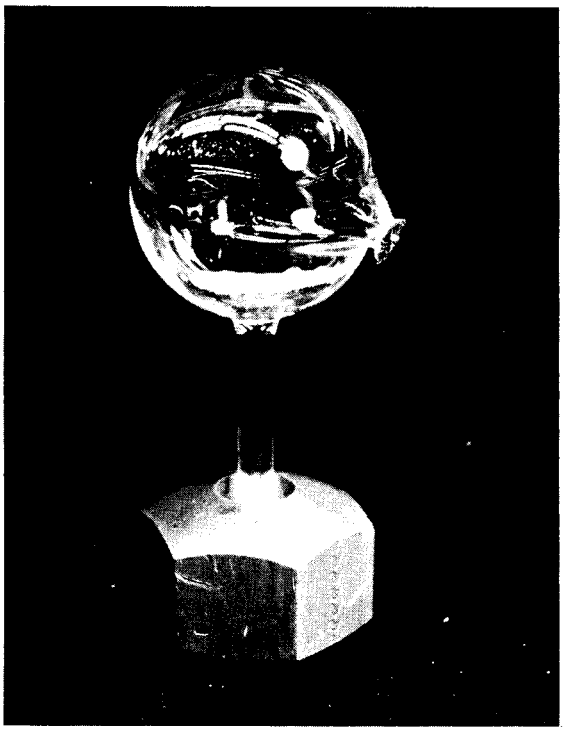

Figure 9: Photograph of ruptured lamp, illustrating typical failure mechanism.

electrodeless arc lamp. However, there are many reasons for an extension of the basic program into the area of metallic-vapor discharges. From the chemical standpoint alone, the electrodeless arc is a considerably more appealing concept for alkali vapor discharges than are conventional sources, and many applications are now available for alkali vapor sources which would be well satisfied by an appropriate electrodeless arc. Likewise, the high pressure mercury discharge is a popular large area illumination source. Moreover, relative to xenon, metallic-vapor illuminants are generally inexpensive.

The transition from a gaseous discharge technology to a metallic-vapor discharge technology is not as straightforward as one might desire. Metallic-vapor lamps are necessarily sealed-off, and reliable discharge ignition in sealed-off electrodeless lamps was a significant problem. Also, given a particular lamp-volume, optimization of discharge performance depends not just on the quantity of vaporizable material present in the lamp and on the operating power level, but on the coupling between these parameters, as well as on the magnitude and frequency of the induction field. Also, metal-vapor lamps have strict cooling requirements compared to gaseous discharge lamps because the operating pressure of the vapor discharge depends on rate-processes which are determined in part by boundary-value (i.e., envelope) temperatures. In general, the metallic-vapor electrodeless discharge lamp must operate at a considerably higher temperature than does its xenon counterpart.

Thus, on the one hand, the advantages of a metallic-vapor electrodeless lamp are both obvious and considerable. On the other hand, several technical problems are recognized immediately, and more probably exist. Also, while successful operation of low-pressure electrodeless discharges in metallic-vapors has been reported, no report of an electrodeless arc in a high-pressure metallic-vapor is known to exist. At the start of this program, it did not appear that even the feasibility of a high-pressure metal-vapor electrodeless arc lamp had been established.

A basic experimental survey of the properties of electrodeless arcs in high-pressure metallic-vapor was conducted to determine the practical feasibility of the concept. Apparatus was designed and constructed for the containment of a cesium vapor electrodeless arc, and techniques were developed to enable the ignition of an electrodeless arc in mercury vapor in a sealed-off, high-pressure spherical quartz lamp.

The study of discharges in cesium vapor was halted by the accidental breakage of the sapphire envelope of the alkali-vapor discharge lamp. The study was continued using the mercury lamps with little loss in continuity, and no loss to the goal of feasibility determination for metal-vapor electrodeless arc lamps.

The techniques developed thus far for the manufacture, sealing and starting of high-pressure mercury lamps are beyond the scope of this report. The key problem in their use appears to be in the maintenance of a sufficiently high internal pressure during operation.

The vapor lamp has one characteristic in common with its gaseous counterpart. If its pressure is inadequate the discharge will be of a sufficiently large size to contact the wall. As discussed in Section 4.1.5, contact of the discharge with the envelope wall promotes lamp failure. As might be expected, the violence of the lamp's failure depends mainly on the power level at which the lamp is operating at the time of failure. Since vapor-lamp pressure is relatively low just after starting, the most common cause of failure of the electrodeless vapor-lamp is the rapid application of excessive power during ignition. All vapor-lamp failures that have been observed to date occurred during starting. One would expect similar behavior to characterize alkali-metal discharges in sapphire envelopes.

The spectral composition of the high-pressure mercury electrodeless arc is almost completely line radiation, although a modest continuum exists between about one and two microns. Mercury spectral and Lite-Mike data were not reduced for purposes of this study and therefore are not discussed at greater length here.

An extensive survey of the illumination produced by the mercury vapor discharge was made because such measurements can be meaningfully interpreted without substantial data processing or reduction. A polar viewing angle of 30° was chosen for convenience.

The five mercury-vapor sources which are discussed were developed from a series of experimental lamps in a systematic effort to obtain predictable performance in a sealed-off lamp. Mercury content and backfill gas pressure were selected to enable rapid lamp warm-up, and to demonstrate certain important operating trends believed common to all electrodeless arc high-pressure metal-vapor lamps.

Observed values of luminous flux are presented in Table VI for each lamp at applied power levels between one and two kilowatts, at a constant frequency of 25 Mc.

Within the limitations of visual observations of the projected image of the discharges, all the mercury present in lamps #1 and #2 was in the vapor or plasma state. Condensed mercury was observed in each of the other lamps during operation.

The discharge in lamp #2 was constricted farther from the wall at a given power than was the discharge in lamp #1, suggesting that the operating pressure of lamp #2 was higher than that of lamp #1. This is consistent with the fact that more mercury is known to be present in lamp #2 than in lamp #1. Lamp envelope temperature data were not taken, however, so the actual operating pressure of either lamp cannot be estimated.

The discharges in lamps #3, #4, #5 were considerably more constricted than the preceding discharges. Mercury could be observed to condense on the upper lamp surface in the vicinity of the stagnation point of the flow of forced-air used for lamp cooling, indicating that excessive cooling existed for these lamps. These discharges presented relatively high impedances to the radiofrequency generator, as indicated by ratios of plate voltage to plate current (~plate impedance) which were observed to increase (at constant dissipation) with the mercury content of the individual lamps. When considered along with the enhanced discharge constriction observed in these lamps, the high impedances these discharges present to the generator suggest that their characteristically low lumen output is a consequence of poor coupling between the induction coil and the discharges. The latter discharges have diameters on the order of 1 cm, and the coil diameter is on the order of five cm, hence the coupling, which is proportional to the area ratio, is very poor. More efficient coupling, and presumably more efficient radiation production, would accompany the use of a smaller diameter coil for the mercury discharge.

TABLE VI

SUMMARY OF HIGH-PRESSURE MERCURY LAMP OBSERVATIONS

Lamp #	Hg fill (gm)	Plate Power (KW)	E (lumens/ft^2)	Luminous Flux (Lumens)	Luminous Efficacy (Lumens/Watt)
1	0.07	0.872	180	2.615×10^4	30.00
1	0.07	1.22	385	5.594×10^4	45.85
1	0.07	1.61	590	8.573×10^4	48.71
1	0.07	1.76	640	9.3×10^4	52.84
1	0.07	2.00	705	10.24×10^4	51.22
2	0.18	1.34	505	7.338×10^4	54.80
2	0.18	1.54	560	8.14×10^4	52.84
2	0.18	1.71	660	9.59×10^4	56.08
2	0.18	2.00	730	10.61×10^4	53.03
2	0.18	1.45	530	7.70×10^4	53.10
3	0.20	0.89	185	2.69×10^4	30.20
3	0.20	1.25	405	5.88×10^4	47.08
3	0.20	1.51	490	7.12×10^4	47.15
3	0.20	1.60	530	7.7×10^4	48.13
3	0.20	1.88	570	8.28×10^4	44.05
4	0.36	1.25	410	5.96×10^4	47.66
4	0.36	1.46	440	6.39×10^4	43.79
4	0.36	1.28	340	4.94×10^4	38.60
4	0.36	1.71	390	5.67×10^4	33.14
4	0.36	1.00	315	4.58×10^4	45.80
4	0.36	1.39	435	6.32×10^4	45.47
4	0.36	1.69	480	6.97×10^4	41.27
4	0.36	2.07	530	7.7×10^4	37.20
5	0.72	1.085	350	5.09×10^4	46.87
5	0.72	1.22	385	5.59×10^4	45.85
5	0.72	1.39	390	5.67×10^4	40.77
5	0.72	1.70	390	5.67×10^4	33.33

SECTION 5

CONCLUSIONS AND RECOMMENDATIONS

5.1 CONCLUSIONS

The xenon electrodeless arc lamp has been found to be an exceptionally efficient source of optical radiation when its operating point has been chosen to minimize conductive heat transfer from the discharge to the wall of its envelope, and "clean" rf techniques have been employed in the design and layout of its high-frequency circuitry.

The operational trends of this lamp's performance observed during the present study are just those predicted[3,4,9] by theory. Thus, within the parametric limits of the present study, power conversion into optical radiation by the electrodeless arc lamp increases with increasing discharge pressure and operating power level, and with decreasing induction field frequency.

Circuit techniques were found to be of key importance in the determination of electrodeless arc lamp performance at every operating point observed during this effort. High radiation efficiency was found to be predicated on high electronic efficiency. Thus, the combined effects of coupling between the induction coil and the discharge, the potential distribution in and around active circuit elements, and the nature of the conductors' surfaces contribute heavily to the determination of the performance of an electrodeless arc lamp.

The highest radiation production efficiency observed in a xenon lamp during this study (i.e., where the observation includes complete irradiance data) was 76.8% (Run A-2). This value corresponds to a case in which 91.5% of the radiofrequency power reappeared in the spectral band ($0.37\mu < \lambda < 1.8\mu$). The luminous efficacy associated with this lamp was 38.8 lumens per watt of DC input power. Observed trends leading toward higher operational efficiency suggest that even these figures can be improved

by increasing the coupling between the discharge and the induction coil and/or by lowering the induction field frequency.

Similar improvements in all observed data are expected to result from these or equivalent optimization techniques which can be employed at each operating point established in this study. Such techniques include optimization of discharge pressure, frequency, and coupling, and are supplemented by a high Q circuit design incorporating well-plated inductive elements in a minimum capacitance configuration.

Spectral irradiance distributions observed in this study indicate that, at the operating points observed, the effective "temperature" of the electrodeless arc lamp is considerably lower than that of the compact-arc lamp. A very crude estimate of the characteristic "temperature" of a radiant source can be found[9] from $\lambda T \approx 3625\mu°K$, where λ is the wavelength at which a source at "temperature" T produces radiation most efficiently, for a fixed value of flux radiated by the source. Assuming that λ is representative of the continuum peak of either a compact-arc or an electrodeless arc source, the spectra of these sources indicate that, within a few hundred degrees,

$$T\ (\text{compact-arc}) \approx 7250°K, \text{ and}$$
$$T\ (\text{electrodeless arc}) \approx 6050°K,$$

where λ (compact-arc) $\approx 0.5\mu$ has been estimated from data contained in lamp-manufactures' literature, and λ (electrodeless arc) $\approx 0.6\mu$ is estimated from the irradiance curves presented in Appendix C.

Since a "cool" discharge is a less efficient surface radiator than a "hot" discharge, the electrodeless arc's observed high efficiency is a consequence of its relatively large size, while its "temperature" is reflected by its relatively low surface brightness. The estimated xenon electrodeless arc "temperature" appears to be ideally intermediate for multiple applications involving visible and near IR-illumination.

Narrow-beam projection applications of the electrodeless arc lamp at one and 2.5 KW are feasible, and a measurable enhancement of beam uniformity should accompany coaxial lamp mounting due to the off-axis temperature profile of the electrodeless arc discharge. The xenon sources studied

herein also are well-suited to area illumination, where full benefit can be derived from their high efficiency, especially in the covert mode.

Successful operation, hence feasibility of a high-pressure mercury vapor electrodeless arc lamp was demonstrated during this study. In general, operation and performance of this device is complicated by the dependence of the discharge pressure on the operating power level, and particular care is required during the initial fill and sealing of the mercury vapor lamp, and in the establishment of its operating point. In all other respects, operation and performance of the mercury vapor electrodeless arc lamps appear to be qualitatively equivalent to the operation and performance of the gaseous electrodeless arc lamp.

With the single exception of the recognized unsuitability of a quartz envelope, an alkali vapor electrodeless arc lamp would present technical and developmental problems that are identical to those presented by the mercury vapor electrodeless arc lamp, which were solved during its development. Electrodeless arc lamps employing any of the alkali metal vapors therefore are considered to be entirely feasible at the present time.

A dynamic high-pressure plasma instability was observed at power levels above 2.5 KW. This instability was always accompanied by a significant decrease in radiation production efficiency, and since no lamp failures occurred during unstable discharge operation conductive mechanisms are not believed to participate to any significant extent. The instability therefore is believed to be purely convective in nature.

All lamp failures observed thus far are believed to have a common cause. All available evidence indicates that during failure the quartz lamp softens, extrudes, and ruptures in the same fashion every time. Techniques which prevent lamp-softening also appear to prevent lamp-failure; thus, improved wall cooling, increased discharge pressure, or any parameter variation which enhances wall-constriction are all effective devices for the prevention of lamp failure.

Several unique aspects of the electrodeless arc source have become apparent, but have yet not been discussed. Both the lamp-system and the lamp itself are high-voltage, low current devices (i.e., compared to the compact-arc lamp and its systems which are obviously low-voltage, high-current devices). In general, systems of the former class require more care in circuit layout and insulation than do the latter, but this

is offset by the fact that smaller buss lines and circuit elements are required in low-current systems. In practice, high-voltage low-current systems usually are smaller and less massive than are low-voltage, high-current systems. This is especially true in the case of radiofrequency systems, where almost all of the current carried by conductors is on the conductors' surfaces. The combination of radiofrequencies with high-voltage, low-current operation in an electrodeless lamp points the way toward future system volume-per-kilowatt ratios considerably smaller than the corresponding ratios for conventional illumination systems. One also would expect the per-watt cooling requirement to be significantly smaller in the case of the electrodeless arc system because of its higher efficiency.

5.2 RECOMMENDATIONS

It would appear to be prudent to further explore the trends toward lower frequency electrodeless arc lamp operation because this appears to be the obvious route to high-power performance of electrodeless arc lamps. If the observed discharge size versus power versus frequency trend continues, a ten-kilowatt electrodeless arc source will not be appreciably larger than those observed in the present study. Clearly, narrow-beam projection systems employing the electrodeless arc lamp would be exceptionally competitive at that level if the observed operating efficiency is retained.

The main technical problem recognized at the present time is the high-pressure instability which has limited the operational power level of the electrodeless arc lamp to 2.5 KW. The magnitude of this phenomenon is not known with certainty, however, the evidence to date has shown that the use of sealed-off lamps may eliminate this instability.

The relationships existing between apparent discharge rotation and the high-pressure instability should be explored experimentally. High-speed motion pictures of unstable discharges would be very helpful in identifying both these relationships and the characteristics of the instability itself. Corrective measures can be developed once the physics of the problem has been identified.

Circuit techniques have been found to be of significant importance in establishing the performance level of electrodeless arc lamps, but no systematic study of appropriate circuit techniques is known to have been performed. Clearly, it is highly desirable that the basic techniques reported herein be employed to specify the characteristics of an

optimized circuit in which the electrodeless arc is an active element, and to determine the electronic techniques required to achieve optimum performance with a practical circuit.

In context with the preceding recommendation, it should be emphasized that the electrodeless arc lamp is amenable to detailed study by means of an existing analysis of discharge energy balance. Only qualitative performance trends have been predicted so far, because the specific case of the xenon electrodeless arc has not been treated due to a lack of appropriate xenon transport and radiation coefficients. Recently, these data have become available, hence mathematical techniques now can be employed effectively to predict quantitatively the properties and operating trends of the xenon electrodeless arc lamp. It is suggested that these techniques be incorporated in all future developmental efforts to supplement the experimental techniques developed herein, in order to reduce the time required to develop future applications of the electrodeless arc lamp.

Finally, the technical feasibility of the high pressure metal vapor electrodeless arc lamp has been established, and successful operation of several such lamps has been demonstrated. It is recommended that the state of this art be extended to include the development of experimental alkali-metal vapor electrodeless arc lamps to the point at which the properties of such lamps can be measured, and a meaningful evaluation of such lamps can be made.

REFERENCES

(1) Cobine, J.D., Gaseous Conductors, Dover Publications New York (1958), Chapter 9.

(2) Reed, T.B., Jour. Appl. Phys. 32,821 (1961)

(3) Hollister, D.D., An Investigation of the High-Pressure Electrodeless Arc in Air I, AFFDL TR-68-160, AFSC Wright Patterson AFB, Ohio, February 1969.

(4) Hollister, D.D., An Investigation of the High-Pressure Electrodeless Arc in Air II, AFFDL TR-70-14, AFSC Wright Patterson AFB, Ohio, April 1970.

(5) Steenbeck, M.Z., Physik 33, 809 (1932).

(6) Peters, Th., Physik Verh. 6, 173 (1955).

(7) Peters, Th., Proc. Fifth International Conference On Ionization Phenomena in Gases, Ec. by H. Maecker, North-Holland Publishing Co., Amsterdam (1962), p 885.

(8) Smythe, W.R., Static and Dynamic Electricity, McGraw-Hill Book Co., New York, Ed. II (1950) p 53.

(9) Hollister, D.D., A Xenon Lamp With Two Less Electrodes Electro-Optical Systems Design 2, 26 (1971)

(10) Hudson, R.D., Infrared Systems Engineering, Wiley-Interscience, John Wiley and Sons, New York 1969 Chapter 2.

APPENDIX A

OPTICAL CALIBRATION

Calibration of the optical diagnostic instrumentation employed in this program is based on observations of the irradiance of a tungsten source with calibration traceable to the NBS, the positive identification of known lines in the spectra of electrodeless discharges in Xe, Kr, and Ar gases and Hg vapor, and the dispersed spectral positions of known monochromatic sources.

The monochromator, a venerable Perkin-Elmer Model 99, is typical of broad-band prism instruments in the extremes of instrumental dispersion which may appear in any spectrogram. Extensive wavelength-calibration of the spectral output of this instrument therefore is prerequisite to its use.

Various methods* for wavelength-calibration of multiple pass prism monochromators are available. The calibration technique employed herein was based on a positive identification of the dispersed positions of the red He-Ne laser line at λ6328 and of the sodium D lines at λ5890 and λ5896. Superposition of these spectral fiducial marks on the spectrogram of an electrodeless arc in mercury vapor extended the range of identified spectrum from λ3650 to λ17110. Additional positional measurements were obtained by means of spectrograms of electrodeless arcs in Xe, Kr, and Ar. The resulting wavelength-versus-position calibration is presented in Figure A-1.

The detector employed in this study is a conventional Perkin-Elmer thermocouple mounted within the monochromator. This sensor is inside an evacuated mount equipped with a KBr window. Its performance in the visible part of the spectrum is considerably inferior to its IR performance due to the nonlinear transmission of the KBr window, which is believed to have been contaminated with water vapor. The principal

---

*Ho, Shau-Yau, Appl. Optics 10, 1584 (1971); also Barns, R.B., et al, J. Appl. Phys., 16, 77 (1945)

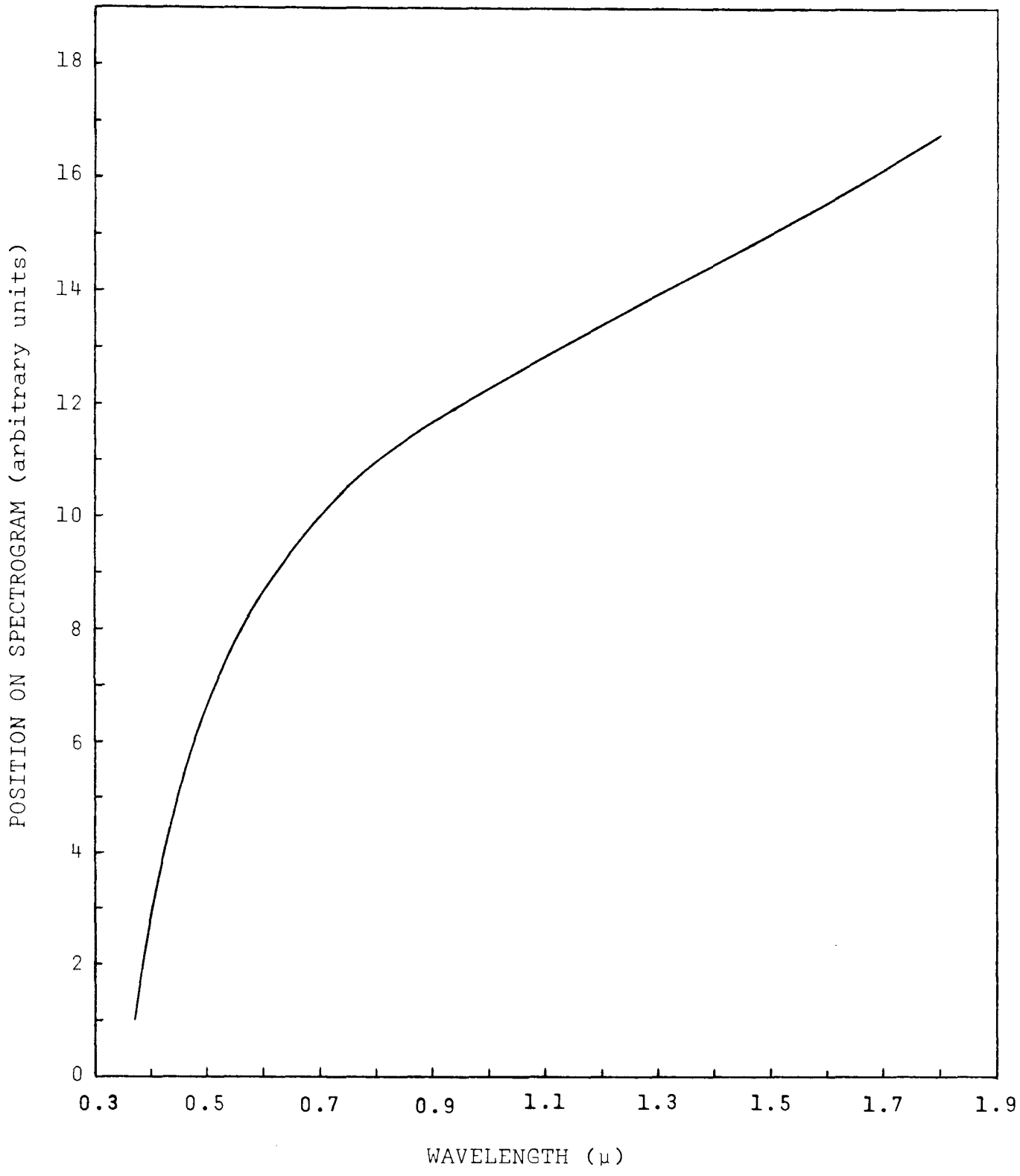

Figure A-1. Wavelengths versus position on spectrogram.

consequence of this nonlinearity is that the lower observational limit of the instrument with a fused quartz prism is in the neighborhood of 0.35μ.

Amplitude calibration was accomplished by observing a standard source with the monochromator and comparing the resulting spectrogram with the known input spectrum. The source employed is a General Electric Quartzline lamp which was calibrated by the Eppley Laboratory, and is traceable to the National Bureau of Standards through the reference standards QM-111, QM-112, and EPI-1373, which are maintained at the Eppley Laboratory. The spectral irradiance distribution of this source (EPI-1402) is shown in Figure A-2, normalized to unity for convenience in computations presented elsewhere. A reproduction of the calibration spectrogram is presented in Figure A-3.

The position on the spectrogram of a given wavelength is obtained from the horizontal calibration presented in Figure A-1 and any suitable reference wavelength. In the present exercise the reference was provided by the superposition of a dispersed xenon spectrum on the dispersed Quartzline lamp spectrogram, and supplemented by the identification of the prominent water absorption band heads located at 1.8μ, 1.4μ, 1.1μ, .94μ and .84μ. The geometry of the calibration exercise was identical to the geometry of the actual experiment to insure the inclusion of all path-length and absorption effects in the calibration.

In the absence of an appropriate slit-drive mechanism, a constant mechanical slit-width* of 200μ was used. This represents a practical compromise between spectral resolution and detector response. To minimize inertial and response effects associated with the recording instrument, the Littrow sweep speed was fixed at the lowest obtainable value (5.7 seconds of Littrow mirror rotational arc per temporal second). Also, only certain calibrated amplifier gain settings were used, and whenever gain was changed during a spectral observation, spectral regions common to both amplifier gain settings were recorded.

---

*The instrument employed in this experiment has its exit slit coupled to its entrance slit such that both slits have the same width at all times. Therefore, no distinction is made in this report between entrance and exit-slit-widths. The distinction between a constant mechanical slit-width and a variable spectral slit-width must be noted, however.

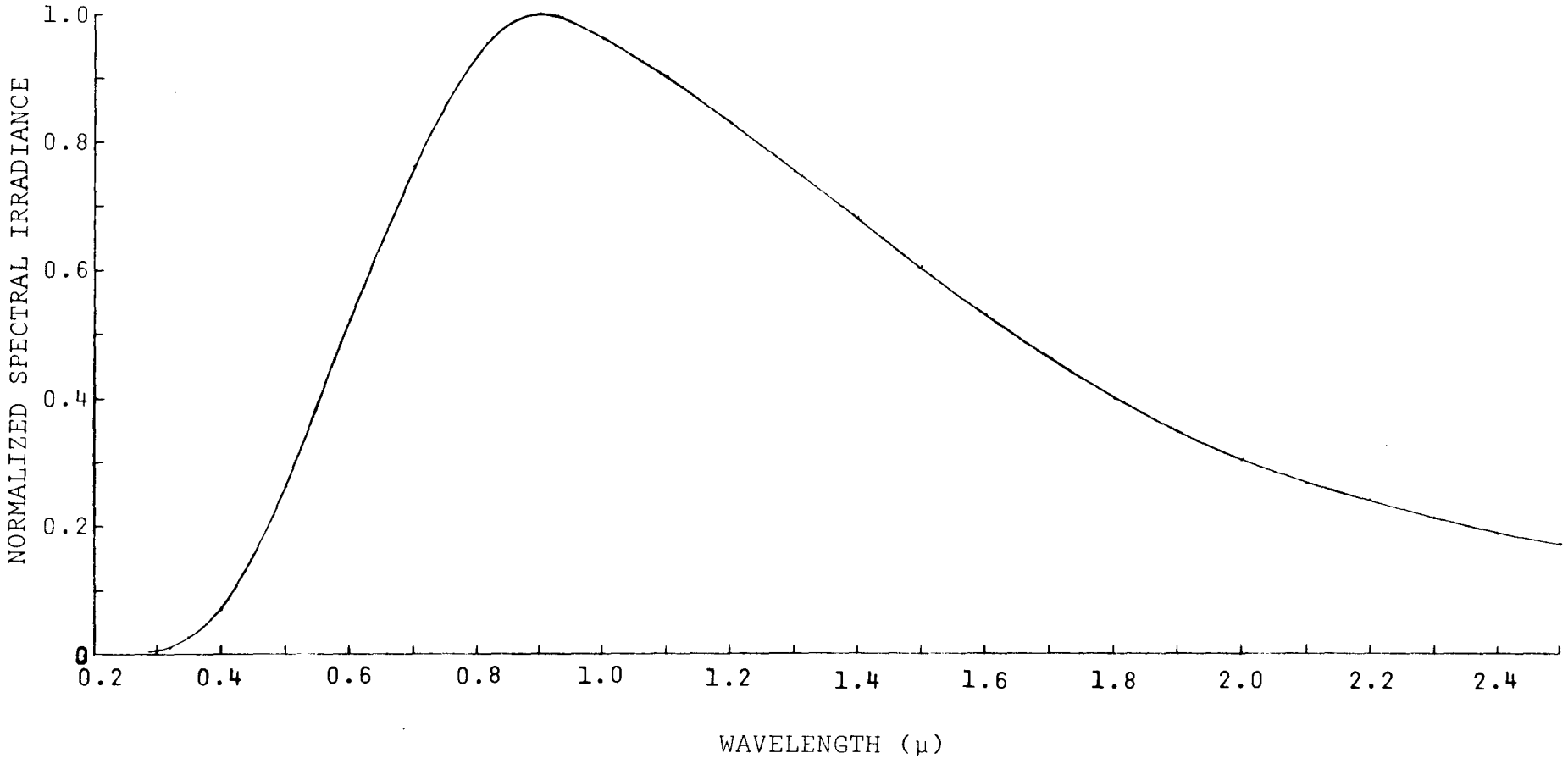

Figure A-2. Normalized spectral irradiance for Quartzline lamp (EPI-1402).

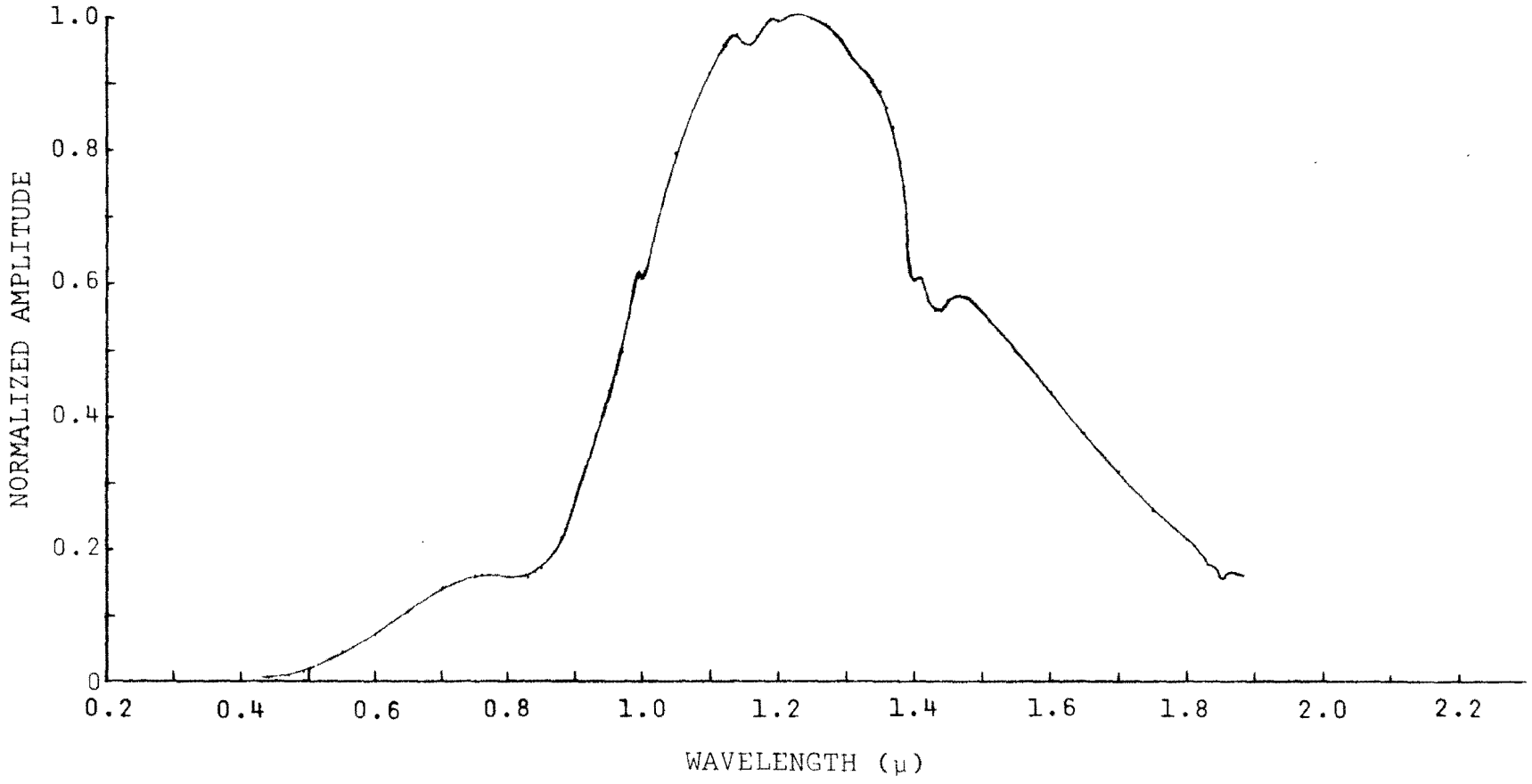

Figure A-3. Quartzline lamp calibration spectrogram.

An instrument transfer function was developed from the wavelength and normalized amplitude calibrations. This function relates an area-per-unit-wavelength interval of the observed spectrogram to the corresponding area-per-unit-wavelength interval of the normalized acutal spectral distribution, and includes the effects of a variable spectral slit-width, and those of water absorption integrated along the optical path. The transfer function, which is evaluated for the laboratory case of minimum Littrow drive speed and a 200μ slit, appears in Figure A-4. It is defined such that the normalized product of the area in a particular wavelength interval on the recorded (i.e., observed) spectrogram and the transfer function for that wavelength interval equals the corresponding area (irradiance) of the normalized input spectral distribution.

In Figure A-5 is presented the reduced Quartzline lamp observation, which has been normalized to unity and superimposed on the lamp's normalized spectral irradiance distribution. The assignment of a numerical value to the normalizing irradiance is provided by a supplementary measurement employing the silicon photodetector of an EG&G Lite-Mike.

The Lite-Mike was calibrated by direct measurement of the irradiance of the standard lamp. The irradiance distribution of this lamp is reproduced in Figure A-6 where its extrapolation to infinite wavelength is indicated (the Eppley Laboratory calibration extended only to 2.5μ).

To a very close approximation the normalized Quartzline lamp irradiance distribution is exponential in the region past its peak at 0.95μ. If the e-folding length of this curve is denoted by u, the amplitude h(x) at any abscissa x will very nearly be $h_o \exp(-x/u)$, where h_o is the peak amplitude. With a very small margin of error the total area A_t under the irradiance distribution is given by

$$A_t \approx A_0 + A_1 + h_o \int_{x=u}^{\infty} \exp(-x/u)dx$$

$$= A_0 + A_1 + uh_o/e \ ,$$

where A_0 is the area of the obviously non-exponential part of the distribution and A_1 is the area of that part of the distribution adjacent to A_0 which extends one e-folding length from 0.95μ. Throughout this calibration all areal integrations are referred to a common scale in which the peak has an amplitude arbitrarily chosen to be five inches.

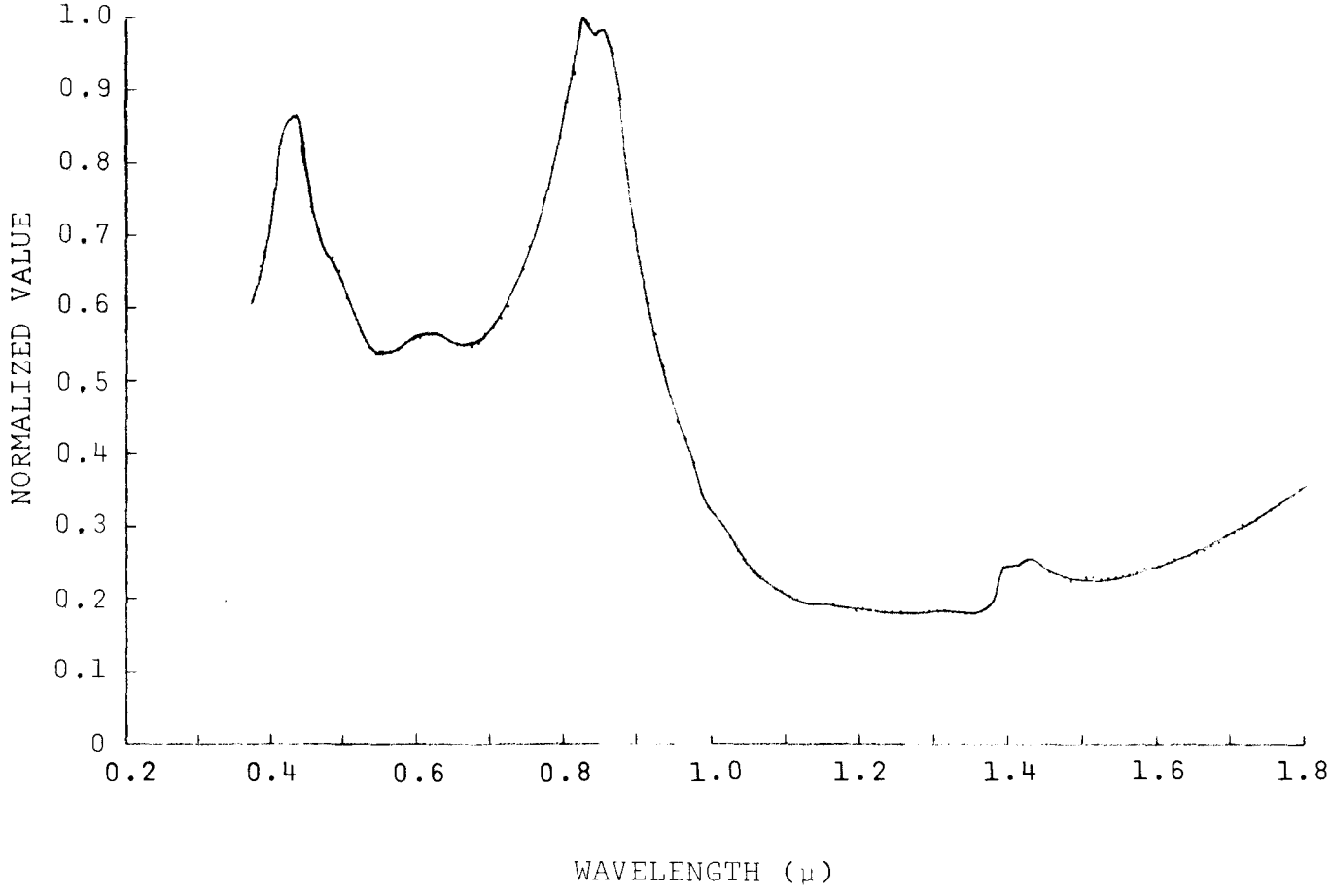

Figure A-4. Normalized instrument transfer function.

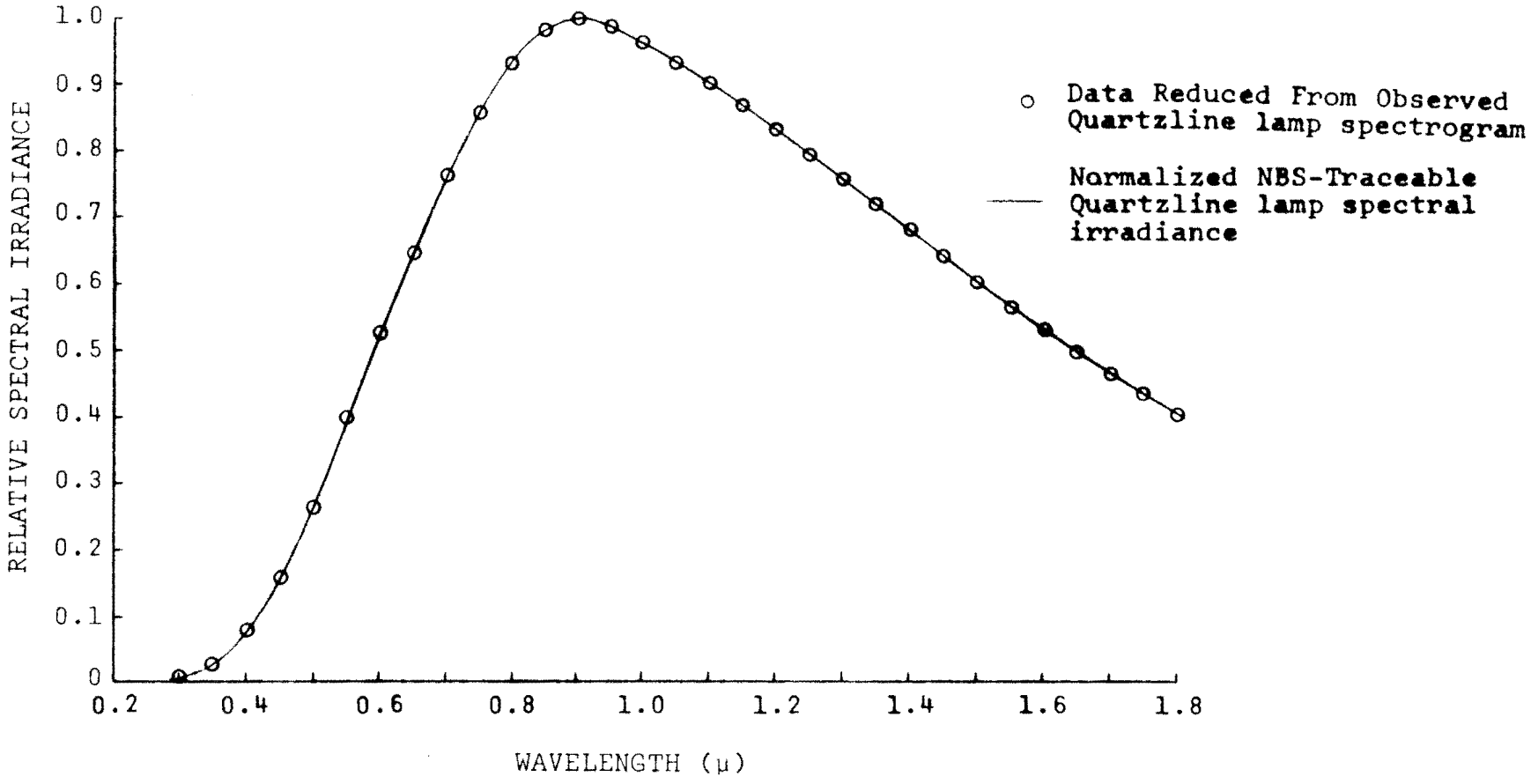

Figure A-5. Comparison of reduced calibration spectrogram with NBS-traceable data for the Quartzline lamp.

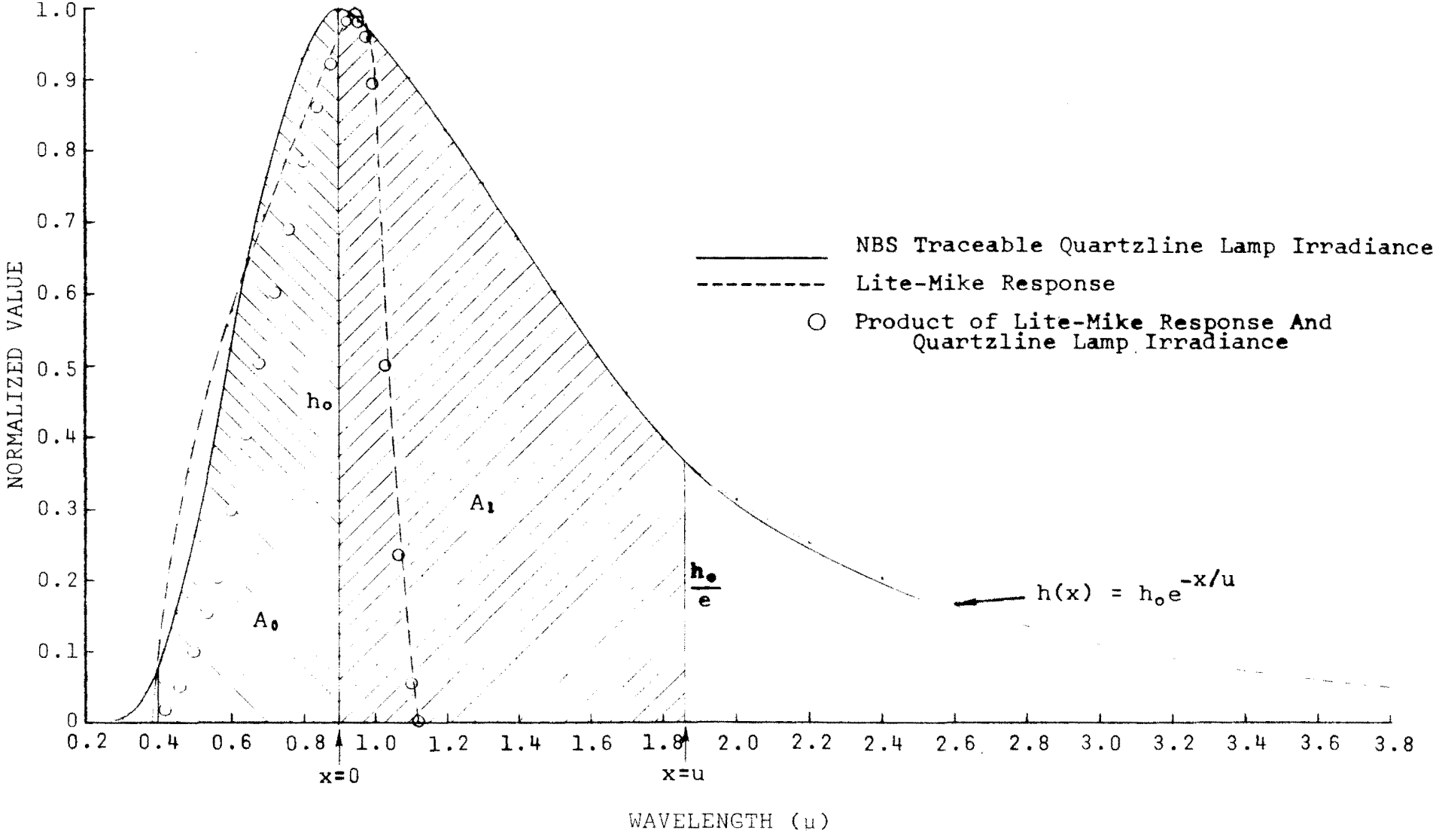

Figure A-6. NBS traceable Quartzline lamp spectral irradiance, Lite-Mike spectral response, and their product.

Likewise, the linear wavelength scale has been chosen so that one inch represents an interval of 200 nanometers. With this convention, the tabulated values of normal Quartzline lamp irradiance can be integrated numerically to give A_0 and A_1 directly in square inches. Conversion from square inches to absolute irradiance involves nothing more than multiplication of the area by the appropriate scale factor which is obtained from the tabulated lamp calibration data: 1 in^2 = 1.012 x $10^3 \mu W/cm^2$. Thus

$$\text{Irradiance} = \frac{\Delta \Phi}{\Delta A} \approx 1.012 \times 10^3 (A_0 + A_1 + uh_o/e) \mu W/cm^2,$$

where u = 4.8 inches is the e-folding distance on the conventional scale, which obtains at 1.86μ, and uh_o/e = 8.84 in^2. Values for A_0 and A_1 were respectively determined to be 7.63 in^2 and 16.65 in^2, yielding a total area of 33.12 in^2. Therefore, the net irradiance of the Quartzline lamp is 3.35 x $10^4 \mu W/cm^2$ at the calibration distance (50 cm) of the lamp.

For convenience in the following presentation the response of the Lite-Mike employed in this study was included in Figure A-6 as was the product of this function and the standard source spectral irradiance. Both the source and response curves have been normalized to unity.

The area under the normal spectral irradiance curve is divided into bands which are bounded by the wavelength limits of Lite-Mike response in order to specify the fraction of source irradiance to which this instrument is sensitive. It is customary to define such bands in terms of the wavelength values at which the instrument achieves 10% of its maximum response. These values, for the instrument employed in this study, are 0.4μ and 1.11μ.

Throughout the duration of the Lite-Mike calibration the source to detector distance was fixed at 98 cm. The current indicated by the Lite-Mike is proportional to the area under the product curve of Figure A-6. Taking account of the appropriate scale factors, this is formulated:

$$I = 2.634 \times 10^2 (\text{area}) \times K_o \text{ microamperes}, \qquad (1)$$

where K_o is a constant of proportionality unique to the particular sensor element employed in the instrument, I is the indicated current, and the area under the product curve is given in square inches (i.e., 9.004 in^2). K_o was evaluated from a single Lite-Mike reading: at the indicated

distance of 98 cm, I = 53μA, and K_o was found to be 2.234×10^{-2} μA/μW/cm^2. This value differs by 13.4% from the value given by the manufacturer of the instrument. The previous calibration was performed approximately fifteen months prior to the present calibration, and the change in the instrument constant's value is believed to be due to ordinary aging.

The response of the Lite-Mike instrument to the Quartzline lamp irradiance distribution was determined in terms of K_o, the area under the irradiance distribution curve, and the indicated current, since

$$\frac{\Delta \Phi}{\Delta A} \propto \frac{\text{area of distribution}}{K_o} I,$$

where the constant of proportionality is the reciprocal of the product area employed above. Thus:

$$\frac{\Delta \Phi}{\Delta A} = 1.647 \times 10^2 \; I \; \mu W/cm^2, \qquad (2)$$

where I is measured in microamperes. Substitution of I = 53μA yields the Quartzline lamp irradiance at a distance of 98 cm: $\Delta \Phi/\Delta A = 8.726 \times 10^3 \mu W/cm^2$. This figure compares with the irradiance derived from Eppley Laboratory data which was given previously to be $3.35 \times 10^4 \mu W/cm^2$ at a distance of 50 cm:

$$8.726 \times 10^3 \times (98/50)^2 = 3.35 \times 10^4 \mu W/cm^2.$$

The instrument calibration procedure is applicable to the case in which a filter is used in conjunction with the Lite-Mike. The filter modifies the instrument response function with the main effect that a new instrumental calibration constant K_f must be determined for each filter employed.

If the net effective filter transmission is denoted by $F(\lambda)$ and the instrument response is denoted by $R(\lambda)$, the effective response of the instrument-filter combination is $R(\lambda)F(\lambda)$, and the combination pass-band is defined, as before, by the wavelength positions of the 10% response points.

Multiplication of the effective response at each wavelength interval by the area under the source irradiance distribution, and integration of this product over the pass-band yields, as before, an area proportional to the current

indicated by the Lite-Mike. This relation was presented in Eq (1), which can be solved for the new instrument constant K_f in terms of the area determined above, the current indicated by the instrument, and the appropriate scale-factors. The source irradiance is then determined by the following expression:

$$\left.\frac{\Delta \Phi}{\Delta A}\right|_{\Delta\lambda} = \frac{\text{(Area of source irradiance in } \Delta\lambda)}{\text{(Product area in } \Delta\lambda)} \cdot \frac{I}{K_f} \frac{\mu W}{cm^2}, \quad (3)$$

where the two areas and the new instrument constant are simple numerics. The transmission curves of two filters used in this study are presented in Figure A-7.

This calibration yielded the following instrument constants:

Filter		Instrument Constant
None	K_0	$= 2.234 \times 10^{2} \mu A/\mu W/cm^2$
RG780	K_{780}	$= 2.857 \times 10^{2} \mu A/\mu W/cm^2$
RGN9	K_{N9}	$= 2.482 \times 10^{2} \mu A/\mu W/cm^2$

Lite-Mike current readings yield directly the Quartzline source irradiance as follows:

Band	Filter	$\Delta \Phi/\Delta A$
0.4μ - 1.11μ	None	0.627×10^2 I $\mu W/cm^2$
0.37μ - ∞	None	1.647×10^2 I $\mu W/cm^2$
0.78μ - 1.10μ	RG780	0.571×10^2 I $\mu W/cm^2$
0.73μ - 1.09μ	RGN9	0.739×10^2 I $\mu W/cm^2$

The instrument constants presented above are valid for the particular instrument and filters employed in the present study, and are independent of the spectral distribution of source irradiance. The numerical values given above relating Quartzline lamp irradiance to Lite-Mike current apply only to the Quartzline lamp herein employed. Equivalent relationships were necessarily derived for each xenon spectral irradiance distribution observed during the main part of the present study.

As a final check on the Lite-Mike calibration technique, the net radiation produced by the standard lamp was estimated by measuring the polar irradiance distribution of this lamp with the Lite-Mike, and integrating the result over 4π steradians at the radius of observation.

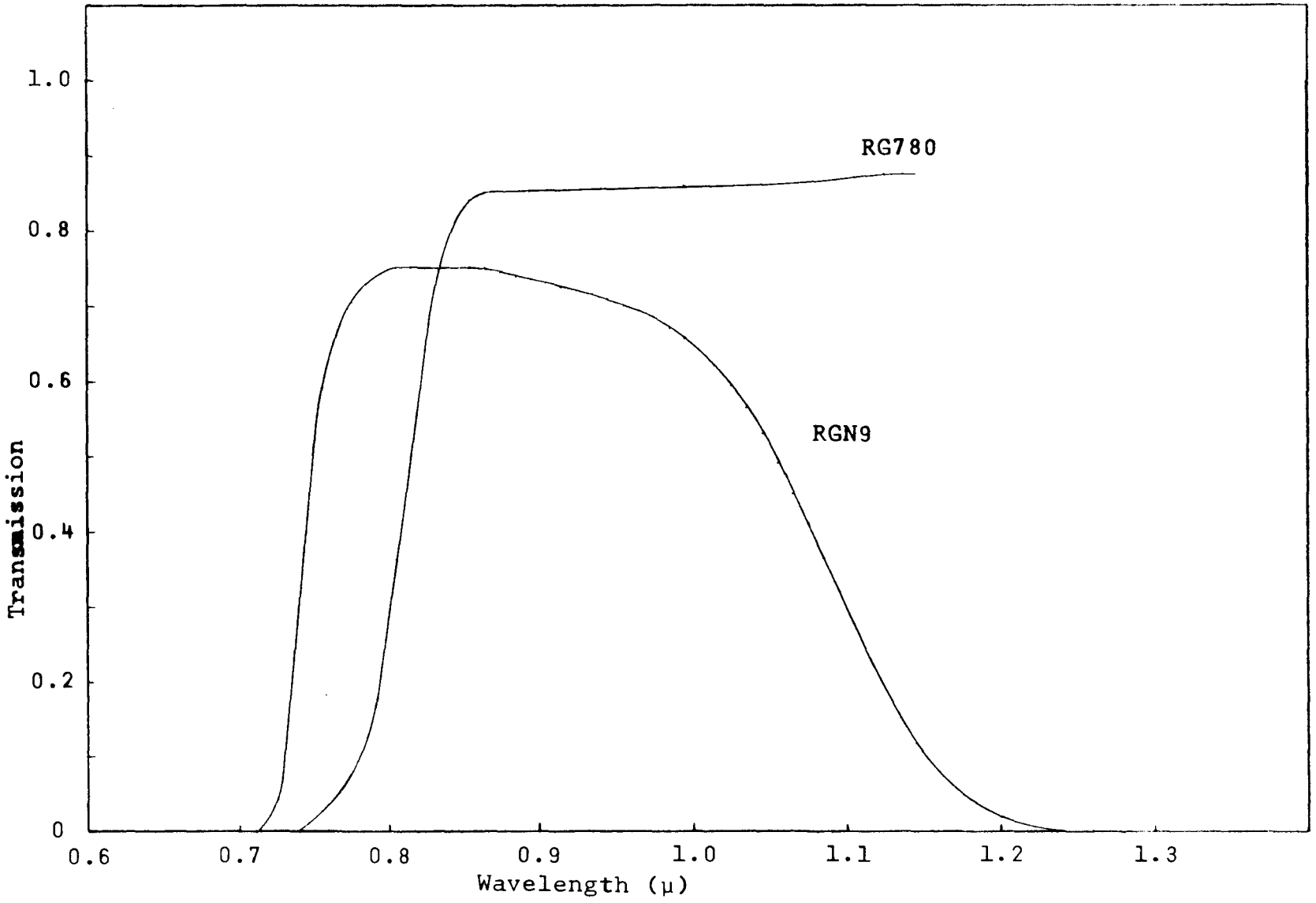

Figure A-7. Transmission of RGN9 and RG780 filters.

Observations were made by locating the Lite-Mike detector head in a succession of prepared positions on a circular jig attached to an optical bench. The apparatus was such that the Quartzline lamp was viewed from the constant distance of 98 cm at 5° intervals. The observed distribution was corrected for stray pickup, which was measured by shielding that part of the lamp being directly viewed and subtracting the indicated Lite-Mike current from the original values at each observation station. This distribution compares within a few percent with the distribution obtained by mounting the Lite-Mike detector head on the optical bench and rotating the Quartzline lamp through 90°. Stray radiation can be eliminated almost entirely from the latter measurement, but non-vertical mounting is not recommended for the standard lamp. Lite-Mike readings of the polar distribution of the Quartzline lamp irradiance are presented in Figure A-8.

The total radiant flux was found from

$$\Phi = 1.647 \times 10^2 \int (\Delta \Phi / \Delta A) r^2 \sin\theta d\theta d\phi \approx 913 \text{ watts},$$

where θ and Φ respectively are the polar and azimuthal coordinates.

The potential across the lamp at the time of this measurement was 116 volts and the current was 7.9 amperes, indicating an input power of 916 watts. One would expect to recover only about 90% of the input power as radiation, however, due to internal lamp and bulb losses. The lamp input current measurement is accurate within 2%, however the lamp voltage and Lite-Mike measurements are individually accurate to only 5% so the margin of error for the measurement of the polar distribution is 12%.

That fraction of Quartzline lamp irradiance which falls under the visibility curve was determined by multiplying the coefficients of the photopic luminosity function at each wavelength interval by the area under the Quartzline lamp irradiance distribution for that wavelength interval, and integrating the result.

The numerical value thus obtained was converted to photometric units at the reference position of the calibration (i.e., lumens/ft^2 at 98 cm) to give 186 lumens/ft^2. This figure represents the 90° value in the polar distribution which was measured previously. Normalization of this distribution to unity, multiplication through by 186 lumens/ft^2 and integration over 4π steradians yields the

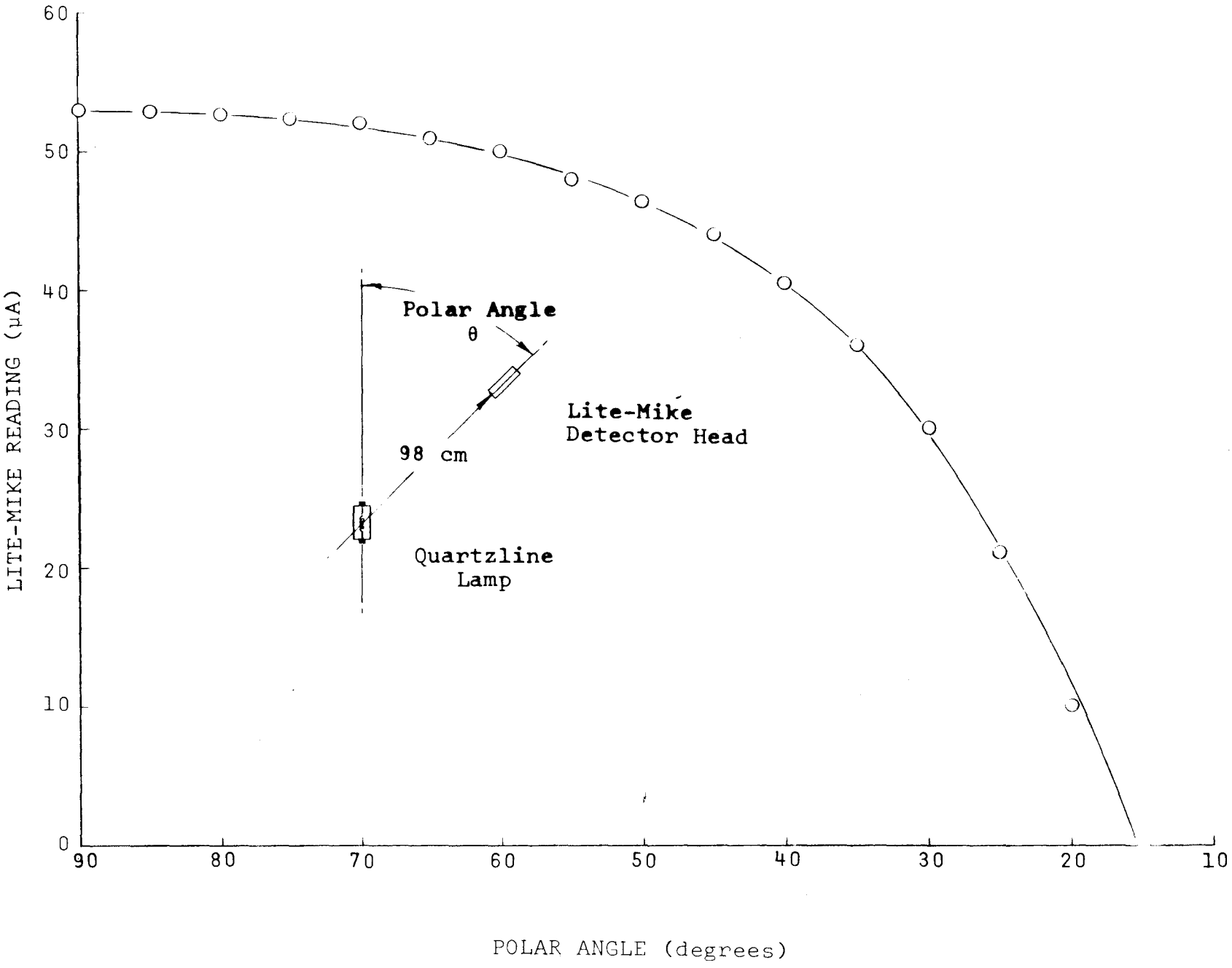

Figure A-8. Polar distribution of Quartzline lamp irradiance.

total luminous flux of the quartzline lamp: 20,880 lumens. This figure compares with the 20,400 mean lumens and the 21,000 approximate initial lumens usually cited* for this lamp.

---

*Kaufman, J.E., Editor, IES Lighting Handbook, Published by the Illuminating Engineering Society, New York, Ed IV. 1968. Table 8-48

APPENDIX B

POLAR RADIATION DISTRIBUTION STUDIES

Irradiance and source-candlepower data obtained during this program were derived in part from images of the top-view of the discharge. This view is characterized by an off-axis peak in the brightness distribution, which follows directly from the structure of the discharge current density distribution. In effect, the top-view of this discharge has a hole in its center which causes the irradiance measured from the top to differ appreciably from that measured from an off-axis position.

During the initial design of the experimental system an engineering trade-off was made based on the desirability of adequate lamp cooling during high-power operation of the lamp, and a capability to view the discharge from other than the vertical direction. It was decided that, for the purposes of the present experiment it was significantly more important to assure adequate lamp cooling than to measure spatial radiation distributions.

Upon completion of the experimental test-matrix it became possible to modify the experiment sufficiently to allow an approximate determination of the polar distribution of discharge radiation. Such modifications included removal of the lamp cooling duct and vertical mirror, the coating of the inside surface of the discharge radiation shield with flat balck paint, the covering of the electronic components with dull black felt, removal of the aluminum shielding cover plate to allow visual access to the discharge lamp, and the blackening of the induction coil by means of ultra-flat black enamel. A 90° circular arc was mounted atop the optical bench and clamped to the frame of the radiofrequency supply, to allow mounting of the Lite-Mike detector head at 5° intervals along the arc. The radius of this arc was such that the Lite-Mike sensor was 98.0 cm from the discharge center at any angular mounting position. With this configuration of the apparatus, the discharge could be viewed between polar angles 15°-45° without appreciable obscuration, but at smaller angles the

power supply framework blocked the radiation from the discharge, and at larger angles (through the horizontal) the lower half of the discharge was obscured by the induction coil. This assemblage is depicted schematically in Figure B-1.

Normalized polar distributions of Lite-Mike readings and illumination are presented in Figure B-2. These data also are tabulated in Table B-I. Except at small polar angles, no significant differences between the spatial distributions of irradiance and illumination have been observed; they are assumed to be identical, except at small polar angles.

The actual polar distribution of discharge radiation is believed to follow that presented out to about 50°. For larger polar angles partial shadowing of the lower portions of the semi-spherical discharge by both the induction coil and by the discharge itself could be observed visually. The decrease in detected radiation along the discharge polar axis was as expected. Beyond 40° to 50° the observed diminution of radiation is believed to have been caused by the coil itself.

With reference to Figure B-2, the distributions which fall off rapidly with increases of polar angle θ are seen to have the coil in the "normal" position relative to the lamp. The fall-off with θ was also observed to increase if the coil size is reduced. Alternately, normal sized coils which were lowered relative to the fixed lamp position yield polar radiation observations that are much flatter and extend to larger angles than do those of the former. In a physical sense one would expect the horizontal flux to be significantly greater than the flux observed from directly above because of the uniformity of the side-view of the discharge which is attributed to the relatively uniform plasma current distribution which exists in that plane. In any event, since at least one-half of the discharge was in shadow at polar angles greater than 60°, and since considerably more than one-half the maximum radiation was detected at polar angles greater than 60°, it appears that the diminution of observed flux with increasing polar angle was nothing more than a simple shadowing effect due to the proximity of the induction coil to the discharge.

For example, consider the geometry presented in Figure B-3 where a spherical discharge of diameter 2r is maintained within a cylindrical induction coil of diameter 2d and height h. To predict qualitatively the effects of shadowing

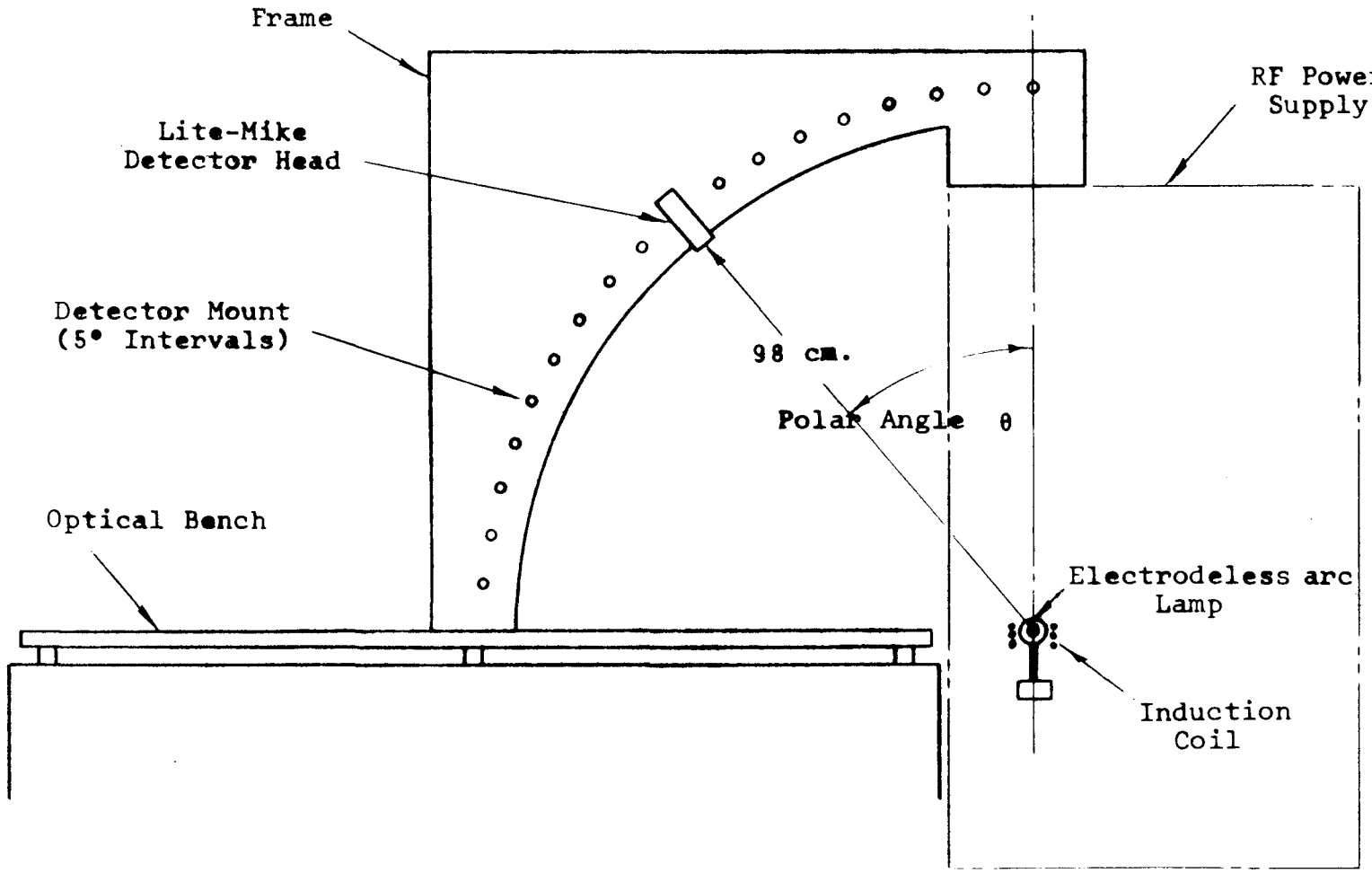

Figure B-1. Experimental layout for polar distribution measurements.

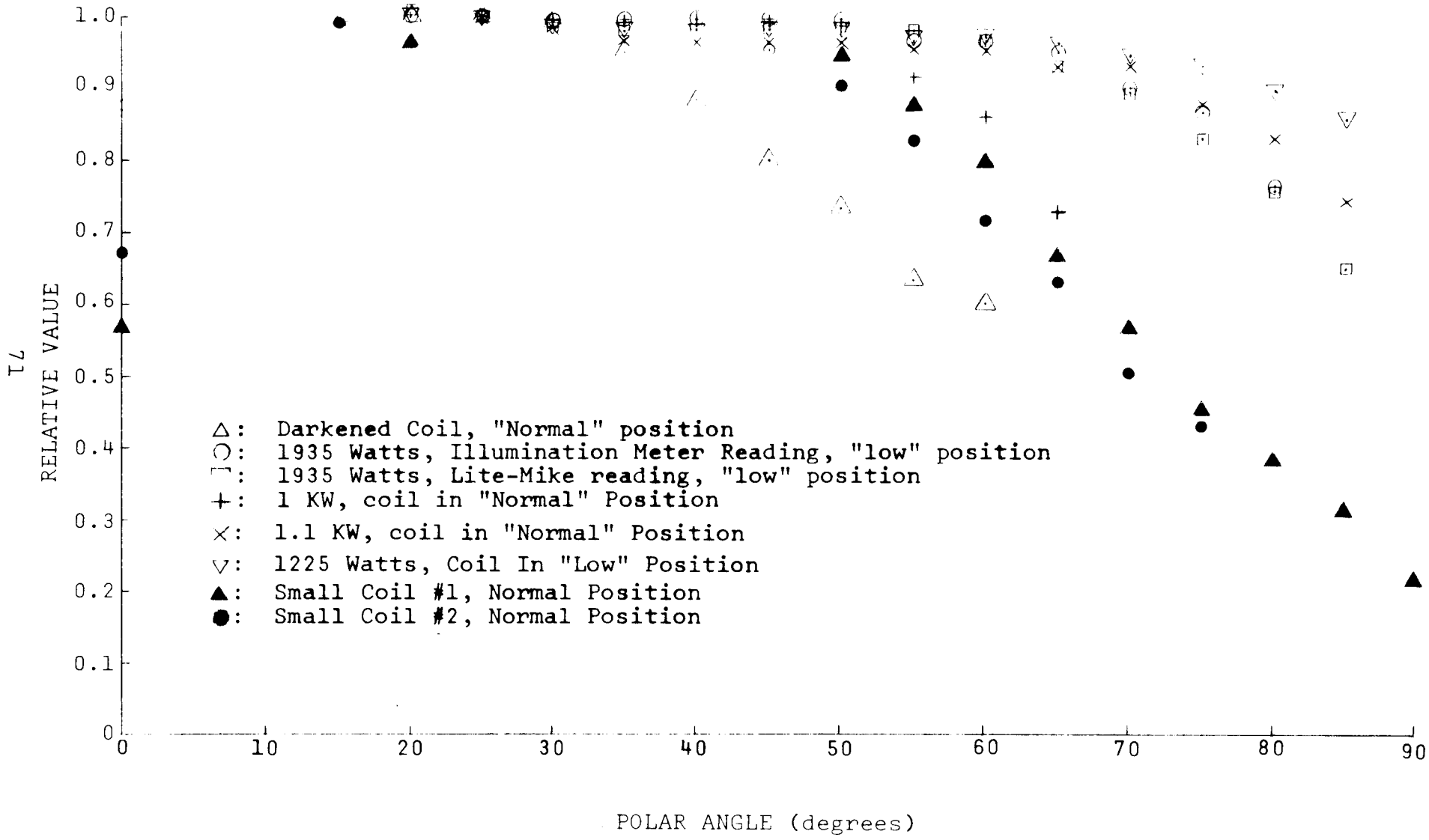

Figure B-2. Polar distributions for some electrodeless arc lamps.

TABLE B-I

ELECTRODELESS ARC LAMP POLAR DISTRIBUTION

Polar Angle	Darkened Coil	1935 Watts Ill Meter	1935 Watts Lite-Mike	1KW low	1.1 KW High	1225 Watts	Small Coil #2	Small Coil #1
90	-	-	-	-	-	-	-	.215
85	-	-	.648	-	.742	.859	-	.314
80	-	.764	.759	-	.83	.898	-	.382
75	-	.866	.828	-	.875	.93	.433	.450
70	-	.9	.897	-	.928	.945	.502	.567
65	-	.95	.931	.73	.928	.961	.630	.667
60	.6	.965	.97	.862	.955	.969	.718	.795
55	.634	.965	.98	.917	.955	.977	.827	.872
50	.734	.994	.986	.984	.965	.985	.905	.944
45	.8	.994	.98	.995	.965	.985	.955	.99
40	.884	.994	.98	.974	.965	.985	.985	.99
35	.95	.994	.980	.974	.965	.985	.994	1
30	.995	.994	.986	.995	.982	.99	1	.995
25	1.0	1	1	1	.99	1	.992	.99
20	1.0	1	1.03	1	1.0	1.02	.975	.962
15	1.0	-	-	-	-	-	.945	.163
10	-	-	-	-	-	-	-	-
5	-	-	-	-	-	-	-	-
0	.868	-	-	-	-	-	.673	.568

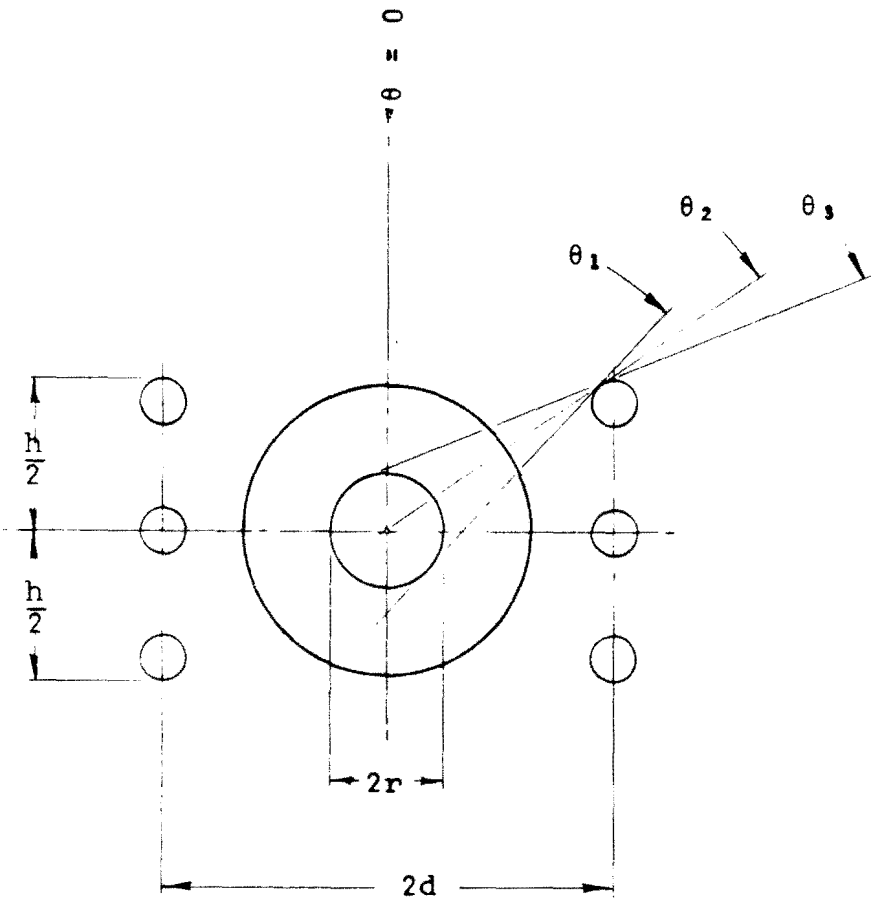

Discharge Diameter, 2r = 1.5 cm.
Induction Coil Diameter, 2d = 6 cm.
Induction Coil Height, h = 4 cm.

Figure B-3. Geometrical configuration of spherical discharge and induction coil.

in a polar radiation measurement one observes that the lower edge of the discharge becomes obscured at an angle θ_1, where $\theta_1 \approx \tan^{-1} d/(3h/4)$. One would predict diminution to be first detected at θ_1. Diminution would be complete (ignoring radiation from the discharge through the space between turns of the coil) at θ_3, where $\theta_3 \approx \tan^{-1} d/(h/4)$. An intermediate angle would be $\theta_2 = \tan^{-1} d/(h/2)$, where shadowing effects would be noticed, yet still developing.

In the present experiment a typical coil diameter was 6 cm, and its height was 4 cm. A typical xenon discharge had a radius of about 1.5 cm. Thus, in this simple model

$$\theta_1 = \tan^{-1} 3/3 = 45°,$$
$$\theta_2 = \tan^{-1} 3/2 = 56.6°,$$
$$\theta_3 = \tan^{-1} 3/1 = 71.5°;$$

and one would predict that a series of polar radiation measurements would yield the correct distribution for $\theta < \theta_1$ (i.e., out to 45°), and that obscuration of discharge radiation would increase as the tangent of the polar angle beyond θ_1, becoming maximum at θ_3 (i.e., 71.5°).

The trend predicted by this simple model is precisely that observed. The observed radiation distribution was low along the the polar axis as expected, increased significantly over a 20° polar angle, and then remained constant out to about 45°, at which angle the top of the induction coil began to obscure the bottom of the discharge. Beyond 45°, the observed polar radiation distribution fell off less rapidly than predicted, but this is because the induction coil only partially obscured the discharge (i.e., light escapes between the turns) at large polar angles.

Structural data near $\theta = 0°$ were obtained using the blackened induction coil and the Lite-Mike detector, where considerable effort was spent to eliminate stray light pickup. The central-axis irradiance $\Delta\Phi/\Delta A|_{\theta=0}$ as indicated by Lite-Mike readings, was approximately thirteen percent less than the reading $\Delta\Phi/\Delta A|_{\theta>20°}$ obtained at polar viewing angles greater than 20°. (i.e., $\Delta\Phi/\Delta A|_{\theta=0} = 0.868\ \Delta\Phi/\Delta A|_{\theta>20°}$). This is reproducible within the accuracy with which the Lite-Mike can be read.

Measurements employing the detector of an illumination meter yielded polar distributions nearly identical to those obtained from Lite-Mike observations, except in the vicinity of $\theta = 0$ where the indicated illuminance is considerably less than that expected on the basis of the polar distribution derived from Lite-Mike measurements. Qualitatively, this is

to be expected because the spectral response of the illumination detector is peaked for higher temperature radiation than is the Lite-Mike, and the top-view of the discharge clearly is a more efficient low temperature radiator (i.e., IR) than it is a high temperature source (i.e., visible) because of its structure. Quantitatively, the relative diminution of illumination at $\theta = 0$ can only be estimated within about 10% because of the spread in observed values at 0°. A nominal central value was obtained by averaging the normalized central value observations. Its value is 0.814. It is included here in the computation of source properties. It is used only for rough, but independent, checks on other calculations.

If no method existed to remove the shadowing effects of the induction coil it would not be meaningful to include this unrecoverable fraction of radiated power in engineering calculations of radiation produced by electrodeless arc discharges. Since methods have been demonstrated successfully which remove shadowing entirely (i.e., the combined inductor/reflector) it is meaningful to treat all the radiation produced by an electrodeless arc as recoverable.

The polar radiation distribution of the electrodeless arc lamp is given by the coefficients presented in Table B-II. The absolute accuracy of this distribution is not known with certainty, but the accumulated error throughout the polar radiation measurement is less than 15%.

Incorporation of this distribution into electrodeless arc calculations involving integrations over 4π steradians is accomplished by formation of the area element $r^2 \sin\theta d\theta d\Phi$, assuming azimuthal symmetry, and summing the coefficients $K(\theta)$ over their respective angles:

$$\int \xi(\theta) dA \approx 2\pi r^2 \Delta\theta \xi_o \sum_{\theta=0}^{\theta=\pi} K(\theta) \sin\theta,$$

where $\xi(\theta)$ is a dummy variable which has an off-axis value ($\theta > 20°$) equal to ξ_o, and r is the observation distance. The summation is evaluated in Table B-III.

TABLE B-II

COEFFICIENTS OF POLAR RADIATION DISTRIBUTION
OF ELECTRODELESS ARC LAMP

Polar Angle	Coefficient K(θ)
0°	0.868
5°	0.905
10°	0.935
15°	0.965
20°	0.980
25°-90°	1.000

TABLE B-III

ELECTRODELESS ARC LAMP POLAR DISTRIBUTION OF RADIATION

θ	K(θ)	sinθ	K(θ)sinθ
90°	1.0	1.0000	1.0000
85°	1.0	0.99619	0.99619
80°	1.0	0.98481	0.98481
75°	1.0	0.96593	0.96593
70°	1.0	0.93969	0.93969
65°	1.0	0.90631	9.90631
60°	1.0	0.86603	0.86603
55°	1.0	0.81915	0.81915
50°	1.0	0.76604	0.76604
45°	1.0	0.70711	0.70711
40°	1.0	0.64279	0.64279
35°	1.0	0.57358	0.57358
30°	1.0	0.5000	0.5000
25°	1.0	0.42262	0.42262
20°	0.980	0.34202	0.33518
15°	0.965	0.25882	0.24976
10°	0.935	0.17365	0.16236
5°	0.905	0.08716	0.07888
0°	0.868	0	0

Σ K(θ) sinθ = 11.91643

APPENDIX C

SPECTRAL RADIATION DISTRIBUTIONS

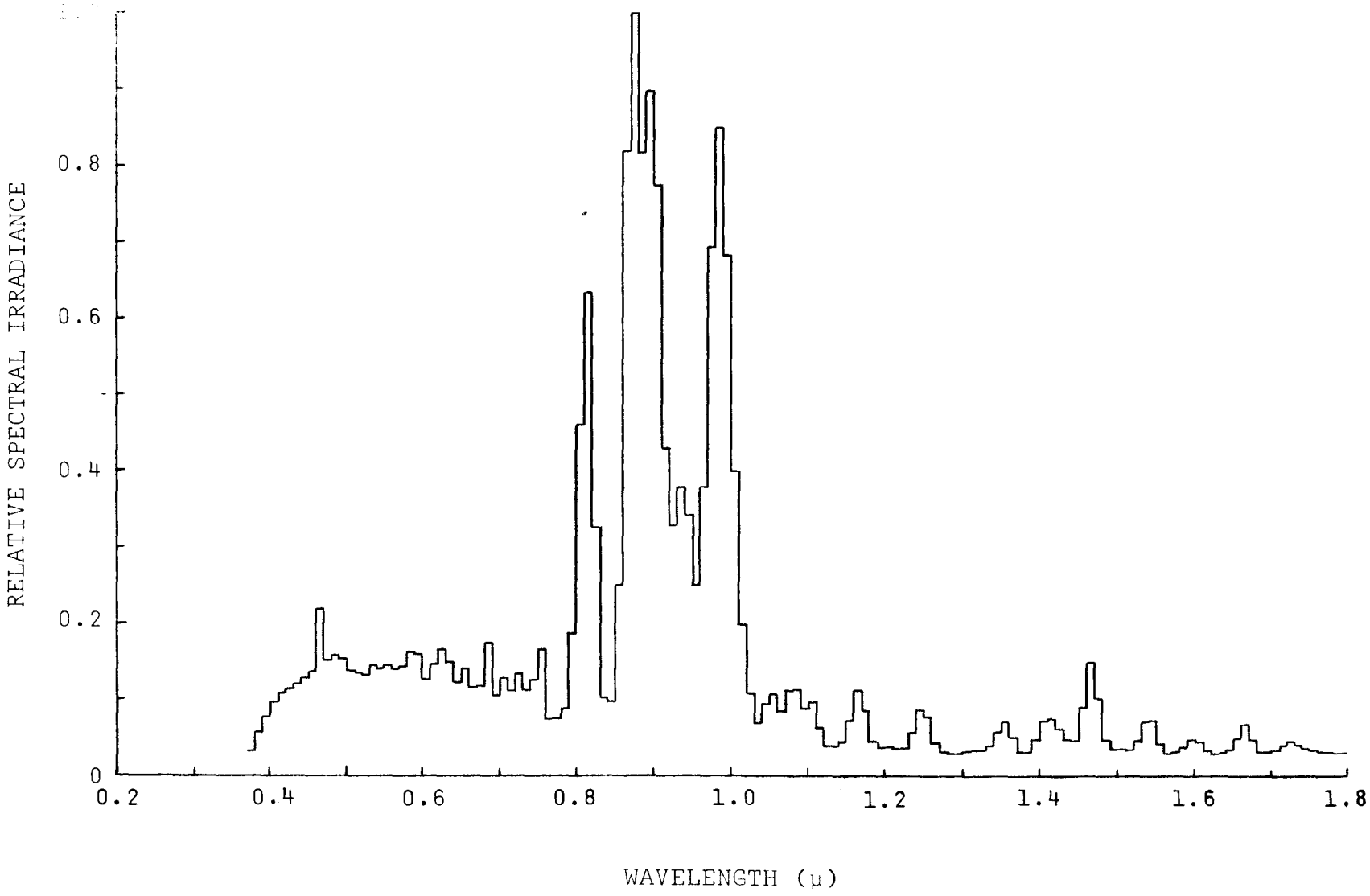

Figure C-1. Spectral radiation distribution of Run A-2: 2.5KW, 25 Mc, 165 psia.

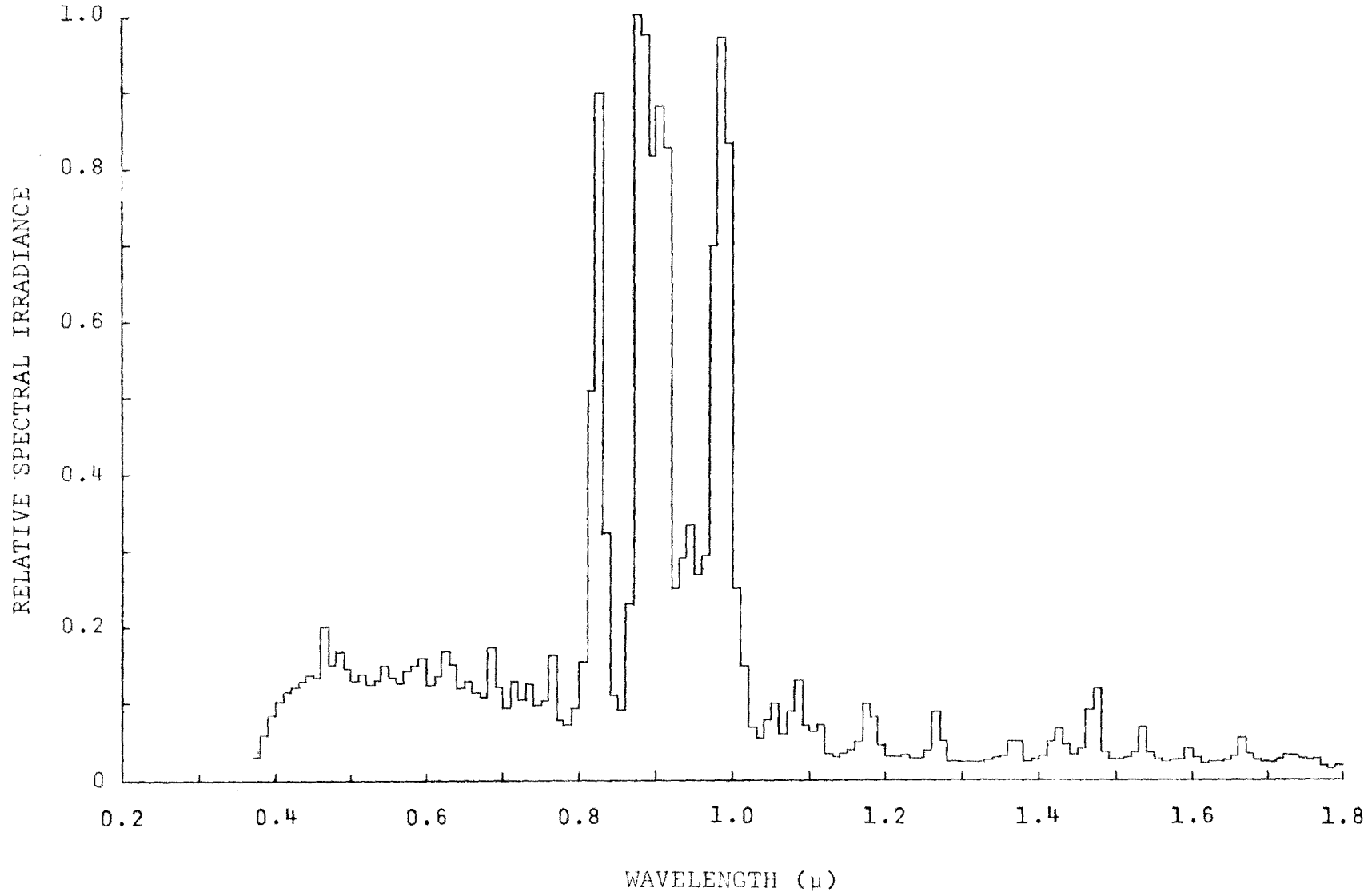

Figure C-2. Spectral radiation distribution of Run B-1: 1KW, 54Mc, 175 psia.

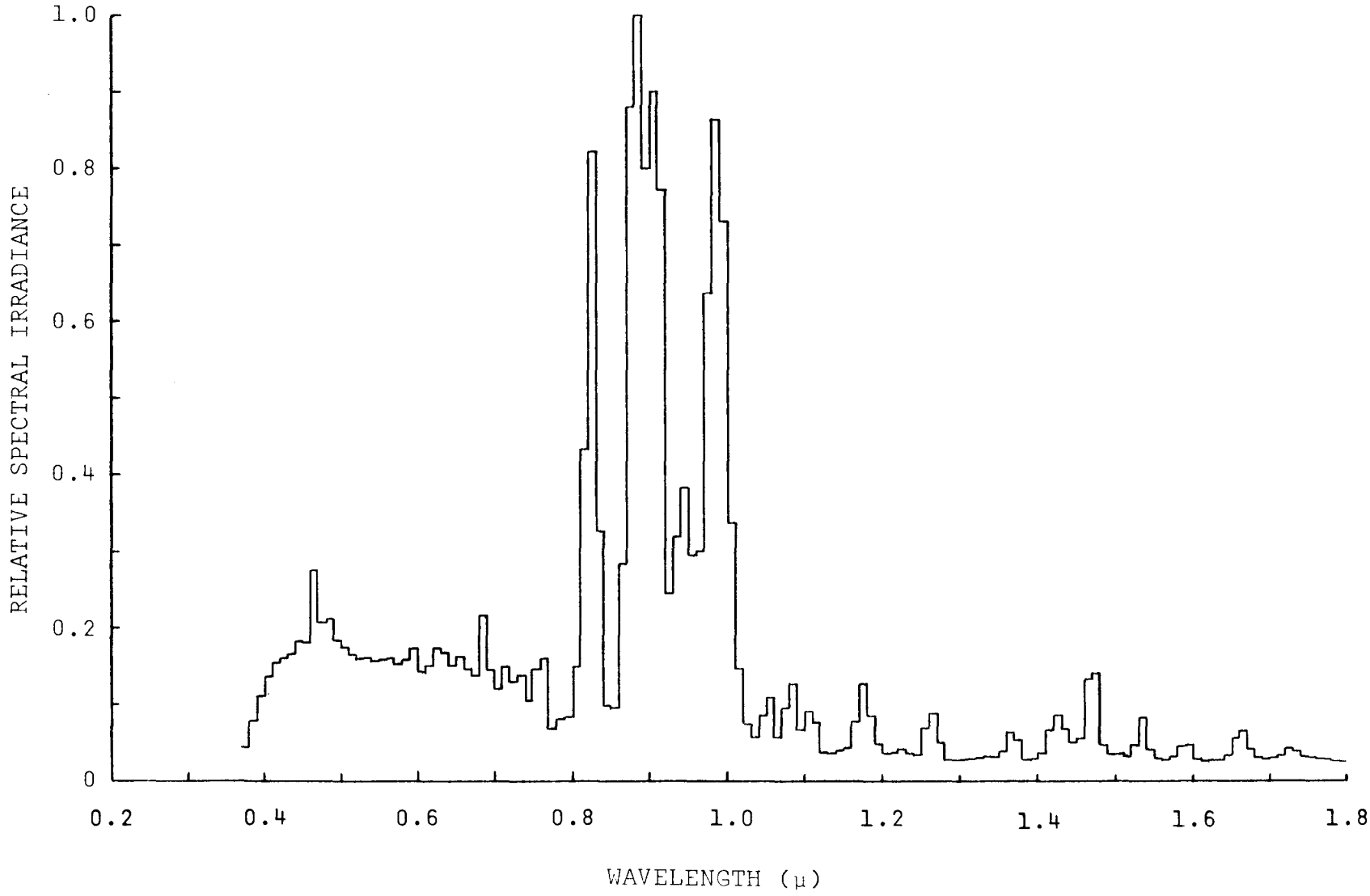

Figure C-3. Spectral radiation distribution of Run B-2: 2.5KW, 54Mc, 210 psia.

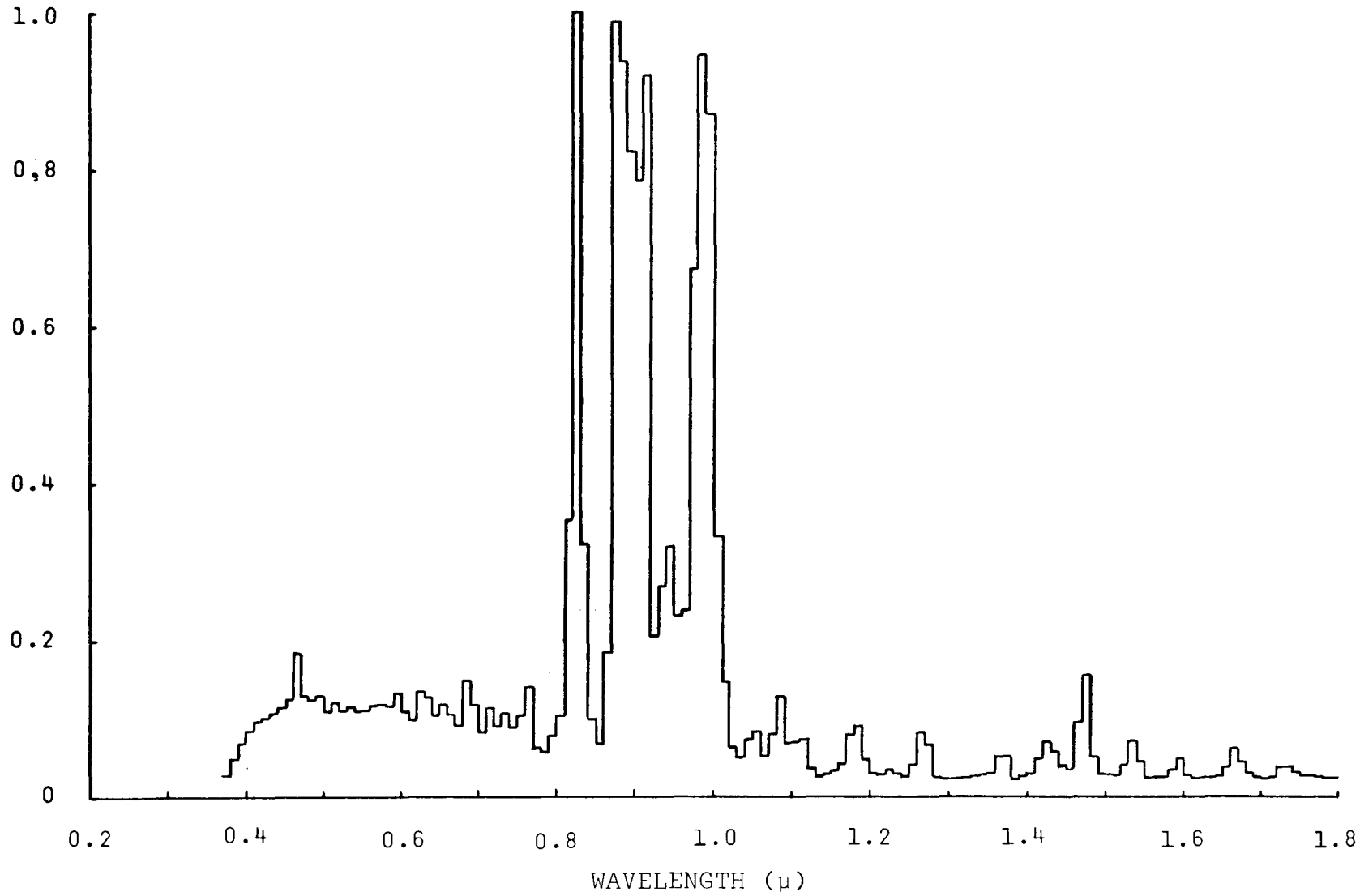

Figure C-4. Spectral radiation distribution of Run C-1: 1KW, 15Mc, 185 psia.

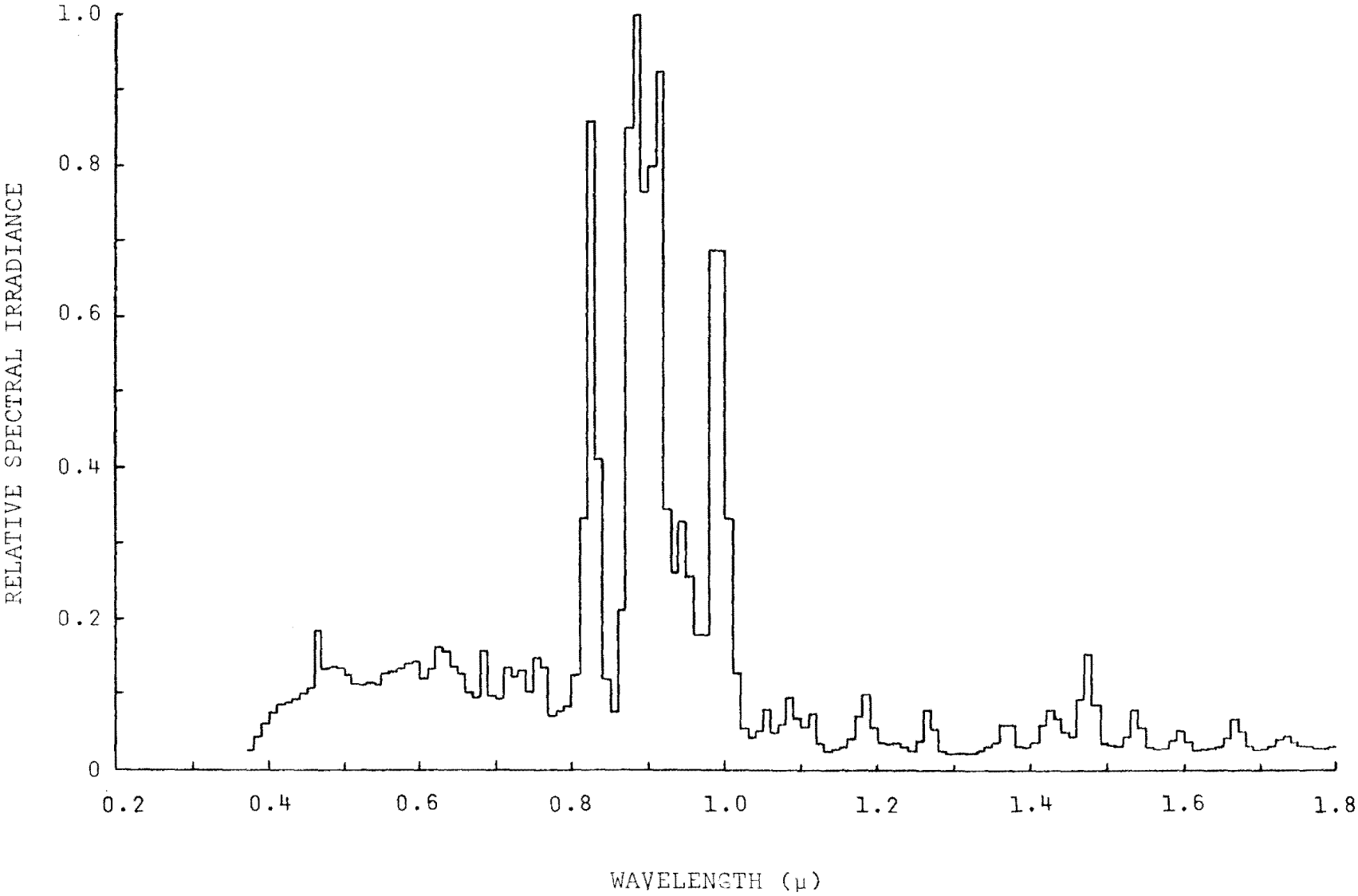

Figure C-5. Spectral radiation distribution for Run C-2: 2.5KW, 15Mc, 170 psia.

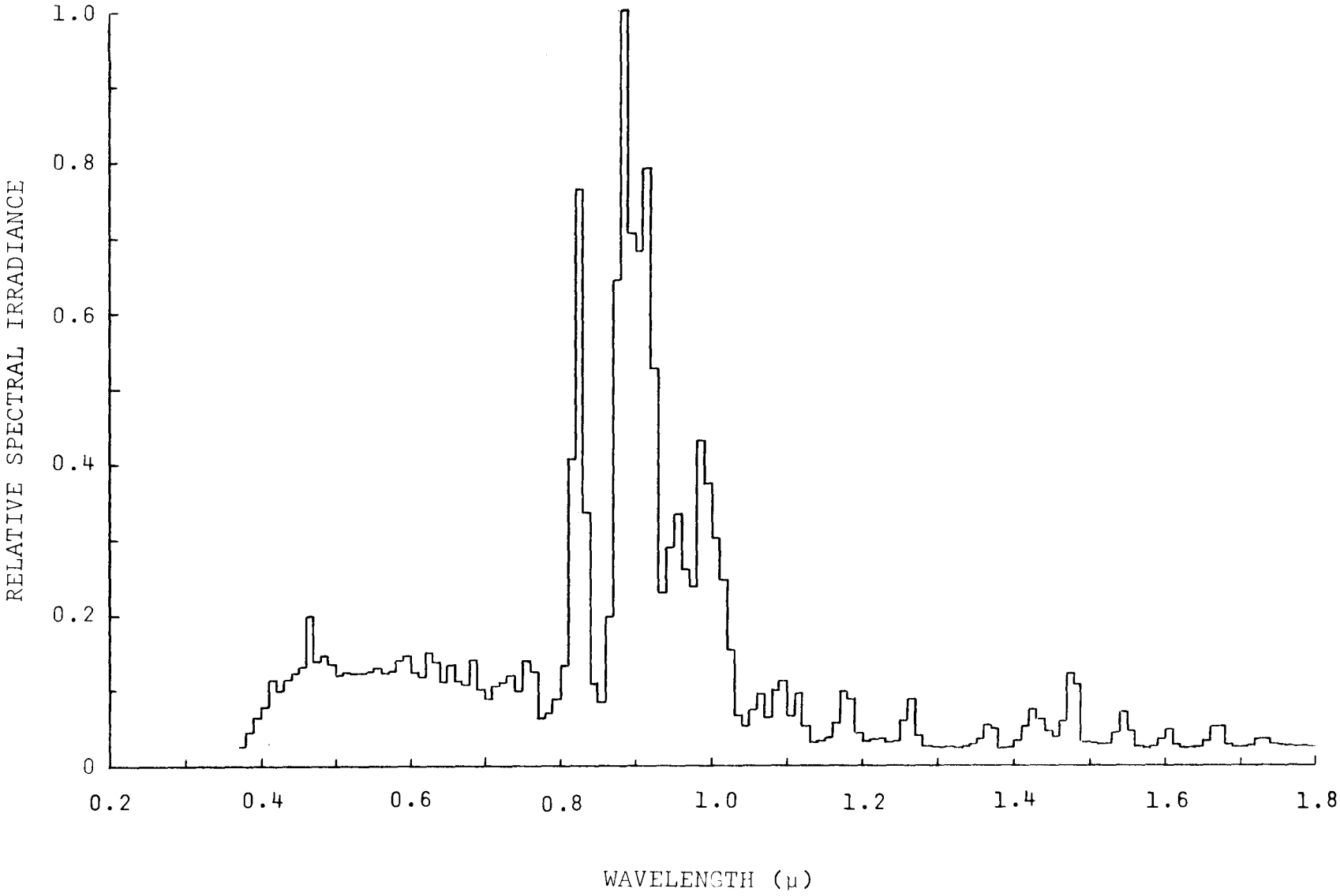

Figure C-6. Spectral radiation distribution for Run SC-2: 2KW, 25Mc, 155 psia

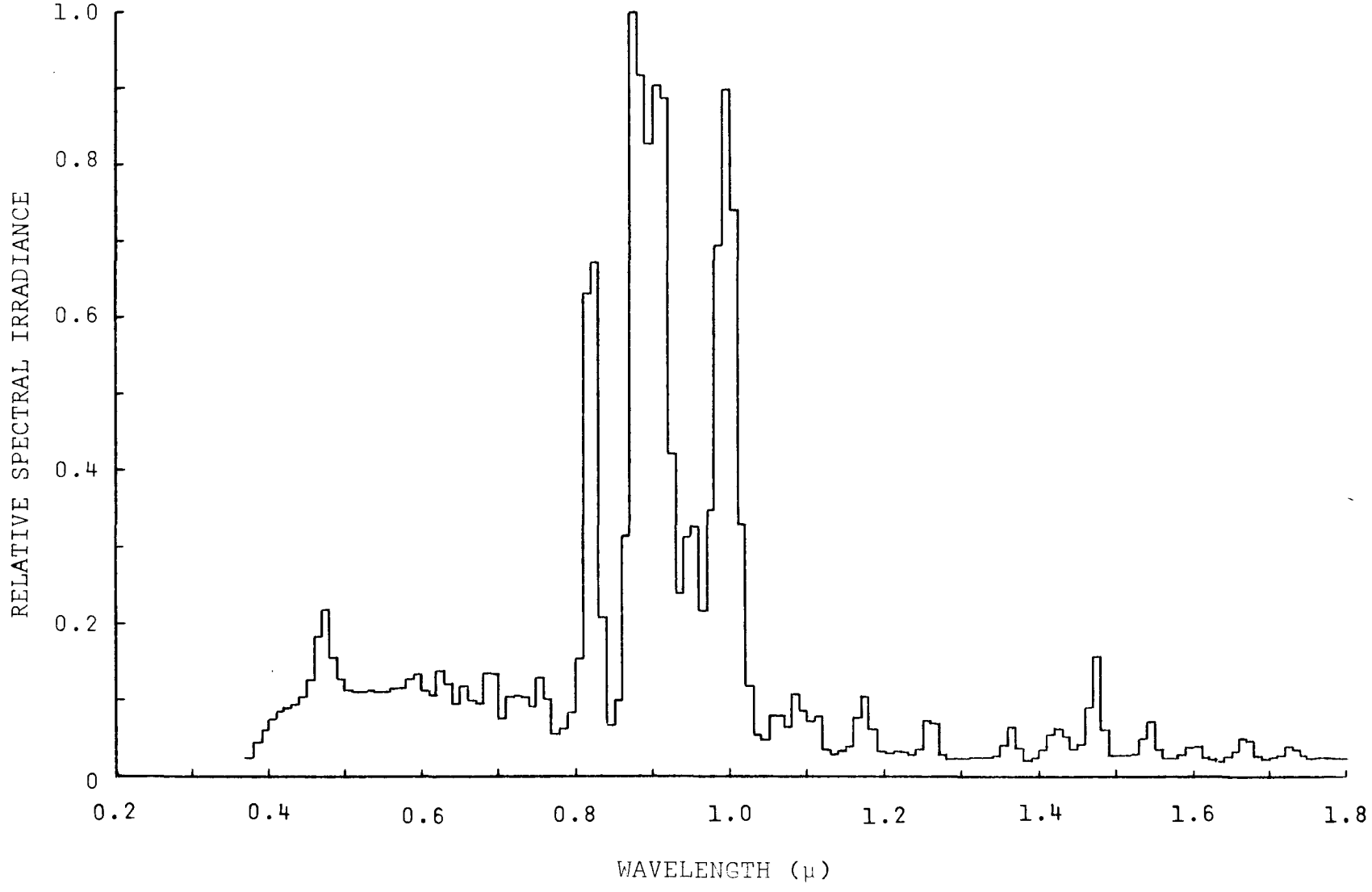

Figure C-7. Spectral radiation distribution for Run SC-1: 1KW, 25Mc, 148 psia.

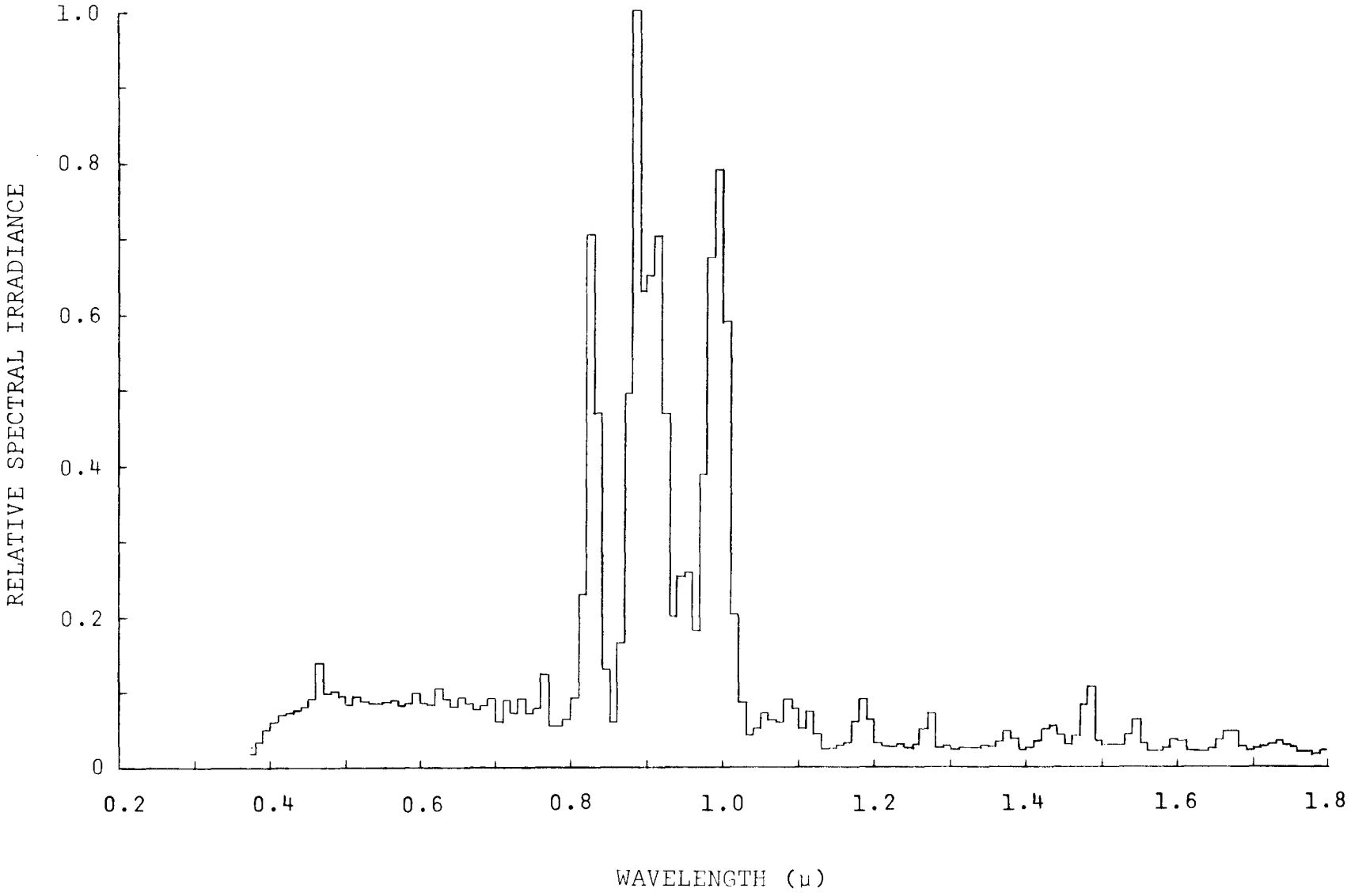

Figure C-8. Spectral radiation distribution for Run BL-1: 1KW, 25Mc, 190 psia.

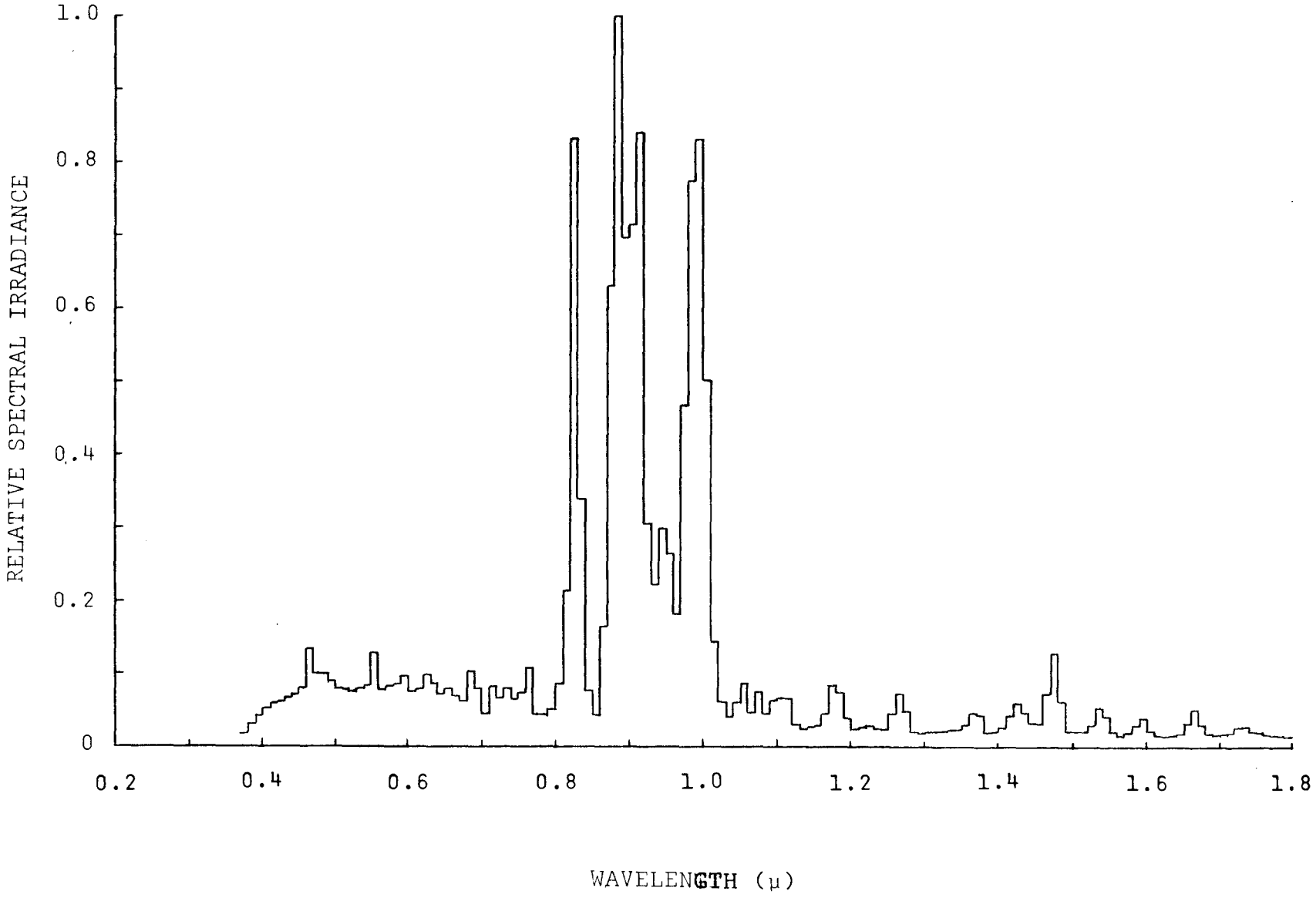

Figure C-9. Spectral radiation distribution for Run SL-1: 1KW, 25Mc, 165 psia.

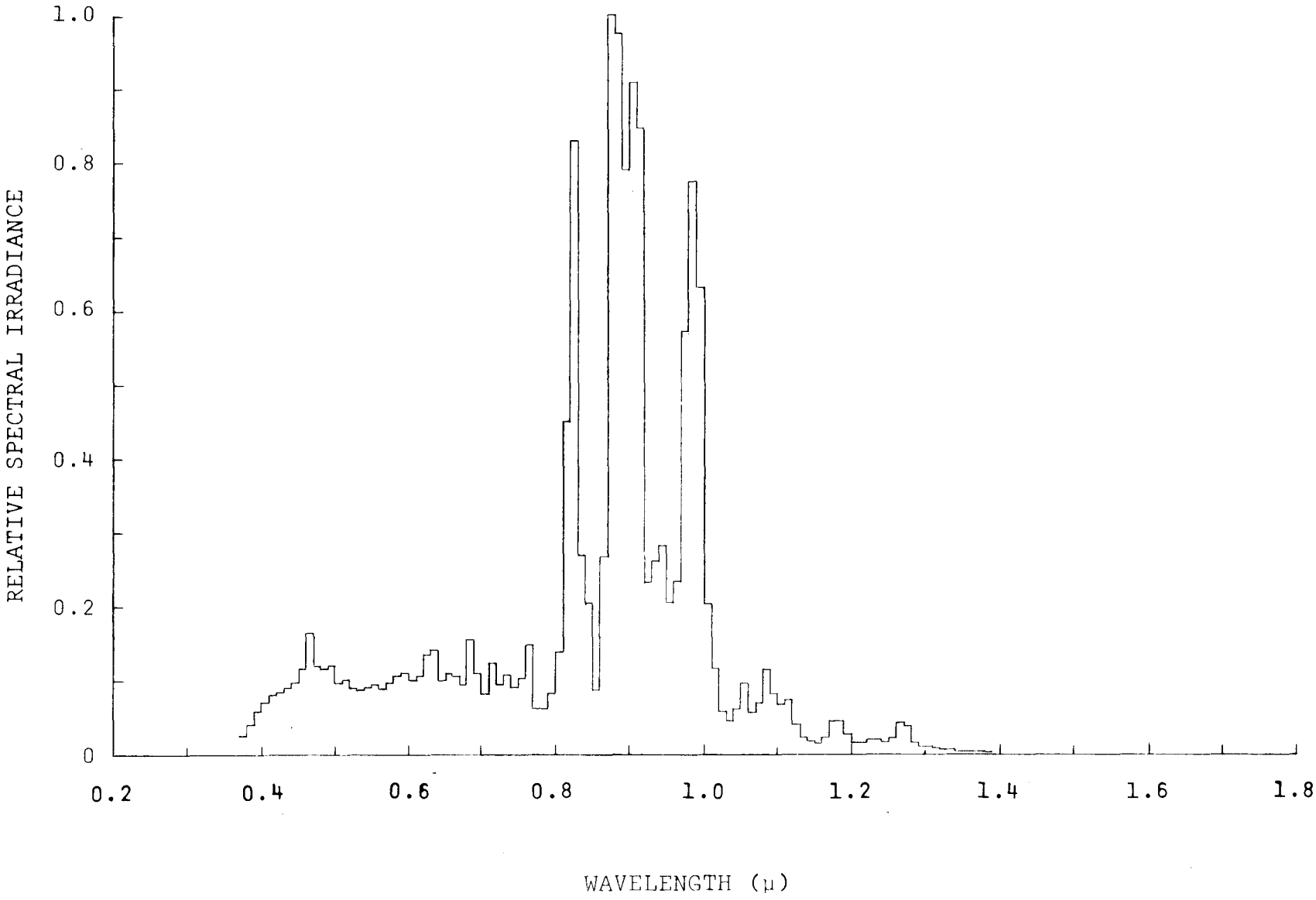

Figure C-10. Spectral radiation distribution for Run W-1: 1KW, 25Mc, 140 psia.

DISTRIBUTION LIST

NUMBER OF COPIES	ADDRESS
2	Advisory Group on Electron Devices ATTN: Secy, Special Group on Optical Masers 201 Varick Street New York, New York 10014
1	IRIA The University of Michigan College of Engineering Willow Run Laboratories Willow Run Airport Ypsilanti, Michigan 48197
1	U.S. Atomic Energy Commission Division of Biology and Medicine Radiological Physics and Instrumentation Branch ATTN: Hodge R. Wasson Washington, D.C. 20545
1	Chief, Bureau of Naval Weapons ATTN: RMGA-6 Department of the Navy Washington, D.C. 20350
1	Commanding Officer Naval Ordnance Laboratory ATTN: Mr. W. Meggers Code 72 Corona, California 91720
1	Commander ASD (ASRNE-42) ATTN: Mr. Melvin R. St. John Wright-Patterson Air Force Base, Ohio 45433

DISTRIBUTION LIST (Continued)

NUMBER OF COPIES	ADDRESS
1	Commanding Officer USAMERDC Technical Documents Center Fort Belvoir, Virginia 22060
1	Aerospace Research Laboratories Office of Aerospace Research United States Air Force ATTN: Dr. Dietrich Langer Wright-Patterson Air Force Base, Ohio 45433
1	U.S. Army Electronics R&D Labs Reconnaissance Branch AMSEL-RD-SAR Fort Monmouth, New Jersey 07703
1	Institute for Defense Analysis ATTN: Lucian M. Biberman 400 Army Navy Drive Arlington, Virginia 22202
1	Air Force Avionics Laboratory ATTN: AVRP (H. Fledel) WPAFB, ohio 45433
1	Director Night Vision Laboratory Ft. Belvoir, VA 22060
20	Defense Documentation Center ATTN: DDC-TCA Cammeron Station (Bldg 5) Alexandria, Virginia 22314
6	Director Night Vision Laboratory ATTN: AMSEL-NV-OR, Mr. Fox Fort Belvoir, VA 22060
1	Commanding General U.S. Army Electronics Command ATTN: AMSEL-TL-BG, Mr. Charles H. Clark Fort Monmouth, New Jersey 07703

Security Classification

DOCUMENT CONTROL DATA - R&D

(Security classification of title, body of abstract and indexing annotation must be entered when the overall report is classified)

1. ORIGINATING ACTIVITY (Corporate author)	2a. REPORT SECURITY CLASSIFICATION
CHARYBDIS, INC. Anaheim, CA 92806	Unclassified
	2b. GROUP

3. REPORT TITLE

A Parametric Survey of the Xenon Electrodeless Arc Lamp

4. DESCRIPTIVE NOTES (Type of report and inclusive dates)

Final Report, May, 1971 - February 1972

5. AUTHOR(S) (Last name, first name, initial)

Hollister, Donald D., Price, Robert E., and Choy, Kim.

6. REPORT DATE	7a. TOTAL NO. OF PAGES	7b. NO. OF REFS
March 1972		10

8a. CONTRACT OR GRANT NO.	9a. ORIGINATOR'S REPORT NUMBER(S)
DAAK02-71-C-0341	CI-72014
b. PROJECT NO. IS663719KK70-03-052	
c.	9b. OTHER REPORT NO(S) (Any other numbers that may be assigned this report)
d.	DAKK02-71-C-0341

10. AVAILABILITY/LIMITATION NOTICES

Approved for public release; distribution unlimited.

11. SUPPLEMENTARY NOTES	12. SPONSORING MILITARY ACTIVITY
	United States Army Night Vision Laboratory Alexandria, VA 22314

13. ABSTRACT

This study treats an experimental survey of key observable properties of the high-pressure xenon electrodeless arc lamp in which performance characteristics and operating trends of the electrodeless arc lamp are described in terms of established operating parameters. The causes of inefficiency in lamp operation were examined and methods developed successfully for improving lamp performance. Data are given which demonstrate lamp operational efficiencies approaching the theoretical maximum. The principal observed cause of electrodeless arc lamp failure is described and techniques are presented for preventing lamp failures. An initial overview of the feasibility, characteristics, and trends of operation of electrodeless arc metal-vapor lamps is presented. Measurements of key properties of the mercury-vapor electrodeless arc lamp are analyzed, and the basic principles of metal vapor lamp operation are extrapolated for application to alkali-vapor electrodeless arc lamps.

DD FORM 1 JAN 64 1473

Security Classification

14. KEY WORDS	LINK A		LINK B		LINK C	
	ROLE	WT	ROLE	WT	ROLE	WT
Radiofrequency plasma Electrodeless arc discharge High pressure plasma Xenon discharge						

INSTRUCTIONS

1. ORIGINATING ACTIVITY: Enter the name and address of the contractor, subcontractor, grantee, Department of Defense activity or other organization *(corporate author)* issuing the report.

2*a*. REPORT SECURITY CLASSIFICATION: Enter the overall security classification of the report. Indicate whether "Restricted Data" is included. Marking is to be in accordance with appropriate security regulations.

2*b*. GROUP: Automatic downgrading is specified in DoD Directive 5200.10 and Armed Forces Industrial Manual. Enter the group number. Also, when applicable, show that optional markings have been used for Group 3 and Group 4 as authorized.

3. REPORT TITLE: Enter the complete report title in all capital letters. Titles in all cases should be unclassified. If a meaningful title cannot be selected without classification, show title classification in all capitals in parenthesis immediately following the title.

4. DESCRIPTIVE NOTES: If appropriate, enter the type of report, e.g., interim, progress, summary, annual, or final. Give the inclusive dates when a specific reporting period is covered.

5. AUTHOR(S): Enter the name(s) of author(s) as shown on or in the report. Enter last name, first name, middle initial. If military, show rank and branch of service. The name of the principal author is an absolute minimum requirement.

6. REPORT DATE: Enter the date of the report as day, month, year; or month, year. If more than one date appears on the report, use date of publication.

7*a*. TOTAL NUMBER OF PAGES: The total page count should follow normal pagination procedures, i.e., enter the number of pages containing information.

7*b*. NUMBER OF REFERENCES: Enter the total number of references cited in the report.

8*a*. CONTRACT OR GRANT NUMBER: If appropriate, enter the applicable number of the contract or grant under which the report was written.

8*b*, 8*c*, & 8*d*. PROJECT NUMBER: Enter the appropriate military department identification, such as project number, subproject number, system numbers, task number, etc.

9*a*. ORIGINATOR'S REPORT NUMBER(S): Enter the official report number by which the document will be identified and controlled by the originating activity. This number must be unique to this report.

9*b*. OTHER REPORT NUMBER(S): If the report has been assigned any other report numbers *(either by the originator or by the sponsor)*, also enter this number(s).

10. AVAILABILITY/LIMITATION NOTICES: Enter any limitations on further dissemination of the report, other than those imposed by security classification, using standard statements such as:

(1) "Qualified requesters may obtain copies of this report from DDC."

(2) "Foreign announcement and dissemination of this report by DDC is not authorized."

(3) "U. S. Government agencies may obtain copies of this report directly from DDC. Other qualified DDC users shall request through _____."

(4) "U. S. military agencies may obtain copies of this report directly from DDC. Other qualified users shall request through _____."

(5) "All distribution of this report is controlled. Qualified DDC users shall request through _____."

If the report has been furnished to the Office of Technical Services, Department of Commerce, for sale to the public, indicate this fact and enter the price, if known.

11. SUPPLEMENTARY NOTES: Use for additional explanatory notes.

12. SPONSORING MILITARY ACTIVITY: Enter the name of the departmental project office or laboratory sponsoring *(paying for)* the research and development. Include address.

13. ABSTRACT: Enter an abstract giving a brief and factual summary of the document indicative of the report, even though it may also appear elsewhere in the body of the technical report. If additional space is required, a continuation sheet shall be attached.

It is highly desirable that the abstract of classified reports be unclassified. Each paragraph of the abstract shall end with an indication of the military security classification of the information in the paragraph, represented as *(TS)*, *(S)*, *(C)*, or *(U)*.

There is no limitation on the length of the abstract. However, the suggested length is from 150 to 225 words.

14. KEY WORDS: Key words are technically meaningful terms or short phrases that characterize a report and may be used as index entries for cataloging the report. Key words must be selected so that no security classification is required. Idenfiers, such as equipment model designation, trade name, military project code name, geographic location, may be used as key words but will be followed by an indication of technical context. The assignment of links, rules, and weights is optional.